

CANADIAN THESES ON MICROFICHE

THÈSES CANADIENNES SUR MICROFICHE



National Library of Canada
Collections Development Branch

Canadian Theses on
Microfiche Service

Ottawa, Canada
K1A 0N4

Bibliothèque nationale du Canada
Direction du développement des collections

Service des thèses canadiennes
sur microfiche

NOTICE

The quality of this microfiche is heavily dependent upon the quality of the original thesis submitted for microfilming. Every effort has been made to ensure the highest quality of reproduction possible.

If pages are missing, contact the university which granted the degree.

Some pages may have indistinct print especially if the original pages were typed with a poor typewriter ribbon or if the university sent us an inferior photocopy.

Previously copyrighted materials (journal articles, published tests, etc.) are not filmed.

Reproduction in full or in part of this film is governed by the Canadian Copyright Act, R.S.C. 1970, c. C-30. Please read the authorization forms which accompany this thesis.

AVIS

La qualité de cette microfiche dépend grandement de la qualité de la thèse soumise au microfilmage. Nous avons tout fait pour assurer une qualité supérieure de reproduction.

S'il manque des pages, veuillez communiquer avec l'université qui a conféré le grade.

La qualité d'impression de certaines pages peut laisser à désirer, surtout si les pages originales ont été dactylographiées à l'aide d'un ruban usé ou si l'université nous a fait parvenir une photocopie de qualité inférieure.

Les documents qui font déjà l'objet d'un droit d'auteur (articles de revue, examens publiés, etc.) ne sont pas microfilmés.

La reproduction, même partielle, de ce microfilm est soumise à la Loi canadienne sur le droit d'auteur, SRC 1970, c. C-30. Veuillez prendre connaissance des formules d'autorisation qui accompagnent cette thèse.

THIS DISSERTATION
HAS BEEN MICROFILMED
EXACTLY AS RECEIVED

LA THÈSE A ÉTÉ
MICROFILMÉE TELLE QUE
NOUS L'AVONS REÇUE

0-315-19580-0

238



National Library of Canada

Bibliothèque nationale du Canada

Canadian Theses Division

Division des thèses canadiennes

Ottawa, Canada
K1A 0N4

67488

PERMISSION TO MICROFILM — AUTORISATION DE MICROFILMER

• Please print or type — Écrire en lettres moulées ou dactylographier

Full Name of Author — Nom complet de l'auteur

MANOJ MISRA

Date of Birth — Date de naissance

July 20, 1954

Country of Birth — Lieu de naissance

INDIA

Permanent Address — Résidence fixe

B-981, Sector A, Mahanagar,
LUCKNOW - 226006, INDIA.

Title of Thesis — Titre de la thèse

A STUDY OF ELECTRON IRRADIATION
DAMAGE TO BIOMOLECULES

University — Université

Univ. of Alberta

Degree for which thesis was presented — Grade pour lequel cette thèse fut présentée

Ph.D.

Year this degree conferred — Année d'obtention de ce grade

1983

Name of Supervisor — Nom du directeur de thèse

PROF. R. F. EGERTON

Permission is hereby granted to the NATIONAL LIBRARY OF CANADA to microfilm this thesis and to lend or sell copies of the film.

L'autorisation est, par la présente, accordée à la BIBLIOTHÈQUE NATIONALE DU CANADA de microfilmer cette thèse et de prêter ou de vendre des exemplaires du film.

The author reserves other publication rights, and neither the thesis nor extensive extracts from it may be printed or otherwise reproduced without the author's written permission.

L'auteur se réserve les autres droits de publication; ni la thèse ni de longs extraits de celle-ci ne doivent être imprimés ou autrement reproduits sans l'autorisation écrite de l'auteur.

Date

July 12 1983

Signature

Manoj Misra

THE UNIVERSITY OF ALBERTA

A STUDY OF ELECTRON IRRADIATION DAMAGE TO BIOMOLECULES

by



MANOJ MISRA

A THESIS

SUBMITTED TO THE FACULTY OF GRADUATE STUDIES AND RESEARCH
IN PARTIAL FULFILMENT OF THE REQUIREMENTS FOR THE DEGREE
OF DOCTOR OF PHILOSOPHY

DEPARTMENT OF PHYSICS

EDMONTON, ALBERTA

FALL 1983

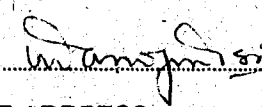
THE UNIVERSITY OF ALBERTA

RELEASE FORM

NAME OF AUTHOR MANOJ MISRA
TITLE OF THESIS A STUDY OF ELECTRON IRRADIATION DAMAGE TO
 BIOMOLECULES
DEGREE FOR WHICH THESIS WAS PRESENTED DOCTOR OF PHILOSOPHY
YEAR THIS DEGREE GRANTED FALL 1983

Permission is hereby granted to THE UNIVERSITY OF ALBERTA LIBRARY to reproduce single copies of this thesis and to lend or sell such copies for private, scholarly or scientific research purposes only.

The author reserves other publication rights, and neither the thesis nor extensive extracts from it may be printed or otherwise reproduced without the author's written permission.

(SIGNED) 

PERMANENT ADDRESS:

B- 981, Sector A,

'Kamlalaya'

Mahanagar, Lucknow 226 006, INDIA

DATED 12 July 1983

THE UNIVERSITY OF ALBERTA,
FACULTY OF GRADUATE STUDIES AND RESEARCH

The undersigned certify that they have read, and recommend to the Faculty of Graduate Studies and Research, for acceptance, a thesis entitled
A STUDY OF ELECTRON IRRADIATION DAMAGE TO BIOMOLECULES submitted by **MANOJ MISRA** in partial fulfilment of the requirements for the degree of **DOCTOR OF PHILOSOPHY**.

R. B. Egerton

Supervisor

[Handwritten signature]

[Handwritten signature]

[Handwritten signature]

External Examiner

Date 12 July 1983



I DEDICATE THIS THESIS TO MY FATHER AND MOTHER

ABSTRACT

The prospects of achieving high resolution in the electron microscopy of biological molecules are greatly reduced because of electron irradiation damage. Information about the structural damage to a specimen, can be obtained by changes in the diffraction pattern, and it is also possible to analyze changes by Electron Energy Loss Spectroscopy (EELS). A comparative study of radiation damage on some biomolecules, amino acids and nucleic acid bases, is described using both of these techniques. The mechanism of radiation damage to these compounds is discussed in terms of their crystal and molecular structures.

An assessment of radiation damage is made, for the first time, on the basis of changes in the Patterson function. Calculation of Patterson function involves computing a Fourier series using the intensities of diffraction spots as Fourier coefficients. Patterson functions were computed for a series of single crystal electron diffraction patterns of 5-iodouracil recorded at increasing irradiation. The mechanism of radiation damage is discussed in terms of a disorder parameter which was found to increase with electron dose. Changes in the Patterson peaks have been related to the structural and chemical damage to 5-iodouracil. Since the computation of the Patterson function does not require phase information, this method of radiation damage assessment is also applicable to the compounds of unknown structures.

A method of obtaining single scattering profile, beyond the L-edge, from the electron energy-loss spectra of Aluminum and Silicon is discussed in the Appendix. This method is based upon the technique of Fourier deconvolution. However, it was not necessary to deconvolute the electron energy-loss spectra of the biomolecules for radiation damage studies since the thickness of these compounds was well below the mean free path of an electron, for inelastic scattering.

ACKNOWLEDGEMENT

About five years ago, it was due to a comedy of errors that I fortuitously found the able and stimulating guidance of Dr. R.F. Egerton, my mentor during the course of this study. I am overwhelmingly grateful and extremely indebted, to him for his generous advice, constant encouragement, helpful and thought provoking discussions and last but not the least, his invigorating and ebullient attitude toward scientific research.

I am extremely thankful to Dr. S.K. Malhotra for allowing me the frequent use of various instruments in his laboratory, without which a major part of this study would not have been feasible.

I would like to thank the members of my supervisory committee (Drs. R.M. Glaeser, J. Gray, S.K. Malhotra and S.S. [redacted] reading my thesis and for their helpful suggestions and constructive criticisms.

I am thankful and indebted to the Department of Physics for the award of a teaching assistantship which covered a part of this research and to the Alberta Heritage Foundation for Medical Research (AHFMR) for the award of a Studentship which indeed allowed me to fully devote my time and attention to research. Without the pecuniary assistance provided by the Physics Department and the AHFMR this journey in the pursuit of mental satisfaction would just have been impossible.

It is a pleasure to thank Mrs. Ruth Nelson for her dexterous and rapid typing of mathematical equations.

I am indebted and thankful to Dr. M.N.G. James of the Department of Biochemistry for his adept explanation of crystallographic folklore to a novice.

I am thankful to my friend Pratap N. Sahay for his initial assistance in computer programming which indeed provided increased versatility to the computer program for generating contour plots.

This all started because of Shyam (S. Shukla). In the absence of his invaluable friendship, I would have been blissfully ignorant about many facets of life. I am deeply indebted to him for vastly enriching my share of experiences, in life.

The presence of Santosh (S. Sikerwar) always heightened the feelings of joy and lessened the pangs of sporadic frustrations. The many hours spent jointly pondering and discussing and sharing academic and non-academic matters, formed a most enjoyable part

of my life. If it is appropriate, I profoundly thank him.

On those, who have always loved me, fell the onus of providing the elemental ingredients necessary for success in life. Their wholehearted support, constant encouragement and inspiration constituted a celestial platform, standing on which I still behold an unflinching beacon of hope.

Table of Contents

	<u>Page</u>
1. INTRODUCTION	1
1.1 The Background	1
1.2 The Object	4
2. ELECTRON-MATTER INTERACTION: EELS AND ELECTRON DIFFRACTION	6
2.1 Elastic Scattering	6
2.2 Inelastic Scattering	9
2.3 Electron Energy-Loss Spectroscopy (EELS)	11
2.3.1 Spectrum Processing for Quantitative Assessment	13
2.3.2 Estimation of Specimen Thickness	17
2.4 EELS and Radiation Damage	18
2.5 Electron Diffraction	18
3. COMPARATIVE STUDY OF RADIATION DAMAGE BY ELECTRON DIFFRACTION AND EELS	21
3.1 Introduction	21
3.2 Experimental Details	23
3.2.1 Specimen Preparation	23
3.2.2 Electron Microscopy	23
3.2.3 Electron Energy-Loss Spectroscopy	25
3.2.4 Analysis of Electron Diffraction Patterns	27
3.2.5 Calculation of Electron Dose	30
3.3 Processing of Electron Energy-Loss Spectra	33
3.4 Results	34
3.5 Discussion	37
3.5.1 Structural Damage to Amino Acids	39
3.5.2 Structural Damage to Nucleic Acid Bases	44
3.5.3 Chemical Damage to Nucleic Acid Bases and Amino Acids	45
4. THE PATTERSON FUNCTION	58
4.1 Historical Introduction	58
4.2 The Definition of the Patterson Function	59
4.3 Characteristics of the Patterson Function	61
4.4 Sharpening of Patterson Function	67
4.4.1 Calculation of B By the Method of Wilson	72

5.	APPLICATION OF THE PATTERSON FUNCTION IN THE RADIATION DAMAGE STUDIES OF 5-IODOURACIL	77
5.1	Introduction	77
5.2	Experimental Details	78
5.2.1	Calculation of Electron Dose	80
5.2.2	Indexing of Diffraction Patterns	80
5.3	Calculation of the Patterson Function	88
5.3.1	Contour Plots of the Patterson Function	90
5.4	Calculation of the B Value	91
5.5	Sharpening of the Patterson Function	98
5.6	Results and Discussion	102
5.7	Factors Contributing to Artifacts in the Intensity Data	112
6.	CONCLUSIONS	119
	BIBLIOGRAPHY	123
	APPENDIX 1: Removal of Mixed Scattering by Deconvolution	131

List of Tables

Table		Page
3.1	Solvents used for the Crystallization of Various Compounds.....	24
3.2	Characteristic Doses for Various Specimens.....	38
3.3	Characteristic Doses Computed from the G-values.....	43
5.1	Data Calculation for Wilson-Plot.....	96
5.2	Effect of Irradiation on Peterson Peaks.....	109

List of Figures

Figure	Page
2.1 A Typical Electron Energy-Loss Spectrum.....	12
2.2 A Schematic EEL Spectrum Illustrating Measurement of Areas for Quantitative Estimation.....	16
3.1 A Plot between Optical Density and Electron Exposure.....	32
3.2 Dose Response Curve for Glycine (Diffraction).....	48
3.3 Dose Response Curve for Methionine (Diffraction).....	49
3.4 Dose Response Curve for Methionine (EELS).....	50
3.5 Dose Response Curve for Valine (Diffraction).....	51
3.6 Dose Response Curve for Cysteine (Diffraction and EELS).....	52
3.7 Dose Response Curve for Cystine (Diffraction).....	53
3.8 Dose Response Curve for Uracil (Diffraction and EELS).....	54
3.9 Dose Response Curve for Thymine (Diffraction and EELS).....	55
3.10 Dose Response Curve for Cytosine (Diffraction and EELS).....	56
3.11 Dose Response Curve for Adenine (Diffraction and EELS).....	57
4.1 The Formation of Patterson Peaks.....	63
4.2 The Distribution of Patterson Peaks in a Two-dimensional Unit Cell.....	65
4.3 Point Atom Approximation.....	69
4.4 Dependence on B of Atomic Scattering Factor.....	71
4.5 Wilson Plot.....	76
5.1 Densitometer Trace of a Single Layer-line and Background Fit from the Diffraction Pattern of 5-Iodouracil.....	81
5.2 Location of the Innermost Spots around the Central Spot.....	85
5.3 Intensity Weighted Diffraction Pattern of 5-Iodouracil.....	89
5.4 $p(u,v)$ Patterson Function as Calculated by Buerger (Figure a) and Calculated Using MODPAT and CONTOUR (Figure b).....	92
5.5 Atomic Scattering Factors for C, N and O (Figure a) and for I and H (Figure b) plotted with respect to $\sin \theta / \lambda$	93
5.6 A Simple Schematic Diagram for the Calculation of $\sin \theta / \lambda$	94
5.7 Zones of Decreasing $\sin \theta / \lambda$ for Wilson Plot.....	97
5.8 Wilson Plot at a Cumulative Dose of 6.4 C m^{-2}	99

5.9	Dependence of B on Dose.....	100
5.10	Four Adjacent Cells of 5-Iodouracil Around a Common Centre Point (the inner cell encloses two molecules of 5-Iodouracil).....	105
5.11	Patterson peaks due to Iodine and Other Atoms of Figure 5.10.....	106
5.12	(a) Unsharpened Patterson Function, Figures (b) to (d) Sharpened Patterson Functions at Increasing Dose.....	113
5.13	(a) to (d) Sharpened Patterson Functions at Increasing Dose.....	114

List of Plates

Plate		Page
3.1	Diffraction Pattern of Gold.....	28
3.2	Diffraction Pattern of Uracil.....	29
3.3	Diffraction Pattern of Glycine at Increasing Doses (a through d) and EEL Spectrum for Adenine (e).....	35
5.1	Diffraction Pattern of 5-Iodouracil.....	83

CHAPTER I

INTRODUCTION

1.1 The Background

The decade of the nineteen twenties constituted a turbulent period for Physics as the old concepts were changing, yielding place to new. In the midst of these changes and with the emergence of Quantum Mechanics, a set of new rules were being developed; germane to these rules was the novel idea of wave-particle duality. In 1927 Davisson and Germer conducted a classical experiment involving diffraction of electrons by crystals which firmly established the wave nature of electrons. Although the determination of crystal structures by Fourier methods based upon X-ray diffraction data was then a fairly developed technique still it took a long time before successful results could be accomplished from electron diffraction data (Vainshtein and Pinsker, 1949).

Even before the construction of the first electron microscope, Dennis Gabor had expressed his apprehension about the utility of such an instrument as is evident by his remark '.....what is the use of it (electron microscope)? Everything under the electron beam would burn to a cinder!' (Marton, 1968). This skepticism, however, did not deter the making of an electron microscope and its subsequent use. The problem raised by Gabor was, to some extent, circumvented by the techniques of staining and embedding which when employed on the specimen seemed to protect its structure up to a resolution greater than about 2 nm. For a little more than a decade now, techniques have been developed for fully exploiting the potential of modern electron microscopes. The aim is the 'visualization' of structures at atomic levels, either in isolation or in their positions in crystalline arrays. When one seeks to gather information at resolutions better than 1.5 to 2.0 nm, the conventional techniques of negative staining fail (Unwin, 1975). The unstained, 'naked' specimen again faces a hostile environment in the microscope column and the long forgotten apprehension of Gabor becomes a question of paramount importance.

In as much as X-ray diffraction techniques have been applied so successfully to the elucidation of the structure of various proteins and other biomolecules at the atomic level, what is the justification of exposing the specimen to high energy electrons in an electron microscope? This question actually overlooks certain advantages, of immense

importance, that electron microscopy offers over X-ray diffraction. Owing primarily to the large cross-sections for the scattering of electrons by matter compared to those for X-rays, the crystal size criterion, which requires large single crystals for X-ray diffraction, can be considerably relaxed for electron microscopy. The phase information is lost in the recording of the diffraction spots (for X-rays and electrons both). The retrieval of phases, in X-ray crystallography, hence requires collection of diffraction data not only from the specimen under study but also from single or more sets of isomorphous crystals (i.e. crystals from which an atom or two, in the unit cell, have been substituted by a heavy atom without altering the unit cell in any other way). This makes phase determination a very cumbersome and laborious process in X-ray diffraction. The situation in an electron microscope is much easier. Since the scattered beam of electrons can be focused to form an image and since the phases are preserved in the images, they can be retrieved by determining the Fourier transform of digitized images. Another advantage of using electrons is the drastic reduction in the recording time of the diffraction pattern. X-rays require exposures of many hours whereas for electron diffraction patterns recording times are of the order of a few seconds to a few minutes.

For more than a century, a cell has been considered to be the unit of life. Our understanding of functional aspects of various intricate physiological and biochemical processes has a great deal to owe to this concept. At the same time, the ubiquitous presence of proteins in cell membranes and their involvement in numerous processes of fundamental importance to life have made membrane proteins indispensable for the living cells. The power of X-ray crystallography in elucidating the three-dimensional structure of certain soluble proteins (oxygen carrying proteins and certain enzymes) is now well established. However X-ray methods are unsuitable for structural investigations of membrane proteins, since most of the membrane proteins have resisted all attempts to crystallization. On the other hand, they can, with due effort, be induced to crystallize into two-dimensional ordered arrays in the plane of the membranes. These crystalline sheets are suitable for structural analyses by electron microscopy.

The requirement of small crystal size, for electron diffraction, has provided hope for elucidating structure of biomolecules which resist crystallization and are not open to study by X-ray techniques. This initial advantage of electron microscopy is, however,

offset by the damage caused to the structure by impinging electrons. Glaeser (1975) has formulated an equation which describes the relationship between necessary irradiation and obtainable resolution in an electron microscope image. Using his equation it can be shown that the recording of an image of an object of 0.35 nm diameter one will need to expose the specimen to at least 400 electrons per \AA^2 . The question that high-resolution electron microscopists have been compelled to ask is how authentic and truly replicative of the structure would an electron microscope image be at such high doses of irradiation? In other words, are the chemical and structural features altered during the exposure of the specimen to the electron beam? It indeed seems that single chief source which greatly hampers the prospects of high-resolution electron microscopy is radiation damage (Glaeser, 1975 and Cosslett, 1975).

Since radiation damage is the biggest barrier to realization of the dream of atomic imaging of biological molecules, efforts should be directed towards finding out the ways of reducing it. However, what is even more important, before a medication can be prescribed, is a clear understanding of the diagnosis. Myriads of interactions are possible when an electron passes through a specimen which could result in manifold mechanisms of irradiation damage. Our knowledge of these interactions is, unfortunately, still scanty and poor (Glaeser, 1975). Although it is not possible, even with the best available microscopes, to monitor the individual damage events at the atomic level (Cosslett, 1978), there exist several methods for calculating the extent of specimen damage. These are directed toward the measurement of changes in certain macroscopical features during irradiation, such as the fading of diffraction spots from a crystalline specimen, mass loss and changes in infra-red or electron energy-loss spectra. All these different methods provide different types of information and the use of one or the other depends upon the desired aspect of information about radiation damage. Those techniques of damage assessment which provide the convenience of *in situ* measurements have naturally been more actively pursued. These comprise monitoring the fading of diffraction spots and changes in an electron energy-loss spectrum. Changes in diffraction patterns of crystalline amino acids and other organic compounds were studied by Glaeser (1971) and Siegel (1972). Isaacson (1972) using changes in the low-loss region of an electron energy-loss spectrum as an indicator, studied the damage process in nucleic acid bases.

He also performed some comparative studies by comparing the low-loss data obtained from an energy-loss spectrum with mass loss measurements and diffraction measurements (Isaacson, 1974). Experimental measurements which have been conducted so far seem to suggest the dependence of damage kinetics on the molecular and crystal structure of the specimen. Essentially, the diffraction and energy-loss methods provide information about the collapse of crystalline order and chemical damage to the specimen, respectively. It is not clear in what order and exactly how the damage actually takes place. Moreover, various experimental parameters have been found to affect the sensitivity of the specimen to electron irradiation, as is evident by large differences existing in the published sensitivities of various compounds. Since no relation between various phenomena and loss of structural information has been made (Zeitler, 1982), it is believed that a greater insight into damage mechanisms could be obtained by quantifying damage process with an overall objective of comparing chemical destruction with structural damage.

1.2 The Object

With this as background, a systematic study of radiation damage was undertaken on nucleic acid bases and some amino acids. The purpose was to compare two types of damage--structural and chemical--using the techniques of electron diffraction and electron energy-loss spectroscopy. In this study a comparison between these damage processes has been made on the basis of their known crystal structures and different intra- and inter- molecular bondings.

Monitoring the fading of diffraction spots with electron irradiation is one way of observing increasing disorder within the crystal structure. Another possible method would be to construct the projected potential of the crystal structure by computing a Fourier series involving structure amplitudes of different diffraction spots (as measured from their intensity) and their phases. Such calculations based on diffraction patterns recorded at increasing irradiation would highlight the damage kinetics and could provide precise information about the mechanism of radiation damage. Clark et al. (1979) conducted such a study on α -copper phthalocyanine to study damage kinetics. Although Fourier synthesis does provide extensive information about radiation damage, it suffers

from two associated problems. First, since the phase information is lost in the recording of a diffraction pattern, any such computation of Fourier synthesis in the absence of phase information would in principle be impossible. For α -copper phthalocyanine, the phases were taken from the X-ray data of a structurally similar compound: platinum phthalocyanine. However, an assessment of radiation damage, for a compound of unknown structure, cannot be made by reconstructing the projected crystal potential due to lack of phase information. The second problem associated with such a Fourier synthesis is following: Do the phases change as the specimen gets progressively disordered and damaged? If answer to this question is yes, then an immediate question is how do the phases change. Clark et al. reasoned that since the structure of α -copper phthalocyanine is centrosymmetric, the phases can assume only two values: 0 and π , hence a change in phase would occur only if the intensity of a spot passes through a zero before reappearing. Since such an event was not observed, they concluded that the phases indeed remain the same. However, if the structure of the specimen is non-centrosymmetric, the phases would not be confined to these two values but could assume any value between these two extremes. In such a case, it is not clear whether the phases would still stay the same or not. Inclusion of incorrect phases could then lead to the determination of incorrect structure in projection.

In this thesis, a method of radiation damage assessment is reported, based upon Patterson synthesis. This involves the calculation of Fourier series using the intensities of diffraction spots as Fourier coefficients (phases are not included). The resulting function, known as the Patterson function, yields information about the distribution of interatomic vectors within a unit cell. This technique was applied to a series of diffraction patterns of 5-iodouracil recorded at increasing doses. During the course of this investigation a relationship between the 'disorder factor' (as the name implies--a factor which is related to increasing disorder of the crystal structure) and increasing electron irradiation was also determined. Phases are not involved in such a calculation, so this method is not handicapped by the problems mentioned above. It should be applicable to both centrosymmetric and non-centrosymmetric structures. However, due to absence of phase information, the information obtained by a Patterson synthesis is not as exhaustive as it would be by including the phases in a Fourier synthesis.

CHAPTER II

ELECTRON-MATTER INTERACTION: EELS AND ELECTRON DIFFRACTION

The situation in an electron microscope is indeed paradoxical. Those same electrons which, by virtue of their interaction with the atoms, reveal the specimen structure and surface morphology may also completely obliterate the desired information due to these interactions. What is desirable is to have a proper estimate of irradiation which can be safely used without disturbing the structural and chemical characteristics of the specimen, at a certain resolution level. Depending primarily upon the specimen nature and the energy of the electrons, there are various modes of electron-specimen interaction. All these different types of scattering events are not necessarily damaging in nature. For a damaging event to occur, energy must be transferred to the specimen by the electron beam. Energy transfer, however, depends upon the kinetic energy of the electrons and the chemical constitution of the specimen. Hence, the probability of occurrence of various damaging events must be considered in the light of various interaction mechanisms. The following discussion will highlight certain features pertinent to these scattering processes, with an overall objective of discussing the mechanisms of electron irradiation damage.

2.1 Elastic Scattering

In a neutral atom comprising equal positive and negative charges, the negative potential due to electron shells (because of its spreading) is smaller than the positive potential due to the concentrated nature of nuclear charge. Hence, the potential inside the neutral atom is positive and is equal to the nuclear potential modified by the screening effect of the surrounding atomic electrons. When an accelerated, high-energy electron enters a specimen, it is attracted towards the nucleus due to the net positive potential. This Coulombic attraction is similar to the scattering of α -particles, first observed by Rutherford, except that the force on an α -particle is repulsive. An important feature of such an interaction between the impinging electron and the nucleus is the large ratio between the mass of the atomic nucleus and the electron. This implies that such an electron-nucleus interaction is generally not strong enough to dislodge the atom from its original position, since it involves loss of only a negligible fraction of energy of the

incoming electron. However, the Coulombic nuclear attraction deviates the electron from its original direction and a transfer of momentum occurs to the nucleus. This type of scattering, which involves negligible energy transfer from the electron to the specimen, is called *elastic scattering*. The angle of scattering is primarily governed by the atomic number of the atom, energy of the electron and its proximity of approach to the nucleus. The deflected electron follows a hyperbolic trajectory with the nucleus at the focus of the trajectory. The probability with which an elastic encounter takes place between an electron and an atom is given by the cross-section for such an event. The cross-section for scattering varies with the angle of scattering, and the probability with which an incident electron is deviated from its initial direction by an angle θ into a cone of solid angle $d\Omega$ is called the differential cross-section. Formulae for elastic scattering have existed, in quantum mechanical formulation, for a long time and are due to Wentzel (1927). The total elastic cross-section (i.e. total probability of scattering in all the directions) from the Wentzel model can be written as:

$$\sigma_{e1} = \frac{\lambda_c^2}{\pi\beta^2} [a/a_0]^2 Z^2 \quad (2.1)$$

where λ_c is Compton wavelength, a is the effective atomic radius, a_0 is Bohr radius, Z is nuclear charge and $\beta = v/c$, where v is the velocity of the electron and c is the velocity of light. If according to Lenz (1954) we choose $a = a_0 Z^{-1/3}$, then equation 2.1 can be written, in the Lenz-Wentzel model, as:

$$\sigma_{LW} = \frac{\lambda_c^2}{\pi\beta^2} Z^{4/3} \quad (2.2)$$

Because of the simplicity of these expressions they are often applied in electron microscopy but the accuracy of these equations is rather poor for high atomic number elements for which the Lenz-Wentzel equations yield low values of the total atomic cross-section and show incorrect angular dependence for differential cross-sections (Isaacson, 1977). The scattering angles for elastic collisions are rather high. For example,

for the collision of a 100 keV electron with a specimen of amorphous carbon the scattering angle is typically 20 mrad. Elastic scattering in the case of crystalline specimens gives rise to scattered beams of electrons in well-defined specific directions, according to Bragg's law and leads to the formation of a diffraction pattern. The phenomenon of electron diffraction is discussed separately later in this chapter.

It is misleading to say that no energy loss occurs in the case of elastic scattering, since some radiation is indeed emitted when the electron is deflected by Coulombic nuclear attraction (Schwinger, 1949) but such losses are negligible compared to the energy of the incident electrons and beyond the threshold of detectability. Even the energy spread of the electron beam (due to thermionic emission and Boersch effect) is orders of magnitude greater compared to the amount of energy lost. Hence, elastically scattered electrons do not cause damage to the specimen in general. The only process whereby an elastic scattering could result in damage occurs if the angle of scattering is very large, resulting in large momentum transfer to the specimen. In such cases the law of conservation of energy and momentum requires transfer of a certain amount of energy. If the energy transferred exceeds the binding energy of the atom then the atom could get displaced from its position. Corbett (1966) has calculated the recoil kinetic energy (E_r) transferred to an atom using kinematic arguments involving conservation of momentum and energy and it can be written as:

$$E_r = E_{\max} \left[\sin\left(\frac{\theta}{2}\right) \right]^2 \quad (2.3)$$

$$E_{\max} = 2 \left(\frac{m}{m_A} \right) \frac{E_o}{mc^2} (E_o + 2mc^2)$$

where θ is the angle of scattering, E_o is the energy of the incident electron beam, m is the rest mass of an electron and m_A is the mass of an atom. E_{\max} is the maximum energy that can be transferred to an atom by an electron. E_{\max} is usually small in the case of 100 keV electrons for all atoms except hydrogen, but for large incident electron energies and light atoms the value of E_{\max} can be significantly high. This type of damage due to an elastic collision is called 'knock-on' damage and evidently is not important for the present study which was conducted at 80 keV energy of the incident electron beam.

2.2 Inelastic Scattering

In addition to the elastic scattering discussed above, which is essentially due to electron-nucleus interaction, an incident electron may interact with the atomic electrons of the specimen. Such an interaction usually results in transfer of energy to the specimen due to the comparable masses of the interacting bodies. This process whereby the incident electron loses energy is called inelastic scattering.

Since a solid is an ensemble of various types of atoms, there exist various modes of energy transfer to the solid by the electron beam. In a crystalline solid, the atoms are not rigidly located at their atomic sites but oscillate about their mean position due to thermal vibrations. When the incident electrons suffer Bragg reflection from crystal planes, the intensity of the diffraction spots is modified due to thermal scattering and sharp intensity maxima exhibit a broader angular distribution of intensity (Hall, 1965). Since a quantized lattice vibration is called a phonon, the electron-phonon interaction in the lattice leads to the creation and annihilation of phonons. The energy losses involved in this type of scattering are very small usually of the order of 0.1 eV.

Another feature that is a manifestation of the solid state is the collective excitation of valence electrons by an external stimulus. If a small fluctuation in the density of valence electrons occurs due to the incoming beam of electrons, then due to Coulombic forces between valence electrons, oscillations occur in electron density with a certain angular frequency. The energy of such oscillations is quantized and if the angular frequency of oscillations is ω_p then plasmon energy will be $\hbar \omega_p$ where \hbar is the Planck's constant divided by 2π , which is of the order of 10-50 eV for most materials. This energy value is too large to be excited by thermal lattice vibrations but energy losses of this order do occur when an electron beam passes through a solid (Pines, 1963). Most of the plasmon scattering is forward peaked (i.e. confined close to scattering angle $\theta = 0$). The differential cross-section of scattering is given by (Raether, 1965):

$$\frac{d\sigma}{d\Omega} = \frac{k}{\theta^2 + \theta^2 \frac{E}{E_0}} \quad (2.4)$$

where K is equal to $\theta_E G(\theta) / 2\pi n a_0$, n is the free electron density contributing to the oscillations, a_0 is Bohr radius. If E is the energy lost by the incoming beam of electrons of energy E_0 then $\theta_E = \frac{E}{2E_0}$ and $G(\theta)$, according to Ferrel (1957) is a factor equal to 1

upto a certain cut-off angle θ_c , above which it drops to zero.

Besides the collective mode of excitation of valence electrons, the incident electron may lose energy by single electron excitations. Core electrons and valence electrons may both be excited by this process. In the case of metals, which have partially filled highest energy band, the valence electrons can undergo transition to higher levels in the same band. The energy required for such an intraband transition is of the order of a few eV. On the other hand, in case of insulators or semi-conductors having energy bands separated by energy gaps, the electrons in the valence band can make interband transitions to the conduction band upon receiving sufficient energy.

Since, the inner shell electrons or core electrons are tightly bound, they require considerably more energy for excitations to the higher states or for complete ionization, compared to valence electrons. Provided sufficient energy transfer occurs, the core electrons are excited to empty states above the Fermi level. If the incident electron loses energy in excess of that required for ionization, the extra energy is acquired as kinetic energy by the ionized electron. Atomic losses in this type of scattering are of the order of 100 eV to many keV, depending upon the atomic number of the atom and the proximity of the shell to the nucleus i.e. on the principal quantum number, n , of the shell.

On the basis of the free electron model, the angular distribution of those electrons, which have been scattered by valence electrons, is proportional to the square root of the energy loss at a particular value of E_0 . However, experiments (Egerton, 1975) support quantum-mechanical calculations of Bethe (1928) that for large energy losses the scattering from valence electrons occurs within a ring in the diffraction plane and is not peaked in the forward direction. Whereas, the scattering in the case of plasmon losses and for transitions involving tightly bound core electrons is peaked in the forward direction.

Scott (1965) and Lenz (1954) have shown from theoretical calculations involving atomic screening that the ratio of elastic to inelastic scattering is proportional to the atomic number, Z . Experimental measurements (Egerton, 1975) have shown a preponderance of inelastic scattering over elastic scattering in carbonaceous materials. However, theoretical calculations based upon more refined models (Egerton, 1982) indicate that the increase in the ratio of elastic to inelastic scattering, over a limited range

of atomic numbers, is not proportional to Z (as calculated by Lenz and Scott).

The possibility of knock-on damage due to elastically scattered electrons is negligible for 80-100 keV electrons, as is evident from the above discussion on elastic scattering. From a crystalline specimen the elastically scattered electrons may be focused to form a diffraction pattern. The occurrence of ordered structures and induced crystallization of biological molecules to form two-dimensional arrays of crystals has opened the possibility of using electron-diffraction techniques in three-dimensional structural studies, as witnessed by the structure determination of the purple membrane from *Halobacterium halobium* by Henderson and Unwin (1975).

Since for damage to occur energy must be deposited into the specimen, the inelastically scattered electrons were initially considered as a ubiquitous hindrance in electron microscopy, marring the image quality and causing radiation damage. However, with the advent of various techniques of energy analysis these very electrons provided a method for determining the chemical composition of the specimen. The use of the inelastically scattered electrons for chemical analysis was originally proposed by Hillier and Baker (1944). However, the idea lay dormant for a long time until some preliminary measurements were carried out by Watanabe (1964) and later by Wittry et al. (1969) and Isaacson (1972).

The following discussion is mainly about the techniques of electron energy-loss spectroscopy and electron diffraction and their application to radiation damage studies of biological molecules.

2.3 Electron Energy-Loss Spectroscopy (EELS)

Assuming a monoenergetic beam of electrons impinging on a specimen, an electron energy-loss spectrum displays the various modes of inelastic scattering discussed above. A typical spectrum shown in Figure 2.1 is a plot of intensity (number of electrons) as a function of energy lost by the incident electrons in traversing the specimen. There are certain features common to all spectra. In the spectrum shown in Figure 2.1 the peak labelled z is called the zero-loss peak. As is evident by the name this implies a peak due to those electrons which have not lost a detectable amount of energy in passing through the specimen. The zero-loss peak comprises the unscattered electrons as well as

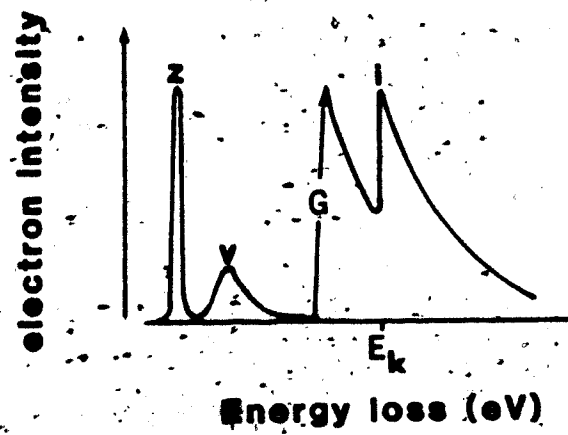


Figure 2.1 A Typical Electron Energy-Loss Spectrum

elastically scattered electrons. Also included in the zero-loss peak are those electrons which have lost a small amount of energy due to electron-phonon interaction. The zero-loss peak is followed by one or more peaks (peak v in Figure 2.1) which are due to the interaction of the incident electron beam with the valence electrons of the specimen, resulting in plasmon losses and single electron intra- and inter- band transitions. This peak, v , extends over a region of about 10-50 eV in the energy-loss spectrum. Since the cross-section for inelastic scattering is maximum for valence electron excitations and much reduced for higher energy losses corresponding to inner-shell excitations, the spectrum shows a jump in the intensity after peak v due to gain change introduced in the detector assembly, while acquiring the spectrum. The energy lost by the incident beam in ionizing an inner-shell electron appears in the spectrum as a sharp rise in the intensity of energy-loss electrons at $E = E_k$ where E_k is the binding energy of the atomic shells of type k where $k=K,L,M$ etc. The values of E_k for various atoms have been tabulated in the literature (Scott, 1965 and Handbook of Chemistry and Physics, E170). The presence of a peak i in the electron energy-loss spectrum at positions corresponding to the binding energies of inner-shell electrons would indicate the presence of that element in the irradiated area of the specimen defined by the transmitted-beam.

EELS offers a powerful method of elemental analysis by analyzing the characteristic ionization edges of various elements. It is particularly useful for the quantitative assessment of low atomic number elements (belonging to the first and second rows of the periodic table) where other methods based upon X-ray production are inapplicable due to low yield of photons (Egerton, 1978). However, the raw energy-loss spectrum, as shown in Figure 2.1, requires a certain amount of processing before any quantitative conclusions can be drawn about the elemental concentrations.

2.3.1 Spectrum Processing for Quantitative Assessment

The usual procedure required for acquiring an energy-loss spectrum involves the use of a magnetic spectrometer, which disperses the signal into its various energy components, attached underneath the microscope column, which disperses the signal into its various energy components. The transmitted electron beam is made to pass through the spectrometer and into a detector assembly and finally to a multichannel analyzer

wherein the electrons are accumulated in different channels corresponding to increasing energy losses. A microcomputer can be used as a multichannel analyser and programmed for the acquisition, storage, display and processing of an energy-loss spectrum (Egerton and Kenway, 1979). In an energy loss spectrum the logarithm of intensity is usually displayed as a function of energy-loss, to accommodate the large variation in intensity in different channels. (For example, the zero-loss peak has very large intensity compared to the intensity of ionization edges).

The first step in the processing of an energy-loss spectrum requires the calibration of the energy axis in electron volts. This can either be performed manually or by computational methods. Manual calibration requires the identification of another prominent peak besides the zero-loss peak. In the case of carbon-supported specimens the prominent K-edge of carbon can be used for this purpose. However, automatic calibration can also be performed by using a program to identify the first maximum intensity value in the displayed spectrum, which is taken as the energy value for the zero-loss peak, i.e. as $E=0$. The energy loss scale is usually linear, having a fixed number of electron volts per channel, for a certain incident energy so the microcomputer automatically performs the calibration of energy axis (Egerton, 1980a).

It is found that the intensity in different channels, for losses greater than about 50 eV, decreases monotonically until it reaches the ionization energy of a particular atomic electron. For moderately thin specimens (<50 nm) this 'background' intensity is essentially due to single valence electron excitations. However for thicker specimens a number of successive losses e.g. multiple plasmon scattering can become a predominant mode of scattering. The technique of deconvolution, for obtaining the single scattering profile beyond the ionization edge by the removal of mixed scattering contribution, is discussed in Appendix 1.

For biological specimens, of the order of 20 nm thick, the multiple plasmon losses are not significant but the background due to single-electron excitations must be removed for quantitative estimations. Background stripping can be performed by a method due to Egerton who realised that the decrease in background is linear on a log-log plot of intensity and energy loss and suggested that the intensity underlying the ionization edge assumes a power law of the type $A E^{-r}$ where A is a constant and r lies between 2 and 6

(Egerton, 1975). The actual subtraction of the background can also be performed computationally by defining a region preceding the ionization edge, typically 50–100 eV in range; if upper and lower bounds of this region are denoted by E_u and E_l and if $E_m = (E_u + E_l)/2$ then A and r can be obtained using the formulae (Egerton, 1980b):

$$A = (I_l + I_u)(1-r) / (E_u^{1-r} - E_l^{1-r})$$

$$r = 2 \log(I_l/I_u) / \log(E_u/E_l)$$

where I_l and I_u respectively are measured by integrating the background over the ranges E_l to E_m and E_m to E_u . The background extrapolated by means of these formulae can then be subtracted from the acquired spectra.

It is found that the signal to background ratio and the energy resolution of the spectrometer are improved by decreasing the angular range of the cone of electrons passing through the specimen (Wittry et al., 1969; Egerton et al., 1976). The angular range can be reduced by inserting the objective aperture which would exclude all those electrons which have angles of scattering greater than a certain value α . However, the angular range α cannot be indefinitely decreased as it would result in reduced signal-to-noise ratio. Use of an aperture usually permits most of the inelastically scattered electrons to pass through but restricts the elastically scattered electrons which have, on average, a higher angle of scattering.

Quantitative estimation of elemental concentration requires the summation of intensity values corresponding to different channels over a certain energy range, Δ , beyond the ionization edge. The range of integration, Δ , is usually called the energy window and a limited range of integration reduces the possibilities of errors in background extrapolation (Egerton, 1978). The concentration of an element (number of atoms per unit area) in the irradiated area of the specimen can be determined using the following formula (Egerton, 1978):

$$N \approx \frac{1}{G} \frac{I_k(\alpha, \Delta)}{I_l(\alpha, \Delta)} \cdot \frac{1}{\sigma_k(\alpha, \Delta)} \quad (2.5)$$

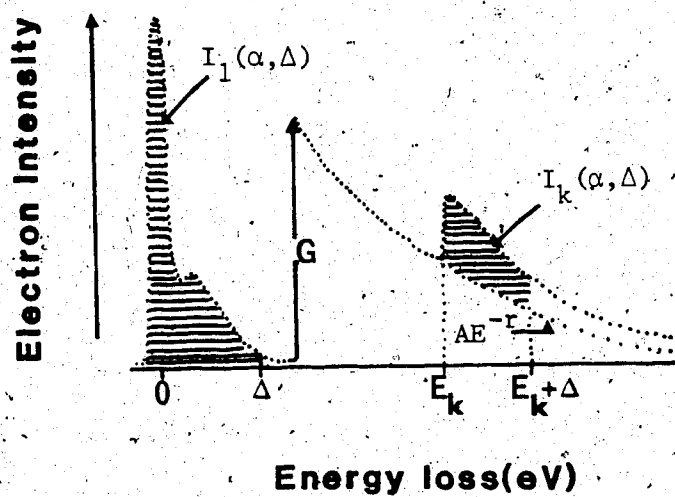


Figure 2.2 A Schematic EEL Spectrum Illustrating Measurement of Areas for Quantitative Estimation

where $I_k(\alpha, \Delta)$ is the integrated intensity of a k-shell electron ($k = K, L, \text{etc.}$) beyond the ionization edge over an energy window Δ for all the electrons scattered through an angle less than α . $I_1(\alpha, \Delta)$ is the area measured from the low-loss region of the spectrum and it allows for an approximate cancellation of the valence-electron contributions. G is the gain change introduced during spectrum acquisition. $\sigma_k(\alpha, \Delta)$ is the partial cross-section for the ionization of an electron in shell k . The partial cross-section can be calculated for a particular value of α and Δ and initial electron energy E_0 . Two different types of programs can be used for its calculation which either employ Hartree-Slater wave functions (Leapman et al., 1980) or hydrogenic approximation (Egerton, 1979b).

On the other hand, if the specimen has been deconvoluted beyond the ionization edge for the removal of valence electron contribution (see Appendix 1), the following equation should be used instead of equation 2.5 for determining N :

$$N = \frac{1}{G} \frac{I_k^s(\alpha, \Delta)}{I_0} \cdot \frac{1}{\sigma_k(\alpha, \Delta)} \quad (2.6)$$

where $I_k^s(\alpha, \Delta)$ is the area under the deconvoluted single-scattering profile beyond the ionization edge up to the energy window Δ and I_0 is the area under the zero-loss peak.

2.3.2 Estimation of Specimen Thickness

The probability of n inelastic collisions of an electron, while passing through a specimen of thickness t , depends upon the mean free path for inelastic collision and is given by the following Poisson equation (Raether, 1965):

$$P_n\left(\frac{t}{\lambda_{in}}\right) = \frac{1}{n!} \left(\frac{t}{\lambda_{in}}\right)^n e^{-t/\lambda_{in}} \quad (2.7)$$

On the basis of this equation, one can derive the following equation for the estimation of thickness:

$$\frac{t}{\lambda_{in}} = \ln(I_t / I_0) \quad (2.8)$$

where I_0 represents the elastic contribution (area under zero-loss peak) and I_t represents the total area under the spectrum (elastic and inelastic contribution). The mean

free path for inelastic scattering for biological specimens is taken to be about 100 nm for 80 keV electrons. Equation 2.8 can therefore be directly used for estimating the thickness of the specimen by measuring the total elastic and inelastic contribution to the spectrum.

2.4 EELS and Radiation Damage

As is clear from the above discussion, electron energy-loss spectroscopy exploits the information present in inelastically scattered electrons. Energy deposited by these electrons may cause structural and/or chemical changes to the specimen. If the specimen is exposed to the electron beam for a certain duration of time and the spectra are acquired from the same specimen area at regular intervals, then the changes in the specimen composition could be detected by analysing these spectra. Monitoring these changes in a series of spectra would indicate the process whereby radiation damage proceeds in the specimen.

Spectral changes in the low-loss region of the energy-loss spectrum were observed by Isaacson et al. (1973). Information about the mass loss due to irradiation can be obtained by monitoring changes in the ionization edges of various elements present in the specimen. After subtraction of the background, the concentration of an element can be determined using equation 2.5 or 2.6. Moreover, in radiation damage studies one is mainly interested in relative changes in concentration and not the absolute values of concentration, so this obviates the necessity of knowing the partial cross section, $\sigma_k(\alpha, \Delta)$. The relative concentration, $N(R)$, can then be determined using equation 3.6 of the next chapter.

2.5 Electron Diffraction

The elastically scattered electron waves from a crystalline specimen interfere constructively in such a manner that the scattered radiation is reinforced only in certain specific directions (defined by Bragg's law), leading to the formation of a diffraction pattern.

One can visualize arrays of regularly arranged points in a three-dimensional space which form the lattice of a crystal structure; the molecules superimposed upon this lattice

would be regularly arranged in an orderly manner in a three-dimensional space. In other words, a crystal can be looked upon as a convolution of the molecule with the lattice. The basic principles of the application of Fourier series to diffraction patterns and to the representation of crystal structures were first recognized by W.H. Bragg, so it has been known for a long time that a diffraction pattern is a Fourier transform of the crystal structure. Therefore, a diffraction pattern of a crystal must be a product of the diffraction pattern of a molecule (molecular transform) and the diffraction pattern of the lattice (i.e. reciprocal lattice). This statement is an immediate consequence of the convolution theorem (Blundell and Johnson, 1976). Intensities of various spots in a diffraction pattern and their relative disposition uniquely define the diffraction pattern of a crystalline structure. The relative disposition of diffraction spots is entirely dependent upon the Fourier transform of the lattice, whereas the intensities of diffraction spots are dependent upon the molecular transform. The Fourier transform of a molecule varies continuously over all reciprocal space and its product with the reciprocal lattice results in its sampling at the lattice points. So, the structural information about a molecule is contained in all the diffraction spots and a Fourier synthesis performed with the aim of structure determination should include the intensities belonging to all the diffraction spots.

If there are N atoms placed in a unit cell at distances $\vec{r}_1, \dots, \vec{r}_n$ from the origin and if their atomic scattering factors are f_1, \dots, f_n then the molecular transform is given by:

$$M(\vec{S}) = \sum_{j=1}^N f_j \exp(2\pi i \vec{r}_j \cdot \vec{S})$$

where \vec{S} is a vector in the reciprocal space, analogous to \vec{r} in the real space. As such, the transform of a single molecule would be too weak to be observable but electron waves scattered from successive unit cells of the crystal, having a path difference equal to an integral multiple of 2π , combine together constructively and reinforce the resultant intensity, which thence becomes observable. However, the molecular transform decreases with increasing angle of scattering due to the falling nature of atomic scattering factors with increasing angle of scattering. The intensity of diffraction spots, therefore, decreases with increasing spatial frequency in the reciprocal space. If a crystal is well ordered (and the structure is periodic down to very small interplanar spacings), it produces a diffraction pattern which extends to very high spatial frequencies. On the other hand, if the structural periodicities are confined to gross structural features only, the intensities of

diffraction spots from such a crystal would be confined to small spatial frequencies. The molecular transform in such a crystal is still the same but, due to disorder, the reinforcement of waves, belonging to different unit cells, from the different parts of the molecule does not occur and the sampled intensity in the Fourier space rapidly declines.

Energy deposited by inelastically scattered electrons may cause structural damage to the crystal. Damage to crystalline specimens can be evaluated by electron diffraction (Glaeser et al., 1969). Various affects such as, broadening of spots, change in interspot distance and/or reduction in the intensity of diffraction spots can be seen as a result of radiation damage. Loss in the intensity of diffraction spots implies some kind of loss in the inherent periodicity of the crystal structure. Since the molecular transform depends upon the atomic scattering factors of various elements present in the unit cell, radiation damage would hence affect the molecular transform and the intensity of a particular diffraction spot would decrease. At the same time energy deposited by the electron beam may cause reorientation of parts of a molecule (for example, rotation of the bonds between the peptide linkage and α -carbon atom in a polypeptide). Such a reorientation of molecular parts does not necessarily have to be identical in all the molecules and so the waves scattered from different unit cells would no longer be in phase and a reduction in the intensities of diffraction spots would occur.

Radiation damage at a particular structural level can, of course, be assessed by monitoring changes in the intensity of a diffraction spot whose spatial frequency corresponds to the inverse of the interplanar spacing existing in the crystal structure (Glaeser et al., 1969) but the purpose of such a study is not to accurately and precisely predict the breaking of individual bonds. Rather, it provides information which when used in conjunction with information obtained from, for example, electron energy-loss spectroscopy, can lead to the interpretation and understanding of various mechanisms possible for the damage process itself.

CHAPTER III

COMPARATIVE STUDY OF RADIATION DAMAGE BY ELECTRON DIFFRACTION AND

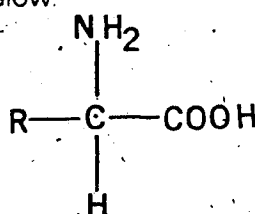
EELS

3.1 Introduction

In examining the interaction between an electron beam and a specimen from the standpoint of radiation damage, electron diffraction and electron energy loss spectroscopy offer powerful techniques. Whereas, EELS can be applied to both, crystalline and non-crystalline specimens, the use of electron-diffraction is restricted to crystalline specimens. In a crystal the atoms or the molecules are regularly arranged in a repetitive manner around the lattice points. The presence of this type of crystalline regularity is responsible for the formation of diffraction spots in an electron-diffraction pattern. If the orderliness of the crystalline structure decreases, due to any cause, its effect can be noticed in the intensities or the positions of the diffraction spots. In other words, any change in the crystal structure which constitutes a change from its original or native state can be monitored by analysing the changes in the intensities or the positions of the diffraction spots. The study of radiation damage by electron-diffraction is the study of structural damage sustained by the specimen due to increasing disorderliness.

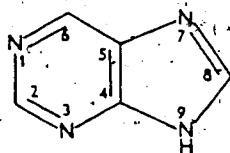
As discussed in the previous chapter, an incident electron may be scattered by an inner-shell atomic electron of the specimen. If the resultant energy transfer to the inner-shell electron is in excess of its ionization energy, it makes a transition to an empty energy level. Such an event appears in the energy-loss spectra as an abrupt rise in the intensity at an energy-loss equal to the inner-shell ionization energy. Since these ionization energy values are characteristic of the scattering element, their presence in the irradiated area can be ascertained by observing their ionization edges in the energy-loss spectra obtained from a specimen. The area under such a peak in an energy-loss spectrum is proportional to the number of atoms per unit irradiated area of the specimen. However, electron irradiation damage may cause some chemical changes to the specimen. Escape of a particular element due to bond rupture may be established by monitoring changes in its characteristic edge in the energy-loss spectra e.g. by calculating the changes in elemental concentration.

The ratio of elastic to inelastic scattering increases with increasing atomic number and radiation damage is most severe in the case of biological molecules (those molecules which are a part of living organism and occur in nature as such). Amino acids are the basic building blocks of large protein molecules. An amino acid consists of an amino group, a carboxyl group, a hydrogen atom and a distinctive R group bonded to a carbon atom called α -carbon atom. The R group is referred to as a side chain. Twenty kinds of side chains resulting in twenty different amino acids are found in proteins. The general molecular formula of an amino acid is shown below:

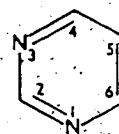


Another important group of biomolecules are called nucleotides, which participate in nearly all biochemical processes. Nucleotides consist of a nitrogenous base, a sugar and one or more phosphate groups. The nitrogenous base is a purine or a pyrimidine derivative. The three pyrimidines are cytosine, uracil and thymine and two major purines are adenine and guanine. The molecular formulae of a purine and a pyrimidine are shown below:

purine



pyrimidine



In this chapter will be reported a comparative study of radiation damage by electron diffraction and EELS on some amino acids and nucleic acid bases. An assessment of the mechanism of radiation damage will be made on the basis of the known crystal and molecular structure of these compounds.

3.2 Experimental Details.

Electron-diffraction studies were conducted on four amino acids: glycine, valine, methionine and cysteine; four nucleic acid bases: adenine, thymine, cytosine and uracil; and on the compound cystine.

3.2.1 Specimen Preparation

These compounds were purchased from the Sigma Chemical Company and all the compounds were found to form good single crystals upon crystallization. Problems were encountered initially in the specimen preparation since these compounds were found to form thick crystals. However, by repeated trials, the proper amount of solute was determined which gave rise to suitable crystals. Optimum amounts of these compounds were then dissolved in water or in other solvents (Table 3.1 gives the list of solvents used for various compounds) and tiny drops of these solutions were deposited by a dropper on different carbon coated copper grids. The specimens were covered to protect them from dust and any other extraneous material and were allowed to dry in air.

3.2.2 Electron Microscopy

The diffraction patterns of glycine were recorded on a Philips 300 electron microscope operated at 100kV and equipped with a liquid nitrogen anti-contamination device. As a precautionary measure the filament was kept under-saturated and small condenser apertures were used: 50 μ m first condenser aperture and 20 μ m second condenser aperture, in order to maintain low electron doses. By operating the microscope in the diffraction mode and by defocusing the first intermediate or diffraction lens the specimen was examined to find a suitable area. In order to minimize radiation damage prior to the commencement of the recording of diffraction patterns, the beam was immediately blocked off by inserting a disk into the beam path (fixed in one of the grooves of the condenser aperture) after locating a suitable area. The diffraction patterns were recorded on Kodak 4489 high speed films. The beam block was taken out after bringing in a film into the camera chamber. A series of diffraction patterns was then recorded at different time intervals. In all cases, a visual inspection of the diffraction pattern was made before actually terminating the recording.

Table 3.1 Solvents used for the Crystallization of Various Compounds

<u>COMPOUND</u>	<u>SOLVENT</u>
1. Glycine	Water
2. Valine	Water
3. Methionine	Ethanol/Water
4. Cysteine	Water
5. Cystine	Ammonium Hydroxide and Acetic Acid
6. Uracil	Water
7. Thymine	Water/Ethanol
8. Cytosine	Methanol
9. Adenine	Ethanol

For the determination of lattice spacings the camera length was calibrated by a standard specimen of gold of known lattice spacings. After the recording of the diffraction pattern, and without altering any setting of the microscope, the specimen was taken out to be replaced by a gold coated copper grid and its diffraction pattern was recorded.

For the calculation of electron dose, the microscope was switched to magnification mode at some known magnification and an image of the spot was recorded on Kodak electron image film 4489 for an estimation of the optical density.

Electron-diffraction and electron energy-loss experiments on all other compounds were conducted on a JEM 100B electron microscope at 80kV accelerating voltage. This microscope was also equipped with a liquid nitrogen anti-contamination device. Electron-diffraction experiments were conducted on all the compounds and electron energy-loss measurements were conducted on all but glycine, valine and cystine. The diffraction measurements were performed in a manner similar to the one described above for glycine. However, after finding a suitable area of the specimen by defocusing the intermediate lens the beam was cut off by the grid bias control of the microscope and the diffraction patterns were recorded on electron image plates. Electron dose was calculated by measuring the beam current (with no objective aperture in the beam path) using a Faraday cup located at the screen level of the microscope. The spot at the specimen level was kept large by defocusing the condenser 2 lens and the spot size was recorded by switching the microscope to imaging mode at a calibrated magnification of 10,000.

3.2.3 Electron Energy-Loss Spectroscopy

The electron energy-loss spectra were recorded by first finding the specimen in the diffraction mode as described above; then the beam was cut off by the grid bias control and the microscope was switched to "high-resolution-diffraction" mode by operating the diffraction control knob. The projector lens is turned off in the high resolution mode and a diffraction pattern of camera length of a few millimeters is formed at the object plane of the spectrometer, which lies close to the screen level. The objective aperture 3 was then inserted (corresponding to a semi-angle α of 8.3 mrad).

The spectrum was focused at the image plane of the spectrometer by changing the intermediate lens current to a predetermined value of about 0.0571A with the help of the diffraction-focus control. The specimen was then irradiated by bringing back the grid bias control to the previous position and simultaneously the acquisition of the spectra was started in the TN-1710 multichannel analyser (MCA). The spectrum was acquired in 1024 channels and the dwell time (the time for which the data is stored in each channel) was 20ms so the recording of one spectrum at a particular dose was performed in about 20s. Spectra were recorded in four different buffers of the MCA, each of 1024 channels, corresponding to increasing irradiation doses. The spectra were then transferred onto a floppy disk and the buffers emptied for the further recording of spectra.

To investigate both structural and chemical changes in an irradiated area of the specimen, it was necessary to conduct these measurements simultaneously, combining the recording of a diffraction pattern and the acquisition of the energy-loss spectra. In the diffraction mode of the microscope, the diffraction control knob was alternately switched between the high-resolution or 'projector off' condition to the 'projector on' condition. In other words: after recording a diffraction pattern as mentioned before the diffraction control knob was changed to high-resolution mode, objective aperture 3 was inserted into the beam path, the intermediate-1 lens current was changed to 0.0571A with the diffraction-focus knob and a spectrum was acquired. After acquiring the spectrum, the diffraction control knob was returned to the previous position, the objective aperture was withdrawn and the diffraction pattern focused for recording the next diffraction pattern.

All the recorded spectra were then stored on the floppy disk for subsequent analysis and all the exposed Kodak 4489 films and electron image plates (belonging to a series of diffraction patterns recorded at increasing irradiation), simultaneously developed in Kodak D-19 developer. The developer was diluted to one half of its original concentration; all the films and plates were developed at 20^o C for four-minutes with continuous agitation (according to Kodak's specifications). The plates were then rinsed in distilled water and transferred to Kodak rapid fixer for a fixing time of four minutes.

3.2.4 Analysis of Electron Diffraction Patterns

To assess the effect of radiation damage on the crystallinity of a particular compound, it is necessary to monitor the changes in the intensity of certain diffraction spots with increasing dose. Densitometer traces were obtained of the spots corresponding to different spatial frequencies, from each diffraction pattern recorded at increasing dose. The area under a densitometer peak was measured (above the background) to yield the intensity of the spot in relative units.

Lattice spacings corresponding to different diffraction spots were determined by first finding the camera length from the diffraction pattern of gold. A polycrystalline specimen of gold gives rise to sharp Debye-Scherrer rings, as shown in Plate 3.1. The following standard equation was used to determine lattice spacings:

$$R d = L \lambda \quad (3.1)$$

where R is the distance of a particular spot from the central spot of the diffraction pattern, L is the camera length, λ is the wavelength of electrons at a particular accelerating voltage and d is the lattice spacing of the plane corresponding to that diffraction spot. The lattice spacings, d , of different rings of the diffraction pattern of gold are known, so by using equation 3.1 the camera length L can be determined. All other quantities are known in equation 3.1, so by substituting the value of camera length, the lattice spacing, d_{hkl} of a spot having h , k and l as Miller indices can be determined.

As an example of the above method we consider the diffraction pattern of uracil, which is shown in Plate 3.2. The diameter of the 111 ring in the diffraction pattern of gold was found to be 10.85 mm and since gold forms cubic crystals having unit cell dimension of 4.070 Å, the value of d_{hkl} can be determined using:

$$d_{hkl} = \frac{a}{\sqrt{h^2 + k^2 + l^2}} \quad (3.2)$$

$$d_{111} = \frac{4.07}{\sqrt{1^2 + 1^2 + 1^2}} = 2.3498 \text{ Å}$$

Therefore, the camera length can be found from equation 3.1.

To determine the lattice spacing for the spot marked A in the Plate 3.2, the distance AA' was determined from the negative of this diffraction pattern and was found to be

Plate 3.1 Diffraction Pattern of Gold





Plate 3.2 Diffraction Pattern of Uracil

equal to 5.08 nm, therefore the d value corresponding to this spot will be equal to:

$$d_A = \frac{2 \times 304.9 \times 0.0418}{5.08} = 5.02 \text{ \AA}$$

Similarly, the d value for any spot in the diffraction pattern can be determined from equation 3.1 by simply substituting the $2R$ value of the corresponding spot from the diffraction pattern.

3.2.5 Calculation of Electron Dose

The irradiation received by the specimen is often called the dose and is usually measured in the units of electrons per square angstrom or in Coulombs per square metre. Electron doses in these experiments were calculated by two different methods. For glycine the dose was calculated by the optical density method (Unwin and Henderson, 1975). The doses for other compounds were calculated by measuring the electron beam current with a Faraday cup installed at the screen level in the JEM 100B electron microscope.

In the optical density method one measures the blackening, D , of the photographic film which bears a simple relationship to the total number of electrons which have produced the blackening. The total number of electrons incident on the photographic film is proportional to the product of the intensity of the electron beam and the time during which the film is exposed to the beam. The product is hence proportional to the optical density. Optical density is defined as the logarithm of the ratio of the intensity I_0 of the incident beam of light and I_t the intensity of the light transmitted by the blackened spot on the photographic film, i.e.:

$$D = \log_{10} (I_0 / I_t) \quad (3.3)$$

The optical density of an exposed film was determined by comparing its densitometer trace with that of a calibration step wedge provided by Kodak. A chart was also provided by Kodak showing the variation of optical density with electron exposure, as is shown in Figure 3.1 for a Kodak 4489 film (curve A). By knowing the optical density of the exposed photographic film, the dose at the plate level was determined from the graph between the optical density and electron exposure. For example, after recording the diffraction pattern of glycine a photographic film was exposed to electron beam for

128 seconds at a magnification of 25000. The densitometer trace of the film was compared with the densitometer trace of the step wedge which gave an optical density of 0.05. From the graph between optical density and exposure it was determined that an optical density of 0.05 corresponded to a dose of 0.55 electrons/ μm^2 at the plate level. The dose rate, the number of electrons per square angstrom per second, at the specimen level was found to be equal to:

$$\frac{0.55 \times (25000)^2}{128 \times 10^8} = 0.027 \text{ e}/\text{\AA}^2/\text{s}.$$

Electron dose for all the diffraction patterns belonging to the series were then obtained by multiplying the dose rate with the cumulative time spent between successive recordings of diffraction patterns.

In the second method of dose calculation, the beam current was measured by a Faraday cup. The dose was calculated using the following equation:

$$D = \frac{8.0 \times 10^4 \times I \times M^2 \times t}{d^2} \quad (3.4)$$

Where,

I = Beam current in A,

d = Diameter at the plate level in mm,

M = Magnification,

t = Time in seconds, and

D = Dose in electrons per square Angstrom.

The radiation damage series for the compound thymine was recorded with a beam current of 0.053×10^{-10} A; the spot size on the plate at the calibrated magnification of 10000 was 60 mm.

$$D = \frac{8.0 \times 10^4 \times 0.053 \times 10^{-10} \times 10^8}{60 \times 60} t = 0.011 t \text{ e}/\text{\AA}^2$$

Hence, the cumulative dose sustained by the specimen before the recording of a diffraction pattern or the acquisition of an energy-loss spectrum was obtained by substituting the total irradiation time in seconds in the above expression for dose.

- A KODAK EM Film 4489
- B EASTMAN Film 5302
- C KODAK High Resolution Plate

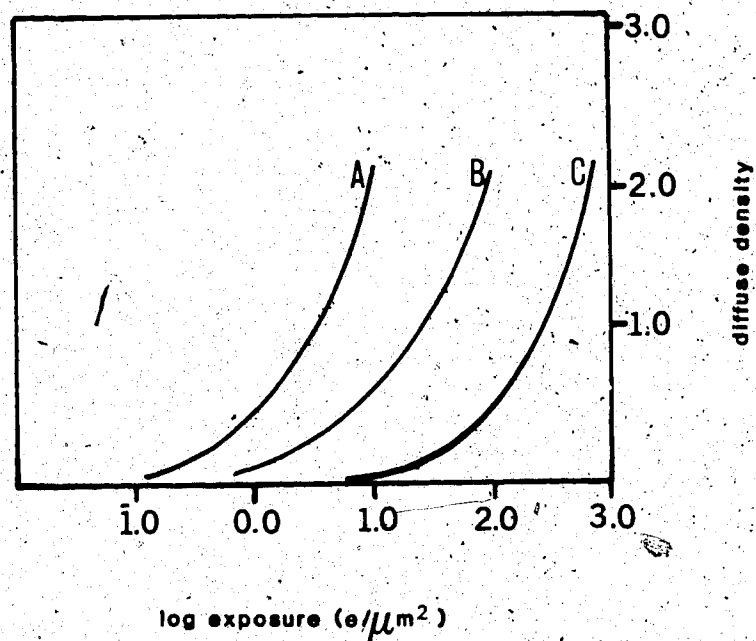


Figure 3.1 A Plot between Optical Density and Electron Exposure

3.3 Processing of Electron Energy-Loss Spectra

The processing of the electron energy-loss spectra involves several steps prior to the determination of the number of atoms of an element in the irradiated area of the specimen.

The energy-loss axis of the spectrum was first calibrated. It can either be done manually or computationally by the microprocessor itself. Manual calibration requires the identification of the zero-loss peak and another prominent feature in the energy-loss spectrum. Since all the specimens were supported on a carbon-coated grid, the common feature which occurred in the energy-loss spectra (besides the zero-loss peak) was the K-shell ionization edge of carbon at about 283 eV. Computational calibration required locating the zero-loss peak either by eye or by a computer program, the calibration was performed by the microprocessor itself (Egerton, 1980a).

After the calibration of the energy axis the background was subtracted computationally, as described in Chapter 2, by making use of an empirical formula due to Egerton (1978). The concentration of a particular element was then determined by computing the area under the peak above background (that is the sum of the intensities in different channels beyond the ionization edge) over a certain energy window Δ , which was taken to be between 50 and 70 eV. The area under the low-loss region of the spectra, up to the same energy window Δ , was also computed and the following formula was used to determine the concentration (number of atoms per square metre) N , of a particular element (Egerton, 1978):

$$N \approx \frac{1}{G} \left[\frac{I_k(\alpha, \Delta)}{I_1(\alpha, \Delta)} \right] \cdot \frac{1}{\sigma_k(\alpha, \Delta)} \quad (3.5)$$

where $I_1(\alpha, \Delta)$ is the area measured from the low-loss region of the spectrum, α is the collection semi-angle determined by the objective aperture, $I_k(\alpha, \Delta)$ is the area above the background above the k-shell ionization edge ($k=K, L, M, \dots$) and $\sigma_k(\alpha, \Delta)$ is called the partial cross-section for a particular shell of the element, which can be computed. The factor G in the denominator of equation 3.5 accounts for the gain change of the detector between the low and high energy regions of the spectra.

Absolute value of N is not needed in radiation damage studies, so one can simply determine the ratio of the initial concentration of a particular element to the concentration

at higher doses. This also obviates the need of knowing the partial cross-section $\sigma_k(\alpha, \Delta)$. Therefore, if the initial concentration is denoted by $N(0)$ and the concentration after a dose D becomes $N(D)$, then the relative concentration $N(R)$ will be given by:

$$N(R) = \frac{N(D)}{N(0)} = \frac{I_k^D(\alpha, \Delta)}{I_1^D(\alpha, \Delta)} \cdot \frac{I_1^0(\alpha, \Delta)}{I_k^0(\alpha, \Delta)} \quad (3.6)$$

where, the superscripts 0 and D on I_k and I_1 represent their initial values and their values at a dose D respectively.

3.4 Results

That the electron irradiation damage does cause undesirable changes to the crystal structure becomes evident simply by observing a diffraction pattern for a period of time. For example, Plate 3.3(a) shows the diffraction pattern of glycine which was recorded at a dose of 13 C m^{-2} . Also shown are the diffraction patterns recorded at doses of 140 C m^{-2} , 300 C m^{-2} , and 400 C m^{-2} in Plate 3.3(b) through 3.3(d). This diffraction pattern extended to a spatial frequency of 1.2 \AA^{-1} . Notice the loss in intensity and eventual disappearance of various diffraction spots. Even a dose as small as 16 C m^{-2} (1.0 e\AA^{-2}) was sufficient to cause changes in the intensity of some spots.

Likewise, discernible changes can be noticed in an ionization edge of an element in the energy-loss spectrum. In Plate 3.3(e) is shown the electron energy-loss spectrum obtained for adenine. The spectrum shows the number of electrons (intensity) in each channel as a function of energy loss. Intensity is shown on the logarithmic axis for the convenience of display. The two traces shown in this figure were recorded at different doses from the same area of the specimen (upper one was recorded at lower dose). Both traces show four prominent peaks. The peak at the extreme left is the zero-loss peak followed by a peak due to valence electron losses. An abrupt change in the intensity is due to detector (PMT) gain change introduced during the serial recording of the spectra. The first peak following the gain change is carbon K-shell ionization edge and the second peak at about 400 eV is due to nitrogen K-shell ionization. The area under the peak (which gives the number of nitrogen atoms per unit irradiated area of the specimen) is

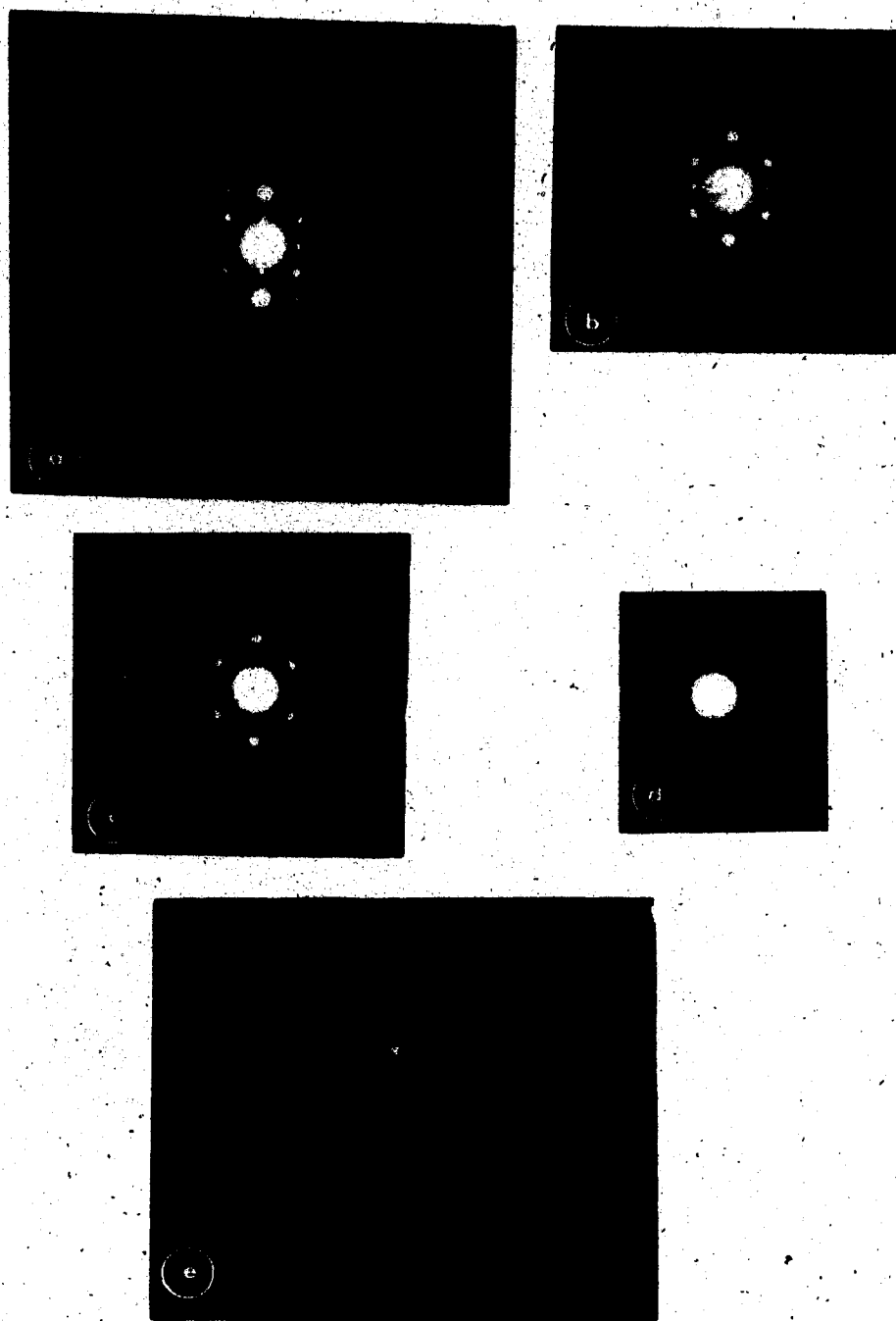


Figure 1. Diffraction Pattern of Glycine at Increasing Doses (a through d) and EEL Spectrum for Adenine (e).

proportional to the integral of the intensities in different channels after the ionization edge. An effect of irradiation can be seen in the lower trace in which a significant reduction has occurred in the intensity of the nitrogen K edge, implying loss of nitrogen from the irradiated area of the specimen.

In relating the changes in the ionization edge and in the intensities of the diffraction spots to radiation damage, the results may be presented graphically. A plot of the loss of intensity of a diffraction spot or the concentration of a particular element as a function of dose (electron irradiation) can be called a dose response curve. A qualitative and quantitative comparison between the dose response curves of different compounds is possible by either of the following two methods. In the 'vanishing point dose' method the intensity of a diffraction spot or the concentration of a particular element is monitored with increasing doses until it stabilizes and no further change in either is observed with increasing doses (Glaeser, 1971 and Kobayashi, 1965). A comparison can then be made by determining the vanishing point dose for different processes of radiation damage. On the other hand, it is seen that, in most of the cases, the intensity and concentration decrease exponentially with increasing doses. Thus, on the basis of the exponential decay of dose response curves one can determine the characteristic dose, $D_{1/e}$. For diffraction measurements $D_{1/e}$ is defined as the dose needed to reduce the intensity of a diffraction spot to $1/e$ of its initial value and for elemental losses it implies the dose required to reduce the content of an element to $1/e$ of its initial concentration.

Structural damage, as assessed from the intensities of the diffraction spots, was found to proceed from the high spatial frequency spots to low spatial frequency spots. The dose response curves plotted for different compounds emphasize mainly the decay in the intensities of high spatial frequency spots.

Figure 3.2 shows the dose response curves for the amino acid glycine in which are plotted the decay curves for 1.05 \AA^{-1} and 1.25 \AA^{-1} diffraction spots. The spots of 0.76 \AA^{-1} and 1.14 \AA^{-1} spatial frequencies are plotted in Figure 3.3 for the compound methionine while the N(R) value for the loss of sulphur atom from methionine is shown in Figure 3.4 as a function of dose. The spots having 0.44 \AA^{-1} and 0.6 \AA^{-1} spatial frequencies from the diffraction pattern of valine are plotted as a function of dose in Figure 3.5. The next two plots are for cysteine and cystine, the plot for cysteine includes

the relative intensities of 0.105 \AA^{-1} , 0.21 \AA^{-1} and 0.32 \AA^{-1} spots as a function of dose and also the relative content of sulphur as measured by EELS while for cystine the relative intensities of 0.37 \AA^{-1} , 0.56 \AA^{-1} and 0.74 \AA^{-1} diffraction spots are plotted.

The following four figures include the response curves for the nucleic acid bases. Figure 3.8 shows the relative intensities of 0.35 \AA^{-1} , 0.55 \AA^{-1} and 0.71 \AA^{-1} spots from the diffraction pattern of uracil also included in this figure is the $N(R)$ value for the loss of oxygen from uracil with increasing irradiation. In the dose response curve for thymine which is shown in Figure 3.9 we notice that the loss of oxygen as well as loss in the intensities of 0.507 \AA^{-1} and 0.76 \AA^{-1} diffraction spots has been plotted as a function of electron irradiation. The curves for cytosine and adenine, Figures 3.10 and 3.11, show the loss of nitrogen and the decay in the intensity of 0.38 \AA^{-1} spot for cytosine and of 0.45 \AA^{-1} spot for adenine.

These curves were used to calculate the characteristic doses for diffraction and EELS measurements which are tabulated in Table 3.2. Also shown are the spatial frequencies of the corresponding diffraction spots within brackets.

3.5 Discussion

The preceding results characterize the trend observed in the radiation sensitivities of certain crystalline amino acids and nucleic acid bases. The sensitivities of these compounds can be explained on the basis of their crystalline and molecular structures.

As pointed out earlier, the process of radiation damage can be discussed in terms of structural and/or chemical damage. Certain features emerge from the characteristic doses tabulated in the Table 3.2. On the basis of the $D_{1/e}$ values for structural damage one can broadly classify these compounds into three categories. Firstly, amino acids were found to be most sensitive to electron irradiation damage while at the other extreme of radiation sensitivity was a purine i.e. adenine. In between these two extremes of radiation sensitivity were pyrimidines. Within amino acids, however, one finds that $D_{1/e}$ ranges between 2 Cm^{-2} (for valine) to 320 Cm^{-2} (for cysteine). The following discussion is based upon the crystal structures of glycine, valine, methionine and cysteine and cystine which were determined by Marsh (1958), Torii and Iitaka (1970), Torii and Iitaka (1973), Harding et al. (1968) and Oughton et al. (1958) respectively.

Table 3.2 Characteristic Doses for Various Specimens

SPECIMEN	DIFFRACTION DATA	EELS DATA
	$D_{1/e} (d_{hkl}^{-1})$ in Cm^{-2}	$D_{1/e}$ in Cm^{-2}
Glycine	118(1.05\AA^{-1}), 76(1.25\AA^{-1})	
Valine	5.4(0.44\AA^{-1}), 2.0(0.6\AA^{-1})	
Methionine	14(0.76\AA^{-1}), 8.0(1.14\AA^{-1})	91 for sulphur loss
Cysteine	320(0.105\AA^{-1}), 128(0.21\AA^{-1})	600 for 15% sulphur loss
Cystine	288(0.56\AA^{-1}), 240(0.74\AA^{-1})	
Uracil	288(0.55\AA^{-1}), 176(0.71\AA^{-1})	200, Oxygen loss
Thymine	272(0.507\AA^{-1}), 122(0.76\AA^{-1})	350, Oxygen loss
Cytosine	528(0.13\AA^{-1}), 208(0.38\AA^{-1})	192, Nitrogen loss
Adenine	2300(0.45\AA^{-1})	2400, Nitrogen loss

3.5.1 Structural Damage to Amino Acids

An essential feature of the crystal structure of all these compounds is hydrogen bonding between the amino and carboxyl groups of the amino acids, which is primarily responsible for holding the lattice together. The other factor which governs the molecular packing is the side chain, R, whose molecular configuration seems to play an important role in describing the radiation sensitivities of these compounds.

In glycine, for example, the side chain consists of a lone hydrogen atom. An incoming electron may deposit more than 200 eV energy to the nucleus of the hydrogen atom, in an elastic encounter. Such a large amount of energy is sufficient to cause the rupture of the $C_{\alpha}-H$ bond in glycine. However, the cross-section for an elastic encounter is extremely small and hence the probability of a direct knock-on damage of C-H bond is negligible. However, the inelastic scattering of an incoming electron with the hydrogen atom, may result in the ionization of the hydrogen atom. The displacement of the hydrogen atom, in this case, would only be possible if the nucleus moves sufficiently far before the reformation of the bond occurs. On the other hand, in valine the side chain consists of $-CH(CH_3)_2$. What is even more probable than the dissociation of the side chain is the rotation of the side chain about the C_{α} bond of the amino acid. Such a rotation of the molecular groups would result in the deterioration of the intensities of diffraction spots making valine an extremely radiation sensitive compound. Such an intra-molecular reorientation would tend to make the diffraction spots belonging to higher spatial frequencies more susceptible to irradiation damage. The long range disorder corresponding to the low spatial frequencies would follow the short range disorder as the displacement or diffusion of molecular fragments or atomic species seems to occur at higher doses.

In methionine, side chain reorientation seems to be somewhat restricted due to two factors. A longer side chain though still susceptible to rearrangement, offers immobility due to steric reasons. Moreover, the presence of a rather heavy element, sulphur, in the side chain also contributes to its greater resistance to change. So, although methionine is more resistant compared to valine it is less resistant compared to glycine in which there is a hydrogen atom instead of the side chain.

In cysteine also, as discussed below, the molecules are bonded together by hydrogen bonds. However, the bondings within and outside the side chain seem to be governing the behavior of cysteine to electron irradiation: its greater resistance to electron irradiation damage can be attributed to the close contact between sulphur atoms and also to the inter- and intra-molecular contacts between sulphur and oxygen atoms. The molecules are stacked such that the sulphhydryl group projects in a direction which is opposite to that of amino and carboxyl groups of the amino acid. So, although the hydrogen bonding between amino and carboxyl groups is as susceptible to radiation damage as it is in other amino acids, the strength provided to the crystal structure by the sulphhydryl group enables the molecule to sustain greater radiation damage before significant loss in the intensities of various diffraction spots occurs.

An interesting feature is observed in the dose response curves of cystine shown in figure 3.7. It is found that the relative intensities of all the reflection spots initially increase slightly before the decay begins. A similar rise in the intensity has been noted in the crystals of α -copper phthalocyanine by Clark et al. (1980) and by Kobayashi et al. (1974). This rise in the intensity can be attributed to dynamical effects or to the increase in the atomic scattering factors which results from the ionization of atomic species. But the increase in the atomic scattering factors should have mainly affected the intensities of the spots corresponding to small spatial frequencies, since for larger $\sin \theta / \lambda$ the change in atomic scattering factor upon ionization is not appreciable. Instead, it seems that some kind of cooperative effect initially takes place, due to some dynamical scattering between the waves diffracted within crystallites. However with increasing irradiation, the disorder in the structure would develop more and more and the effect on the intensities due to dynamical scattering would accordingly decrease resulting in a drop in the intensity after an initial rise.

Notice from Table 3.2 that cystine is considerably more resistant to electron irradiation compared to other compounds discussed so far. The molecules of cystine are stacked in a hexagonal lattice, perpendicular to the c axis. A strong covalent bond exists between the two sulphur atoms which form a disulphide bridge between the two cysteine residues. Besides this covalent linkage each sulphur atom has a close contact with its non-bonded neighboring nitrogen (intra-molecular) and carbon and sulphur

(inter-molecular) atoms. Such a network of intra- and inter-molecular bonds seems to provide a greater resistivity to its crystal structure, compared to that of cysteine.

Irradiation of amino acids could also be discussed in terms of degradation of the molecules into other products of lower molecular weight. Here it is useful to make a comparison with results obtained in radiation chemistry, where solid amino acids (in non-aqueous state) are exposed to different types of radiation (neutrons, γ rays, electrons), at doses comparable to those used in electron microscopy. The radiochemical reactions show considerable complexity but it is possible to extract information which is of direct relevance to the problem of radiation damage (of amino acids) in an electron microscope. Radiolysis of glycine, valine, alanine, cysteine and some other amino acids has been studied by Meshitsuka et al. (1964), Gejvall et al. (1975), Gottschall et al. (1967), and Petterson et al. (1968).

There are two major processes which seem to take place upon irradiation of amino acids: (1) deamination, which involves removal of hydrogen and formation of the corresponding acid without change in the number of carbon atoms and (2) decarboxylation, which results in the formation of an amine and carbon dioxide. As a result of deamination and decarboxylation, the yields of ammonia and carbon dioxide can be measured using chemical techniques. In radiation chemistry a useful quantity for the measurement of different products upon irradiation is the G-value. A G-value is defined as the number of molecules produced, of a particular type, upon the absorption of 100 eV of energy. The G-value for the yield of ammonia, from solid amino acids irradiated in vacuum at room temperature, ranges from approximately 2 to 6 (Garrison, 1968). For sulphur-containing amino acids hydrogen sulphide gas is also formed and the yield of ammonia is slightly lower than that for other aliphatic amino acids (Peterson et al., 1968).

The G-value obtained by radiation chemistry measurements can be converted to an equivalent characteristic dose using the following equation:

$$d_{1/e} = \frac{0.63 \times 100 \times \lambda \times e}{G \cdot E_p} \cdot \frac{\text{bonds}}{\text{volume}} \quad (3.7)$$

where λ is the inelastic mean free path, e is the electronic charge, E_p is the plasmon

energy. The G-value for the release of a particular gas can be related to the scission of a particular bond which needs to be broken for the release of gas (for example, release of ammonia would require scission of C-N bond); the last term in the above equation relates to the number of such bonds initially present in the unit volume of the material.

Using the G-values given in the literature for the release of ammonia and reasonable estimates of λ and E_p (typical values of $\lambda = 50$ nm and $E_p = 20$ eV can be used) the $D_{1/e}$ values were computed for valine and cysteine. The results for such calculations are given in Table 3.3.

For valine $D_{1/e}$ value obtained using equation 3.7 is seen to vary between 27 and 80 Cm^{-2} due to different G-values existing in the literature. The characteristic doses given in the column 5 of table 3.3 are much higher compared to the $D_{1/e}$ values obtained by electron diffraction measurements for high spatial frequency diffraction spots. The characteristic doses of column 5 are comparable to the dose required for the complete fading of the diffraction pattern (for valine, as also determined by Glaeser (1971)) and to the characteristic doses for low spatial frequency diffraction spots (for cysteine). This suggests that the initial damage to the specimen (which mainly reduces the intensities of high spatial frequency diffraction spots) may not be due to deamination of the molecule and some other mechanism (possibly rotation of side chain) is operative at small doses. However, bond scission should become increasingly important at higher doses when, for example, the characteristic dose for the release of ammonia becomes comparable to the characteristic dose for the fading of diffraction spots belonging to small spatial frequencies.

The $D_{1/e}$ value for sulphur loss from cysteine as determined by EELS is seen to be much higher than the $D_{1/e}$ value determined for the release of hydrogen sulphide. This could be due to trapping of hydrogen sulphide in the specimen which when treated to water, for radiation chemistry measurements, would readily dissolve in water. The G-value for the formation of cystine upon irradiation of cysteine was found to be 5.0 (Pettersen et al., 1968). This fairly high G-value indicates that sulphur could still be present in the specimen (in the radiation product cystine), which is also confirmed by the high dose required for sulphur loss (600 Cm^{-2} for the loss of 15% sulphur) as determined by EELS.

<u>COMPOUND</u>	<u>YIELD OF</u>	<u>G-VALUE</u>	$D_{1/e}$ (C m ⁻²) <u>CALCULATED</u>	$D_{1/e}$ (C m ⁻²) <u>DIFFRACTION</u>	$D_{1/e}$ (C m ⁻²) <u>EELS</u>
Valine	Ammonia	2 - 6	27 - 80	28 (complete disappearance) 5.4 (0.44A ⁻¹) 2.0 (0.60A ⁻¹)	
Cysteine	Ammonia	1.8	100	320 (0.105A ⁻¹) 128 (0.21A ⁻¹) 66 (0.31A ⁻¹) 14 (0.52A ⁻¹)	
	Hydrogen sulphide	1.5	117		600 for 15% sulphur loss

Table 3.3 Characteristic Doses Computed from the G-values



3.5.2 Structural Damage to Nucleic Acid Bases

As mentioned before, the pyrimidines were found to be more resistant to radiation damage compared to the amino acids. This increased resistivity of pyrimidines seems to be due to their molecular structure. These compounds possess a ring-like structure made up of carbon and nitrogen atoms. The π electrons, furnished by different atoms forming the pyrimidine ring, are perpendicular to the plane of the molecule, resulting in considerable overlapping between the adjacent π electron clouds and consequent delocalization of these electrons. The energy given to the specimen by the electron beam thus gets shared by different delocalized bonds. Sharing of the excitation energy imparted to the molecule reduces its damaging effect and thus provides a greater resistance to electron irradiation.

A consequence of the delocalization of the π electron clouds is the phenomenon called *resonance* and such conjugated molecules are essentially *resonating* molecules (Pullman and Pullman, 1963). If the bonds were all localized, as are the σ bonds, then the concept of the additivity of bond properties would hold and the total energy of such an unconjugated molecule would be the simple addition of individual bond energies. However, for conjugated molecules such a simple addition of bond energies is not permissible due to the spreading of the electron cloud which experiences repulsion by other σ and π electron clouds and attraction of the nuclei of different atoms. The quantum-mechanical considerations for the calculation of the energy of conjugated molecules yield a quantity called resonance energy, which is the difference in energy between the localized and delocalized structures. Resonance energy also depends upon the number of π electrons contributing to the conjugated structure. Therefore, of greater relevance to the present discussion is the resonance energy per π electron. A large energy difference between the localized and delocalized structures would give the delocalized one greater ground-state energy, and therefore a more stable structure compared to the localized structure. In other words, a greater resonance energy per π electron would provide a gain in stability to the conjugated compound under the electron beam.

The characteristic doses for structural damage tabulated in Table 3.2 for nucleic acid bases are in a specific order. According to which adenine is found to be the most

resistant of all the nucleic acid bases followed by cytosine, uracil and thymine in the order of increasing susceptibility to electron irradiation. This stabilization of the nucleic acid bases is in agreement with the resonance energy calculations of Pullman et al. (Pullman and Pullman, 1963). According to their calculations purines as a whole are characterized by a greater value of resonance energy per π electron compared to pyrimidines, and among the purines, adenine has the highest value of resonance energy per π electron. While amongst the pyrimidines, cytosine has the greatest value of resonance energy per π electron. A similar trend has been observed by Isaacson (1972) from structural energy-loss measurements of damage involving the low loss region of the energy loss spectrum.

3.5.3 Chemical Damage to Nucleic Acid Bases and Amino Acids

However, greater resistivity of the ring structure, due to delocalization of π electrons, does not extend a similar protection to the peripheral atoms attached to the main ring structure. This is evident from the characteristic doses for chemical damage as assessed by electron energy-loss spectroscopy. In the third column of Table 3.2 are the $D_{1/e}$ values for elemental losses. The loss of peripheral atoms (nitrogen and/or oxygen), is seen to be closely related to the fading of the diffraction patterns of these compounds. This, in turn, implies that in nucleic acid bases the deterioration of the crystal structure and losses of different atoms are comparable and competitive processes. The $D_{1/e}$ values for the high spatial frequency spots are comparable to the $D_{1/e}$ values for elemental losses, whereas the characteristic doses for the low spatial frequency spots were found to be much in excess of the $D_{1/e}$ values for elemental losses. This indicates that the high-spatial-frequency damage occurs first and involves the loss of peripheral atoms. It seems that during this period of irradiation the ring structure of the nucleic acid bases is not affected much due to its resonance-enhanced stability. However, this initial stabilization of the ring structure, is only temporary, as is evident by the increasing long range disorder observed from the decay in intensity of small spatial frequency spots.

On the other hand, the loss of sulphur from methionine and cysteine was found to be a fairly gradual process. The comparison of the characteristic doses for the loss of sulphur from these compounds with $D_{1/e}$ for structural damage indicates that the sulphur

loss occurs at comparatively higher doses. Here, structural damage seems to precede chemical damage. It is seen from Table 3.2 that for the small spatial frequency spot (0.105 \AA^{-1}) the characteristic dose for cysteine is 320 Cm^{-2} while only 15% of sulphur loss occurs at a dose which is about twice the characteristic dose for structural damage. Similarly in methionine: the characteristic dose for sulphur loss is considerably higher compared to the characteristic doses for structural damage. This suggests that elemental loss may not be the decisive factor for structural damage in these aliphatic side chain compounds, at small doses, and that rotation of the side chain about the C_{α} atom may be responsible for the loss in intensity of high spatial frequency diffraction spots. However, at relatively higher doses bond scission would become an important cause of radiation damage, as is evident by the characteristic doses calculated from the G-values for the release of ammonia and hydrogen sulphide.

In summary, the behavior of nucleic acid bases and amino acids during electron irradiation was found to be governed by their molecular and crystal structures. Nucleic acid bases were found to be more resistant to radiation damage compared to amino acids and their greater resistance can be attributed to their high resonance energy per π electron. Further, the peripheral atoms surrounding the main pyrimidine ring were found to be more susceptible to damage compared to the ring itself. However, the initial excitation of the molecule by the deposition of energy may lead to the ionization and resonance energy for such excited molecules will differ from their ground state values as calculated by Pullman and Pullman. The stabilization and the tendency to form conjugated molecules of the primary products of irradiation (ions and radicals), would depend upon their own resonance energy values and it does not seem possible to explain the resistivities of damage products on the basis of the ground-state resonance energy values of their parent molecules. Especially, the stability of the structure would seem to diminish considerably after damage has occurred to the ring structure.

As a reasonable hypothesis one can say that the initial stability of amino acids is governed by their side chains, assuming that the effect of hydrogen bonding in maintaining the crystal structure would be almost similar in all these amino acids. This could be true for all those amino acids which possess an aliphatic side chain. However, for the amino acids having aromatic (conjugated) side chains attached to α -carbon atoms (like

phenylalanine, tyrosine and tryptophan) it seems reasonable to expect that the effect of the delocalization of electrons in the side chain would be an important factor in determining their susceptibility to irradiation damage, while the atoms attached to the ring could be vulnerable to damage as found for the nucleic acid bases.

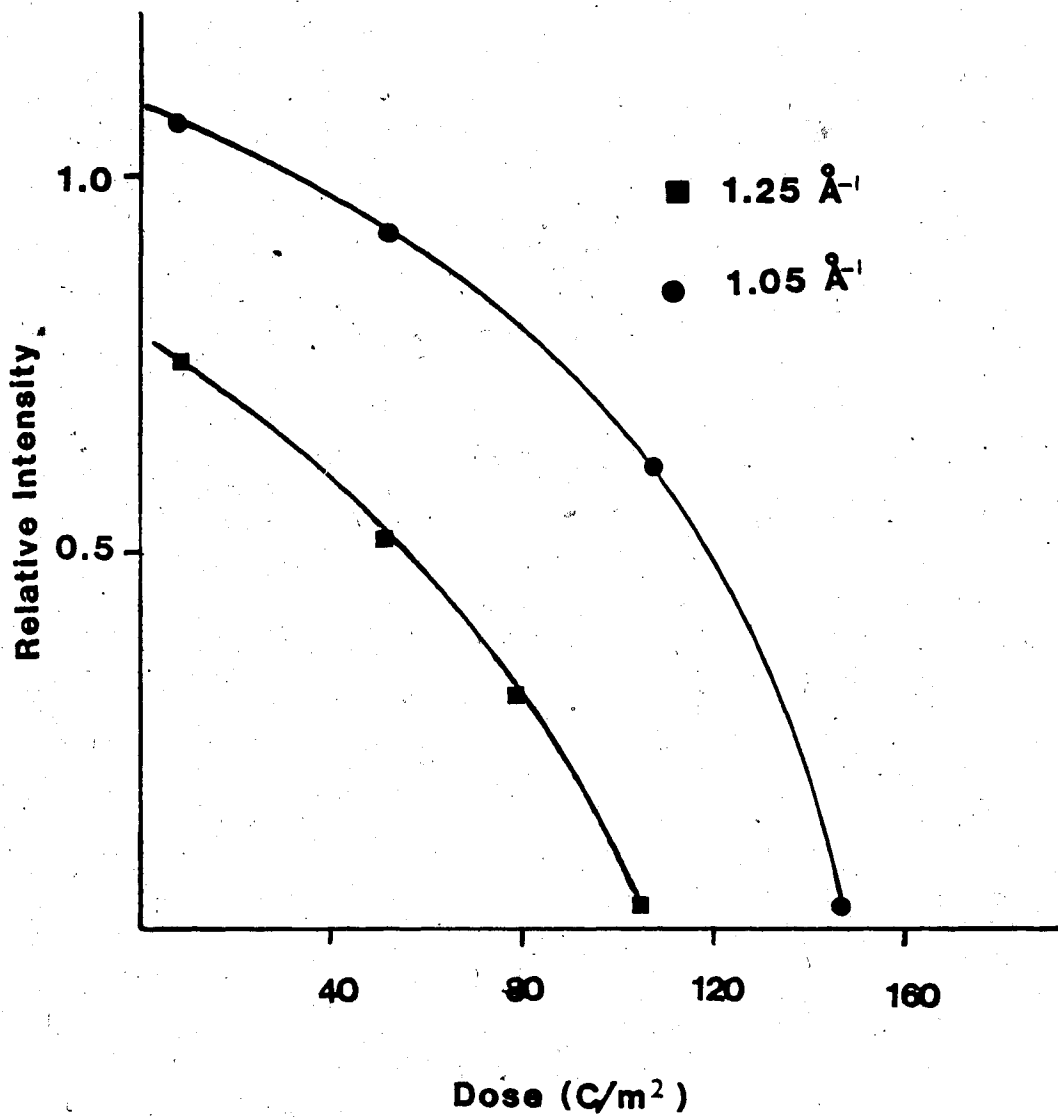


Figure 3.2 Dose Response Curve for Glycine (Diffraction)

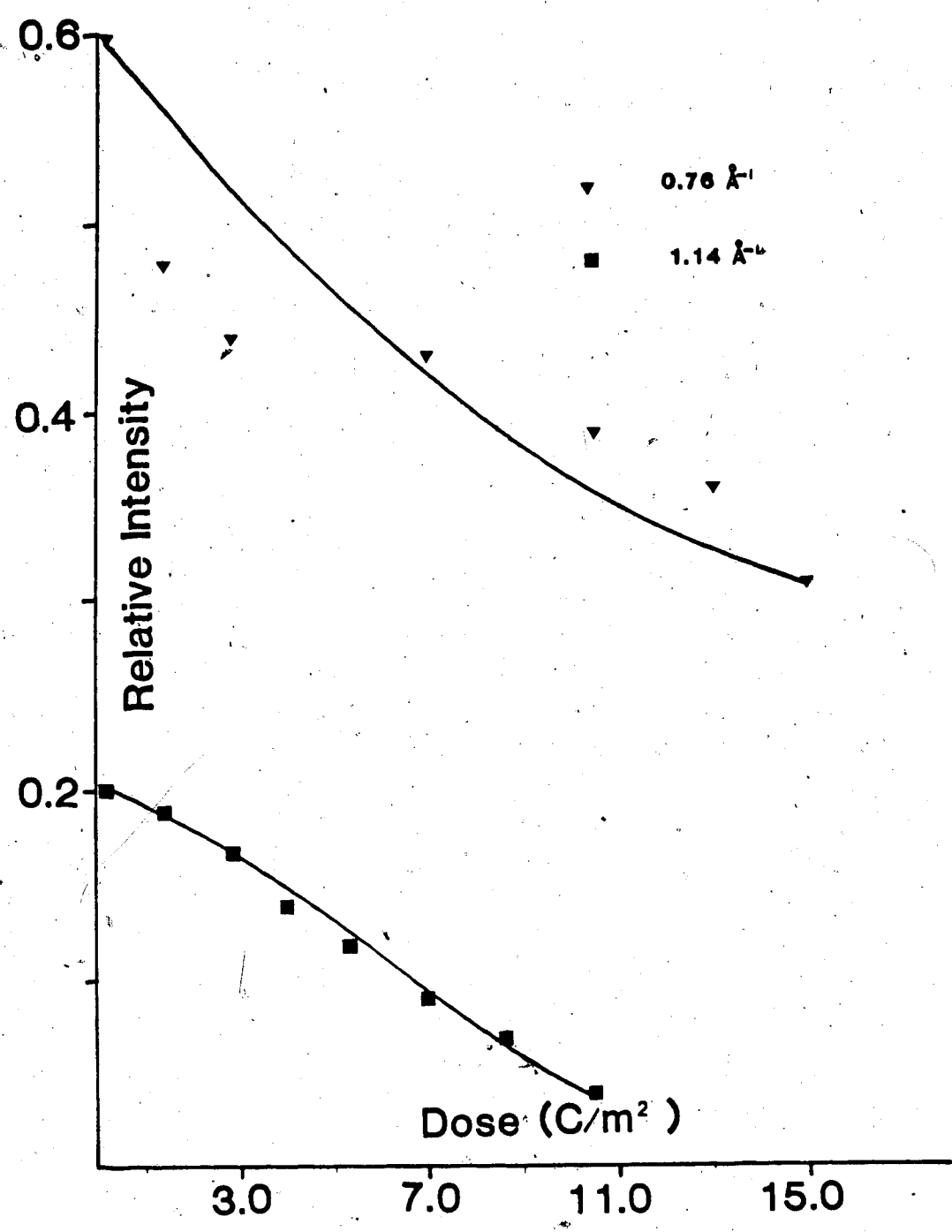


Figure 3.3 Dose Response Curve for Methionine (Diffraction)

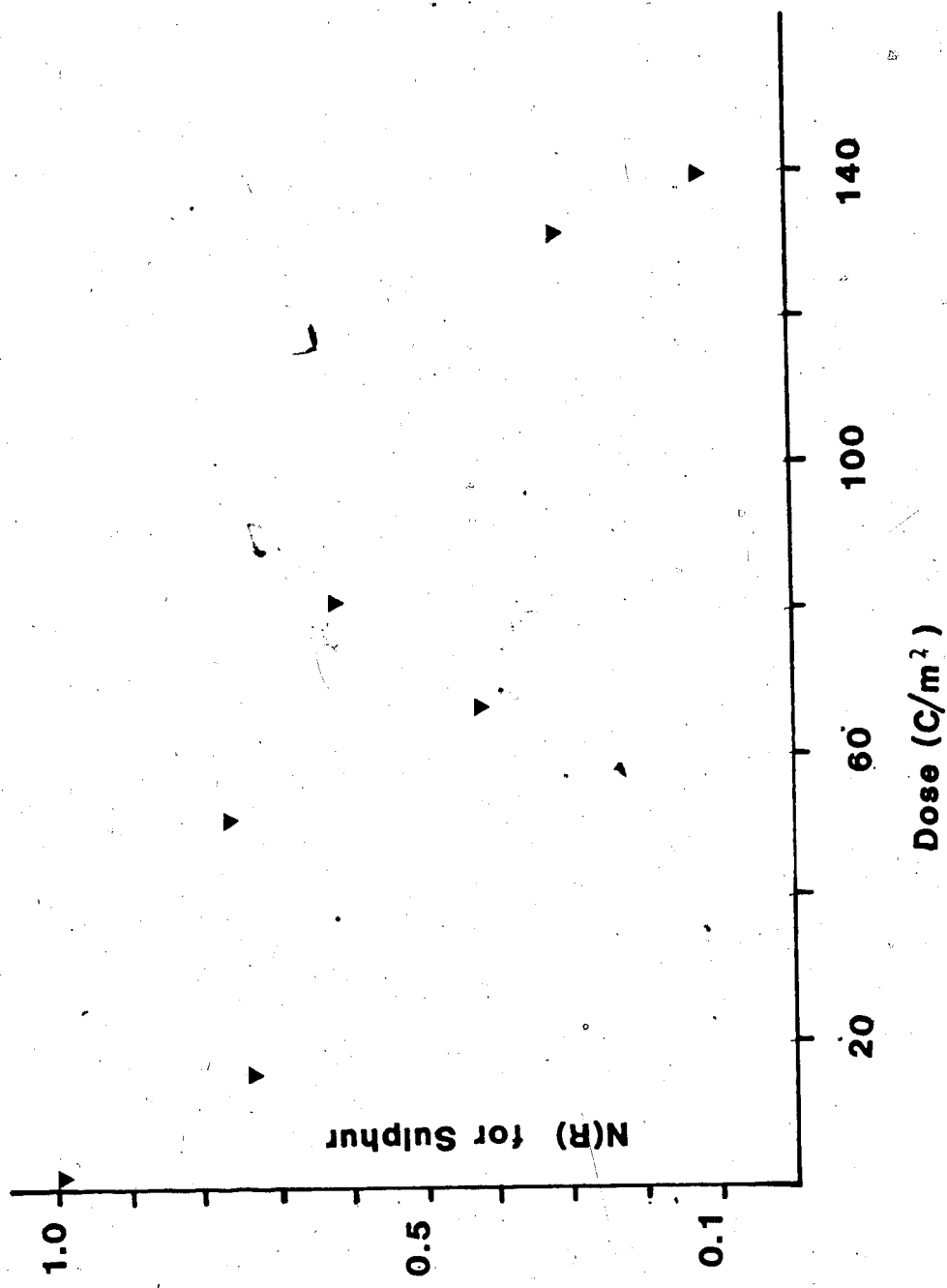


Figure 3.4 Dose Response Curve for Methionine (EELS)

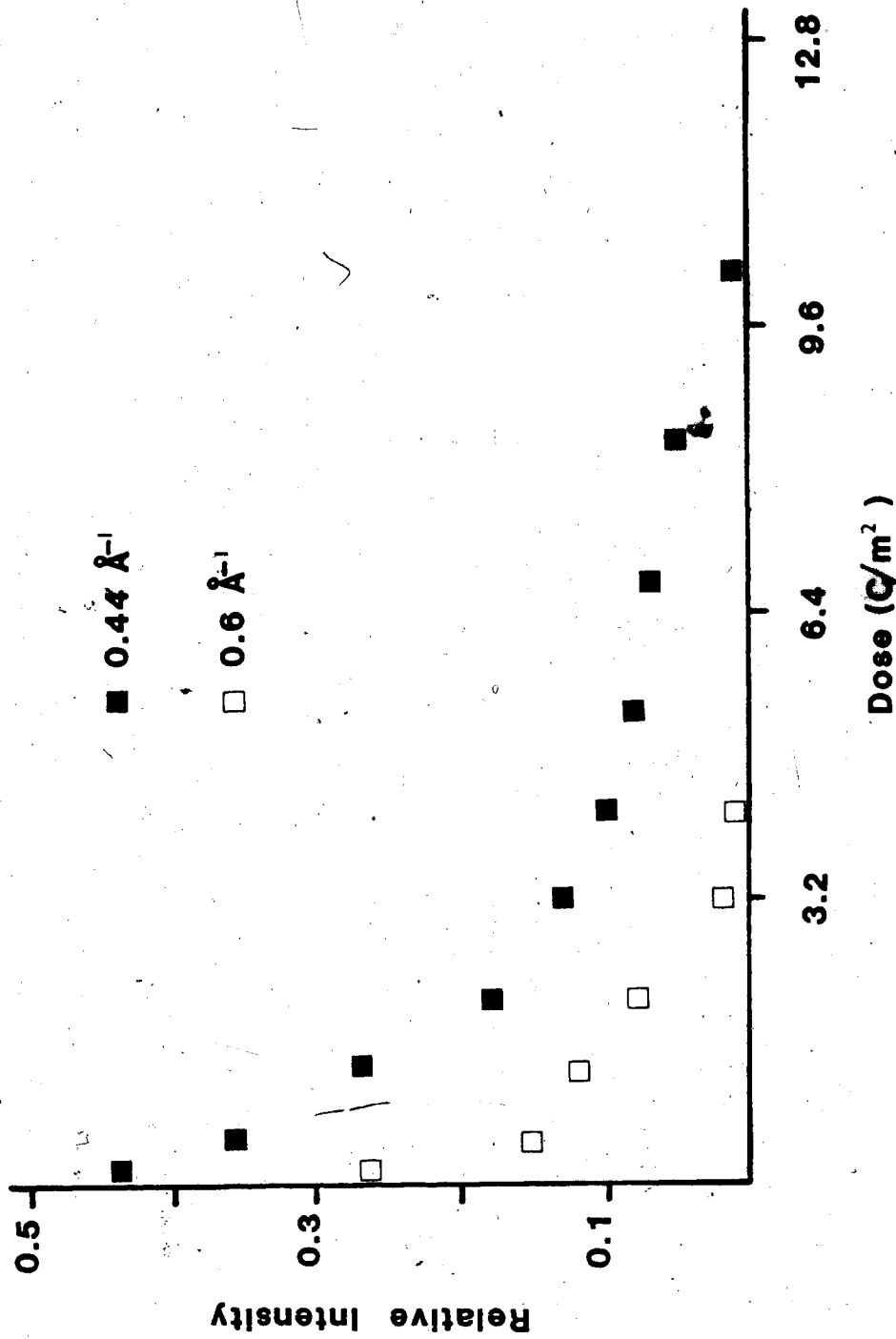


Figure 3.5 Dose Response Curve for Valine (Diffraction)

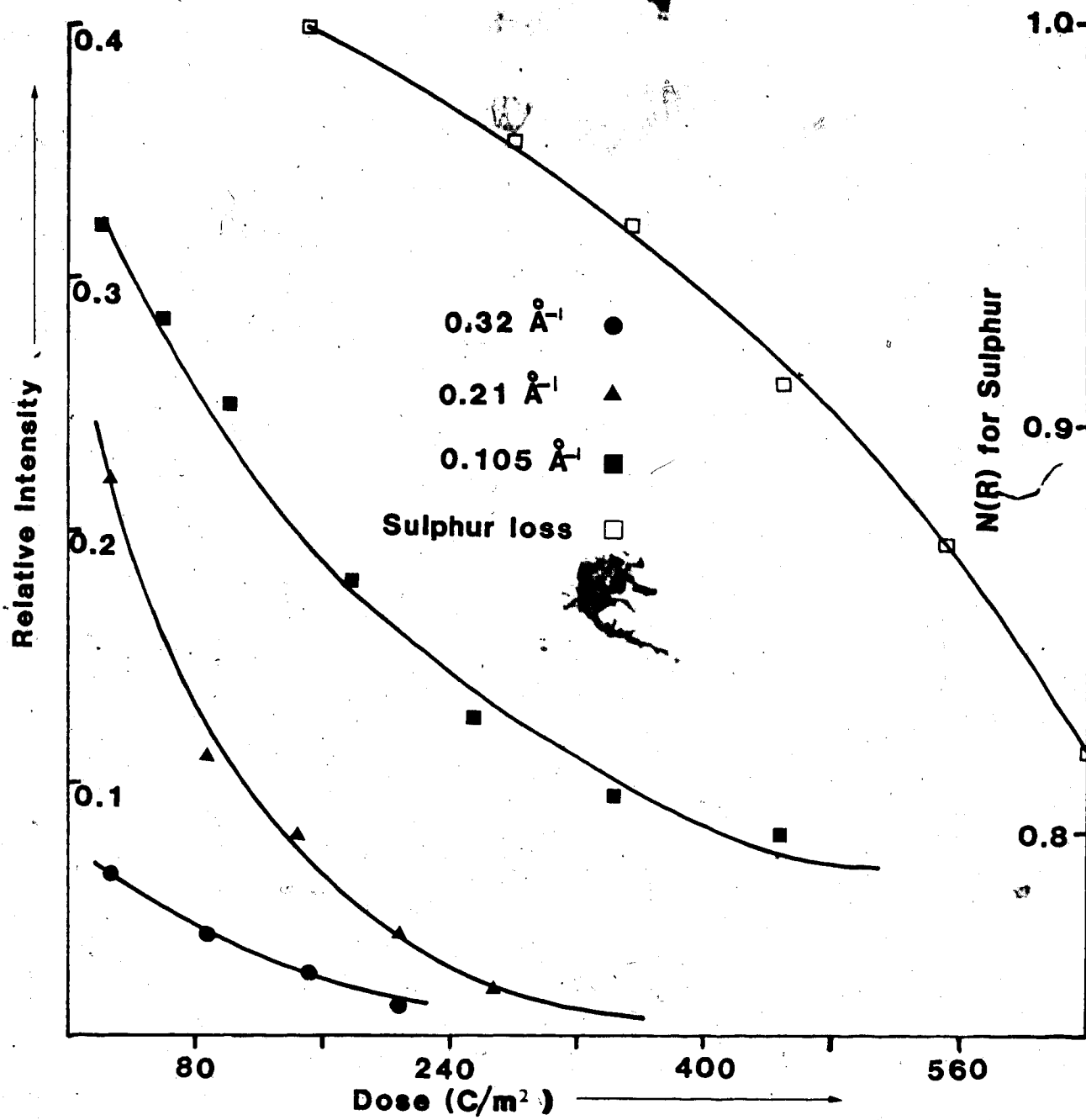


Figure 3.6 Dose Response Curve for Cysteine(Diffraction and EELS)

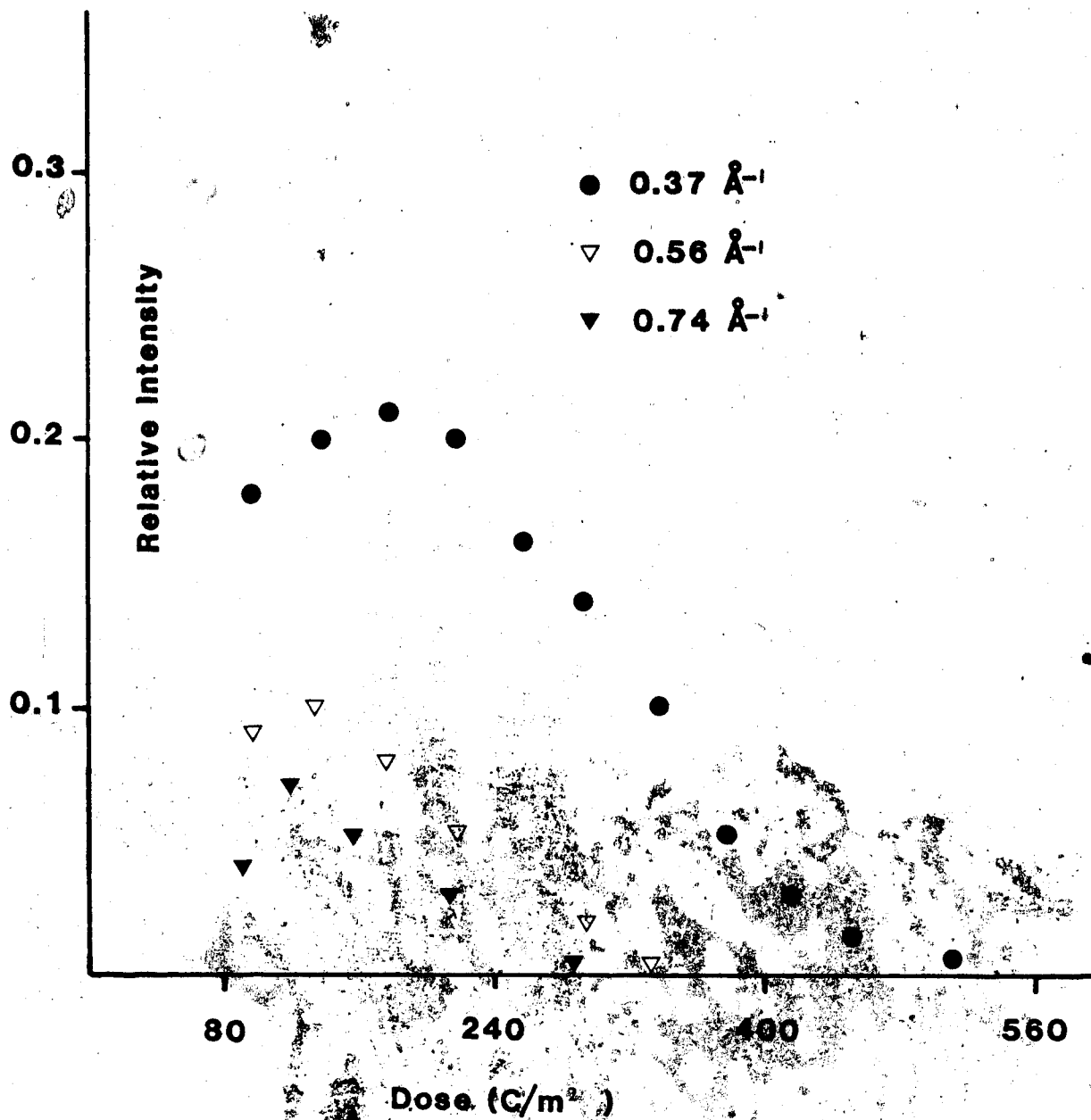


Figure 3.7 Dose Response Curve for Cystine (Diffraction)

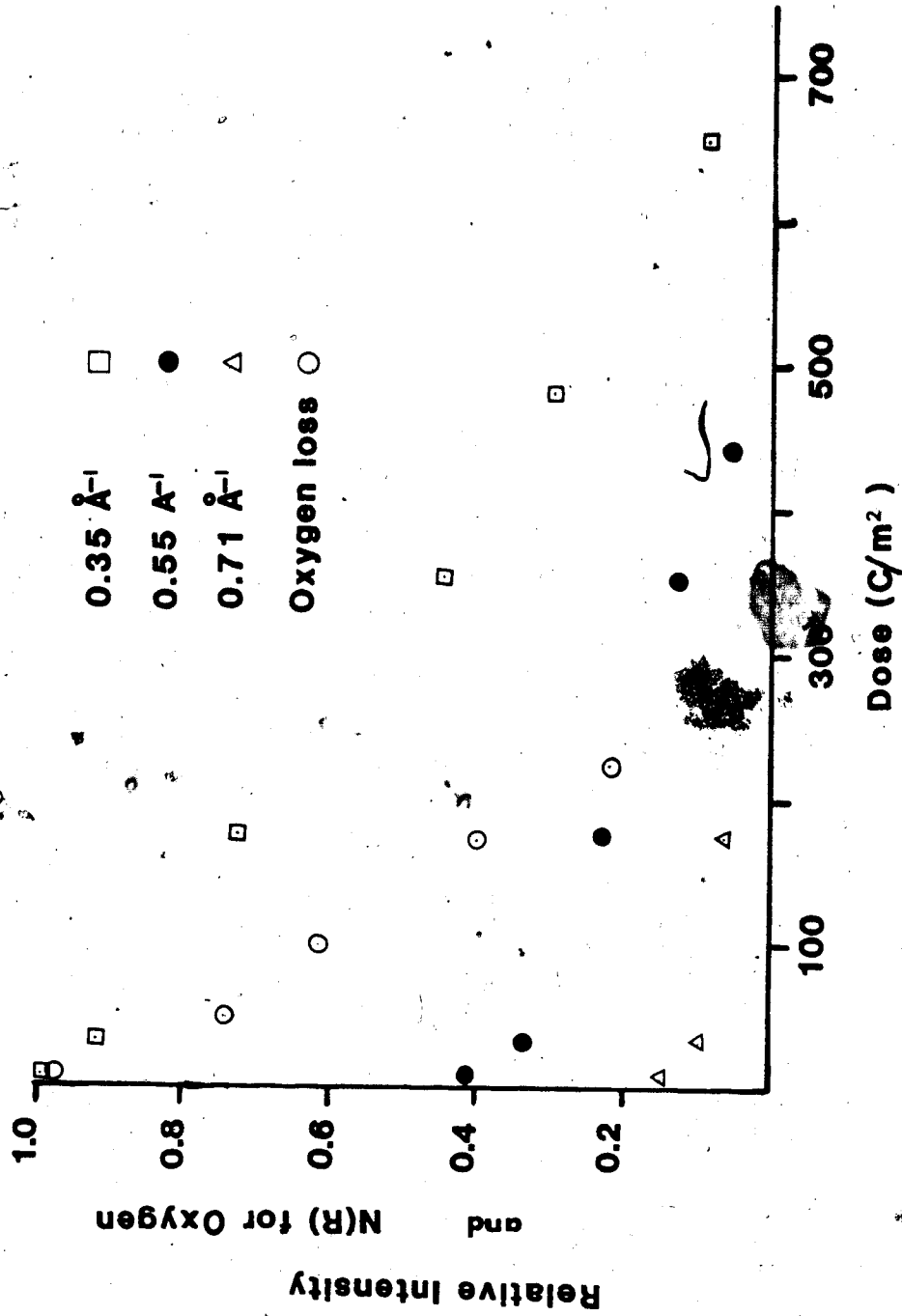


Figure 3.8 Dose Response Curve for Uracil (Diffraction and EELS)

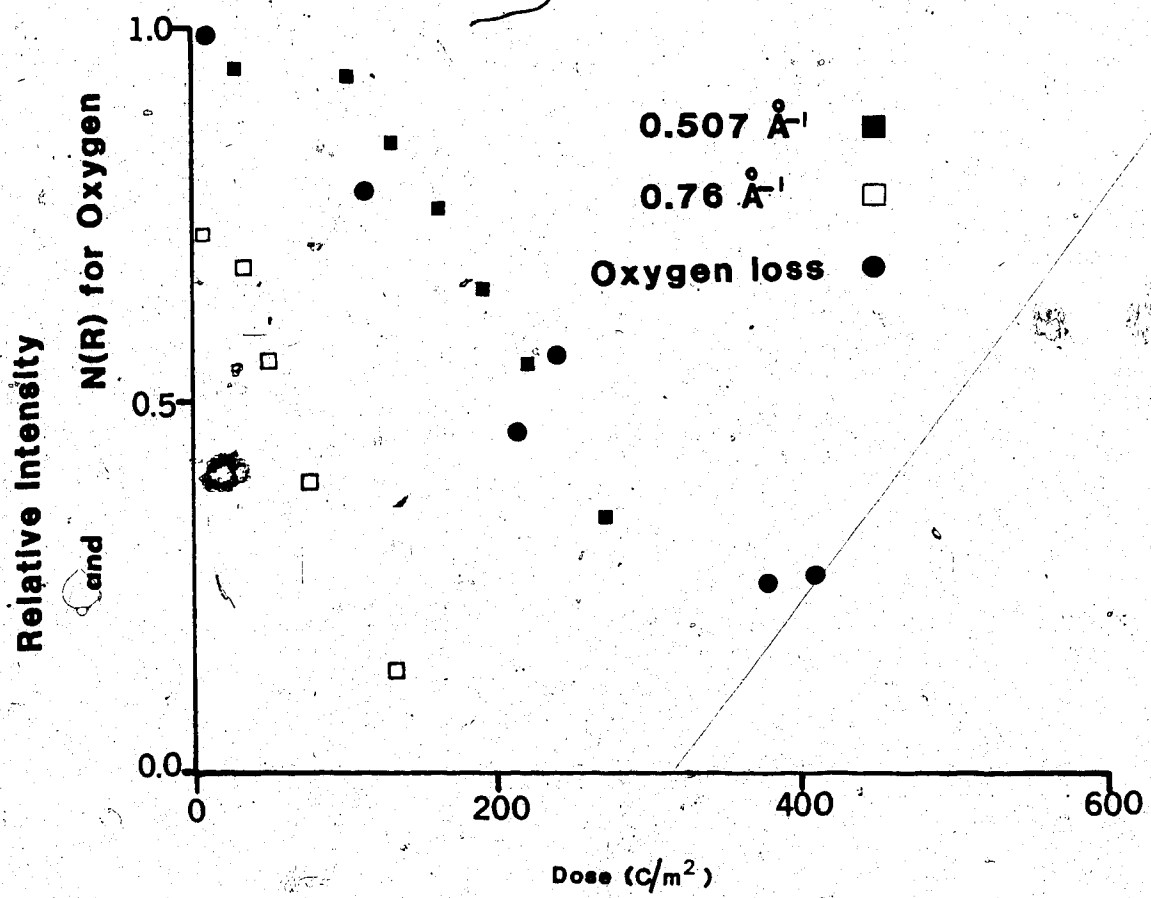


Figure 3.9 Dose Response Curve for Thymine (Diffraction and EELS)

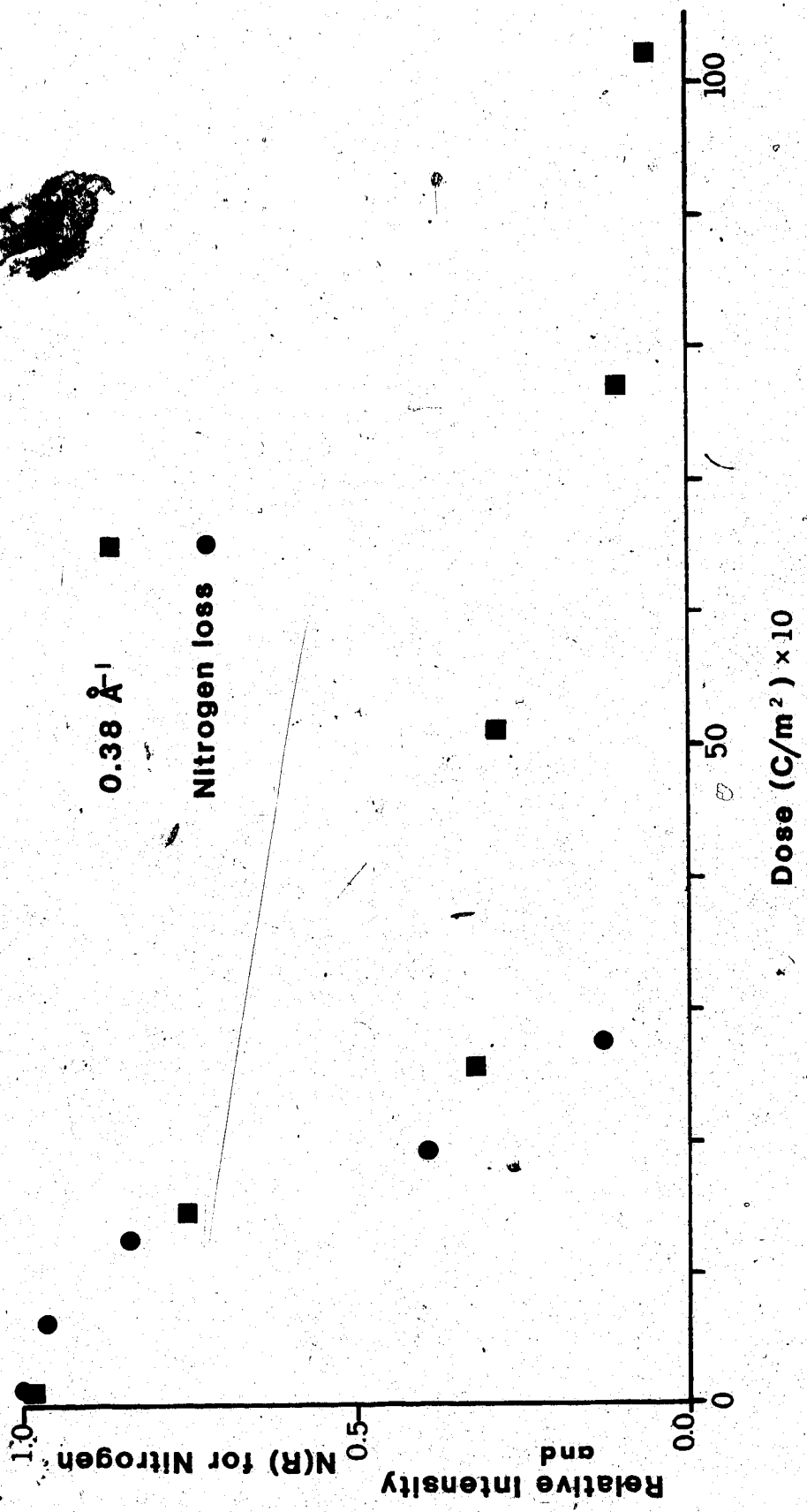


Figure 3.10 Dose Response Curve for Cytosine (Diffraction and EELS)

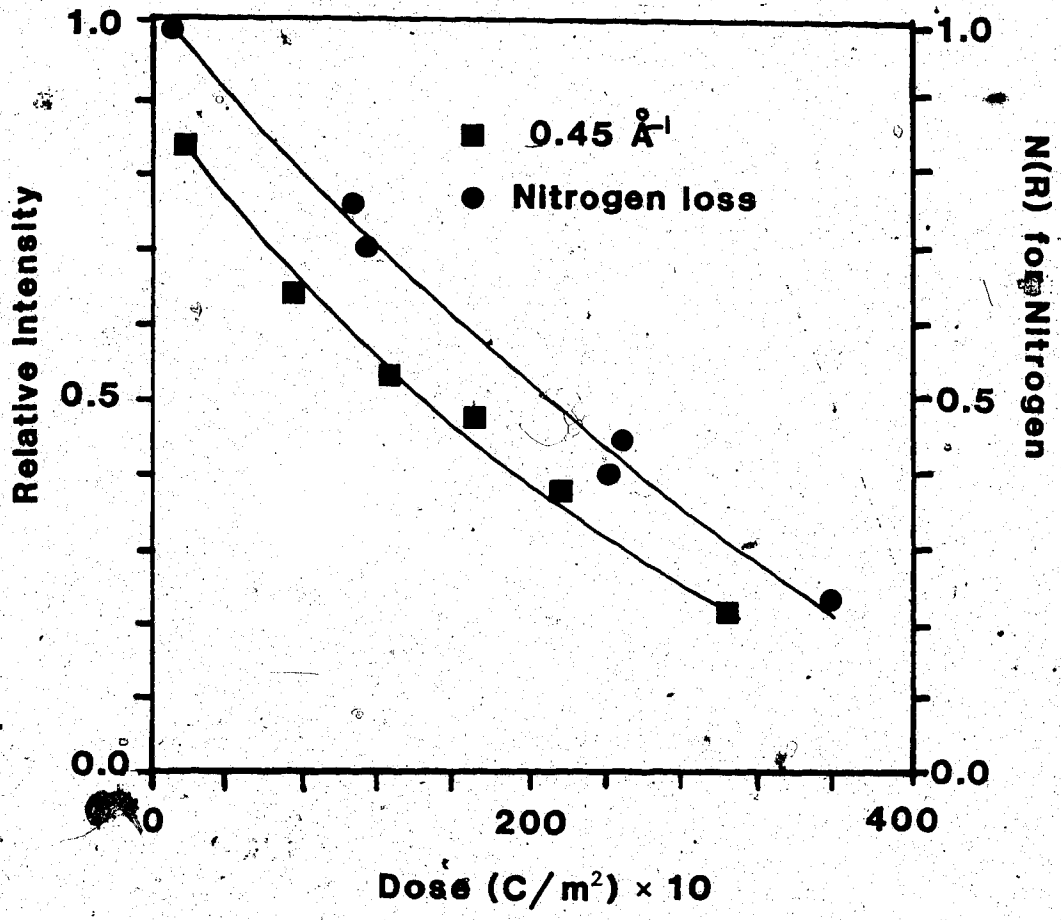


Figure 3.11 Dose Response Curve for Adenine (Diffraction and EELS)

CHAPTER IV

THE PATTERSON FUNCTION

4.1 Historical Introduction

Ever since Max von Laue, Walter Friedrich and Paul Knipping published the first X-ray diffraction photographs of copper sulphate (Laue et al., 1912) and W.H. Bragg and W.L. Bragg utilized and extended their method to other simple crystalline materials (Bragg and Bragg, 1913) and propounded the theory of X-ray diffraction by crystalline objects, the scientific community has witnessed a tremendous increase in the wealth of knowledge about the matter in the solid state. The profound impact of Laue's and Bragg's theories was evident to the early crystallographers of 1920s but any attempt to unravel the atomic arrangements within a crystal seemed to be in vain because of the complexities involved in calculations and due to lack of phase information. In a paper published in 1934, A.L. Patterson (Patterson, 1934) laid the foundation of a new theory, which, in subsequent years, catalyzed enthusiasm in X-ray crystallography, a field that was still in its infancy at that time. The details of his work were published in 1935 (Patterson, 1935) in a paper entitled 'A Direct Method for the Determination of the Components of Interatomic Distances in Crystals', wherein he described the ways Fourier Series can be manipulated for the purposes of structure determination. He utilised the concept of convolution or *faltung*, as it was then known, from the works of Debye and Menke on X-ray scattering from liquids. It was known that the desired reconstruction of the structure, from the intensities of the diffraction spots only, cannot be carried out, due to the lack of information about the phases of the diffraction spots. Since the intensities of the spots or their Fourier amplitudes depend on the nature and positions of atoms within the unit cell of a crystal hence the information about their distribution within a unit cell must be, in some way, hidden in the intensities of the spots. With this in mind, in lieu of phase information, Patterson succeeded in extracting invaluable information about the crystal structure merely from the intensities of the spots. The Fourier series

that he constructed involving the intensities of the spots as Fourier coefficients is known as the Patterson function and the following discussion succinctly describes some of the characteristics of the Patterson function first of all in terms of a mathematical formalism.

4.2 The Definition of Patterson Function

Patterson suggested, as an aid to structure determination, the use of a function $p(u,v,w)$ defined as:

$$p(u,v,w) = \frac{1}{V} \sum_h \sum_k \sum_l |F_{hkl}|^2 \exp[-2\pi i(hu+kv+lw)] \quad (4.1)$$

where u, v, w are the three spatial parameters having the same dimensions as x, y and z , which are the fractional co-ordinates of a point within the unit cell. $|F_{hkl}|^2$ is the relative intensity of a particular diffraction spot hkl , and V is the volume of the unit cell. The physical significance of this equation can be understood by expressing it in terms of the crystal potential function $\phi(x,y,z)$ (which will subsequently be referred to as the potential function).

Equation 4.1 can be rewritten as

$$p(u,v,w) = \frac{1}{V} \sum_h \sum_k \sum_l [F_{hkl} \cdot F_{hkl}^*] \exp[-2\pi i(hu+kv+lw)] \quad (4.2)$$

where F_{hkl}^* is the complex conjugate of the true structure factor F_{hkl} .

We know that the potential function, $\phi(x,y,z)$ can be expressed in terms of the structure factor in the following way:

$$\phi(x,y,z) = \frac{1}{V} \sum_h \sum_k \sum_l F_{hkl} \exp[-2\pi i(hx+ky+lz)] \quad (4.3)$$

We obtain F_{hkl} from this equation by taking its inverse Fourier transform:

$$F_{hkl} = V \int_0^1 \int_0^1 \int_0^1 \phi(x,y,z) \exp[2\pi i(hx+ky+lz)] dx dy dz \quad (4.4)$$

Also,

$$F_{hkl}^* = V \int_0^1 \int_0^1 \int_0^1 \phi(x,y,z) \exp[2\pi i(h(-x)+k(-y)+l(-z))] dx dy dz \quad (4.5)$$

which again is obtained by taking the complex conjugate equation of equation

4.4: $\phi(x,y,z)$ remains unchanged, being a real quantity.

OR,

$$F_{hkl}^* = V \int_0^1 \int_0^1 \int_0^1 \phi(x,y,z) \exp[2\pi i(h(-x)+k(-y)+l(-z))] dx dy dz \quad (4.6)$$

and if we now change the variables as:

$X=-x$, $Y=-y$ and $Z=-z$. we get

$$F_{hkl}^* = -V \int_0^{-1} \int_0^{-1} \int_0^{-1} \phi(-X,-Y,-Z) \exp[2\pi i(hX+kY+lZ)] dXdYdZ \quad (4.7)$$

Alternatively,

$$F_{hkl}^* = V \int_{-1}^0 \int_{-1}^0 \int_{-1}^0 \phi(-X,-Y,-Z) \exp[2\pi i(hX+kY+lZ)] dXdYdZ \quad (4.8)$$

We know that a unit cell repeats itself throughout a crystal and since the integration in equation 4.8 is being performed over a complete unit cell, the range of integration will not affect the result if we change it from (-1 to 0) to (0 to 1); still means an integration over a whole unit cell.

Therefore, equation 4.8 becomes:

$$F_{hkl}^* = V \int_0^1 \int_0^1 \int_0^1 \phi(-x,-y,-z) \exp[2\pi i(hx+ky+lz)] dx dy dz \quad (4.9)$$

where, the variable of integration has been rewritten in terms of x , y and z .

Comparison of equations 4.4 and 4.9 shows that F_{hkl}^* is the Fourier transform of $\phi(-x,-y,-z)$. This function differs from the potential function only with respect to the signs of the coordinates and so it represents the centrosymmetric image of the potential function.

Since in equation 4.2 $p(u,v,w)$ is the Fourier transform of the product of two functions, F_{hkl} and F_{hkl}^* , it must also be equal to the convolution of the transforms of each function. Therefore, we can write equation 4.2 as:

$$p(u,v,w) = \frac{1}{V} \left\{ \left[\sum_h \sum_k \sum_l F_{hkl} \exp[-2\pi i(hu+kv+lw)] \right]^* \right. \\ \left. \left[\sum_h \sum_k \sum_l F_{hkl} \exp[-2\pi i(hu+kv+lw)] \right] \right\} \quad (4.10)$$

From equations 4.3 and 4.9 we can write:

$$p(u,v,w) = V (\phi(x,y,z) * \phi(-x,-y,-z))$$

which says that Patterson function is proportional to a convolution between the potential function $\phi(x,y,z)$ and its centrosymmetric image $\phi(-x,-y,-z)$.

We can rewrite the last equation in vector notation; if \vec{r} represents the x, y and z co-ordinates and u, v, and w are represented by \vec{u} then this equation becomes

$$p(\vec{u}) = V[\phi(\vec{r}) * \phi(-\vec{r})] \quad (4.11)$$

Invoking the definition of a convolution function, we can write the convolution of two functions $g(\vec{r})$ and $h(\vec{r})$ as $g(\vec{r}) * h(\vec{r}) = \int_{\vec{r}} g(\vec{r}) \cdot h(\vec{u}-\vec{r}) d\vec{r}$.

Substituting $g(\vec{r}) = \phi(\vec{r})$ and $h(\vec{r}) = \phi(-\vec{r})$, equation 4.11 becomes:

$$p(\vec{u}) = V[\phi(\vec{r}) * \phi(-\vec{r})] = \int_{\text{all } \vec{r}} \phi(\vec{r}) \cdot \phi(\vec{u}+\vec{r}) d\vec{r} \quad (4.12)$$

The limit of integration 'all \vec{r} ' implies an integration over the whole unit cell. So, we can write equation 4.12 as:

$$p(\vec{u}) = V \int_{\substack{\text{unit} \\ \text{cell}}} \phi(\vec{r}) \cdot \phi(\vec{u}+\vec{r}) d\vec{r} \quad (4.13)$$

Equations 4.1 and 4.13 form the definition of the three dimensional Patterson function. Whereas, equation 4.1 is used for the calculation of the Patterson function from the relative intensity data, equation 4.13 expresses the Patterson function in terms of the potential function.

4.3 Characteristics of the Patterson Function

The following points describe various characteristics of the Patterson function:

1. There always exists a centre of symmetry in a Patterson function, even if $\phi(\vec{r})$ is non-centrosymmetric.
2. The contribution to the Patterson function from two atoms separated by a vector \vec{r} will be a rather diffuse peak centred at \vec{r} . For a crystal having many atoms within a unit cell, the Patterson function consists of various Patterson peaks

is facilitated by understanding the quantitative nature of the peaks.

The electron beam in an electron microscope column gets scattered by the specimen due to the electrostatic potential of atomic nuclei and their electron cloud. The construction of Fourier Series from electron diffraction data (with the inclusion of phases) provides a map of the potential distribution in the unit cell in which the maxima of different peaks correspond to the nuclei of different atoms. The heights of these peaks are proportional to $Z^{2/3}$ (Wainstein, 1963) where Z is the atomic number of the corresponding atom. On the other hand, in the case of the Patterson function, the formation of various peaks can be understood in the manner described below:

Figure 4.1 shows a one dimensional unit cell of length 'a' having two different atoms 1 and 2, located at fractional coordinates x_1 and x_2 respectively. The upper figure shows the distribution of potential function, $\phi(x)$, at these two atoms. The Patterson peaks corresponding to these two atoms can easily be deduced since the value of Patterson function is the product of the potential functions (or Fourier peaks) separated by a vector u (see equation 4.13), as u varies in position across the peaks. The product $\phi(x) \phi(x+u)$ will be zero for all the values of u less than u_{\min} (Figure 4.1(a)) In other words, the product will be zero as long as one end of the vector u lies in the zero region of potential function. And it will have non-zero values provided the left hand of the vector u falls within the left peak and the right hand of the vector falls within the right peak or both ends of the vector fall within one peak. As we proceed with different values of u (when both ends of the vector are falling in different peaks), integrating each time over the repeat distance of the unit cell, we encounter u_p , which is equal to the interatomic vector, $x_1 - x_2$, and it gives rise to maximum value of $p(u)$ (peak 12). As u increases to u_{\max} , the product $\phi(x) \phi(x+u)$ falls to zero and $p(u)$ decreases correspondingly. Since the interatomic vector can be in both, positive and negative, directions, it is necessary to consider the negative values of u

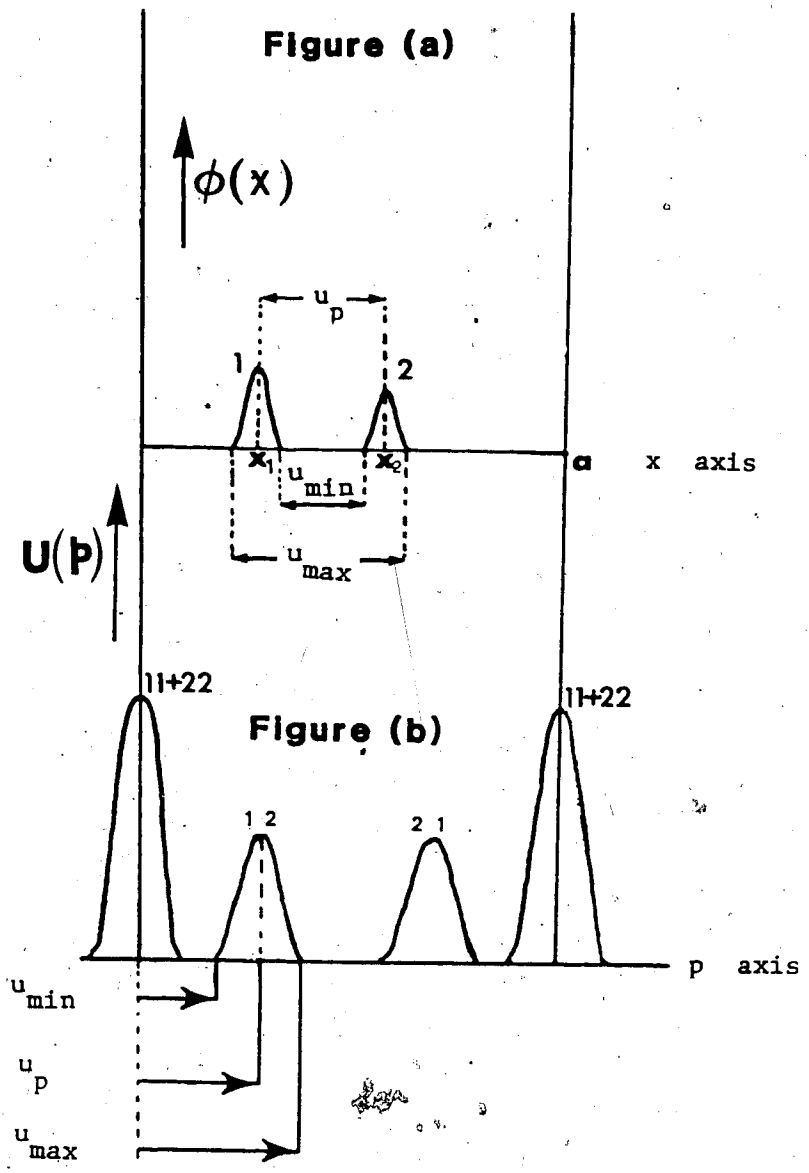


Figure 4.1 The Formation of Patterson Peaks

also. A peak $-(x_1 - x_2)$ will exist on the negative side of the origin or $(x_2 - x_1)$ will exist within the unit cell (peak 21).

On the other hand if $p(u)$ becomes large by having very small values of u such that both ends of the vector lie within each peak, and when u tends to zero, $\phi(x) \phi(x+u)$ implies the product of the maximum of each peak with itself and in this limit it gives rise to a large peak at the origin corresponding to a 'null vector' (peak 11+22). Figure 4.1(b) shows that the width of a Patterson peak is $u_{\max} - u_{\min}$ which from Figure 4.1(a) is equal to the sum of the widths of peak 1 and 2.

It is evident from this simple one-dimensional example that a Patterson map is a map of all inter-atomic vectors including the null vectors, the peaks in a Patterson map are distributed about the origin at distances equal to inter-atomic vectors and Patterson peaks are broader compared to atomic peaks.

3. For a molecule containing N atoms per unit cell, $\phi(r)$ will have a total of N peaks, while $p(u)$ will have N^2 peaks. Of these N^2 peaks, N vectors will be of zero length (null vectors) i.e. vectors from each atom to itself and will contribute a very large peak at the origin. The remaining $N(N-1)$ peaks will be distributed in the unit cell.

The distribution of peaks due to three such atoms within a unit cell is illustrated in the Figure 4.2. This shows a two-dimensional cell in which lies a molecule having three atoms (Figure 4.2(a)). Figure 4.2(b) shows the interatomic vectors between different atoms of the molecule. Since $N=3$ here, the total number of non-origin peaks will be six and the distribution of these six peaks is shown in Figure 4.2(c), in addition to a large peak at the origin. Finally, Figure 4.2(d) shows the distribution of peaks in four adjacent unit cells.

Since, the Patterson function contains a greater number of peaks within each unit cell, compared to atomic peaks obtained by Fourier synthesis, the density of Patterson peaks increases with increasing number

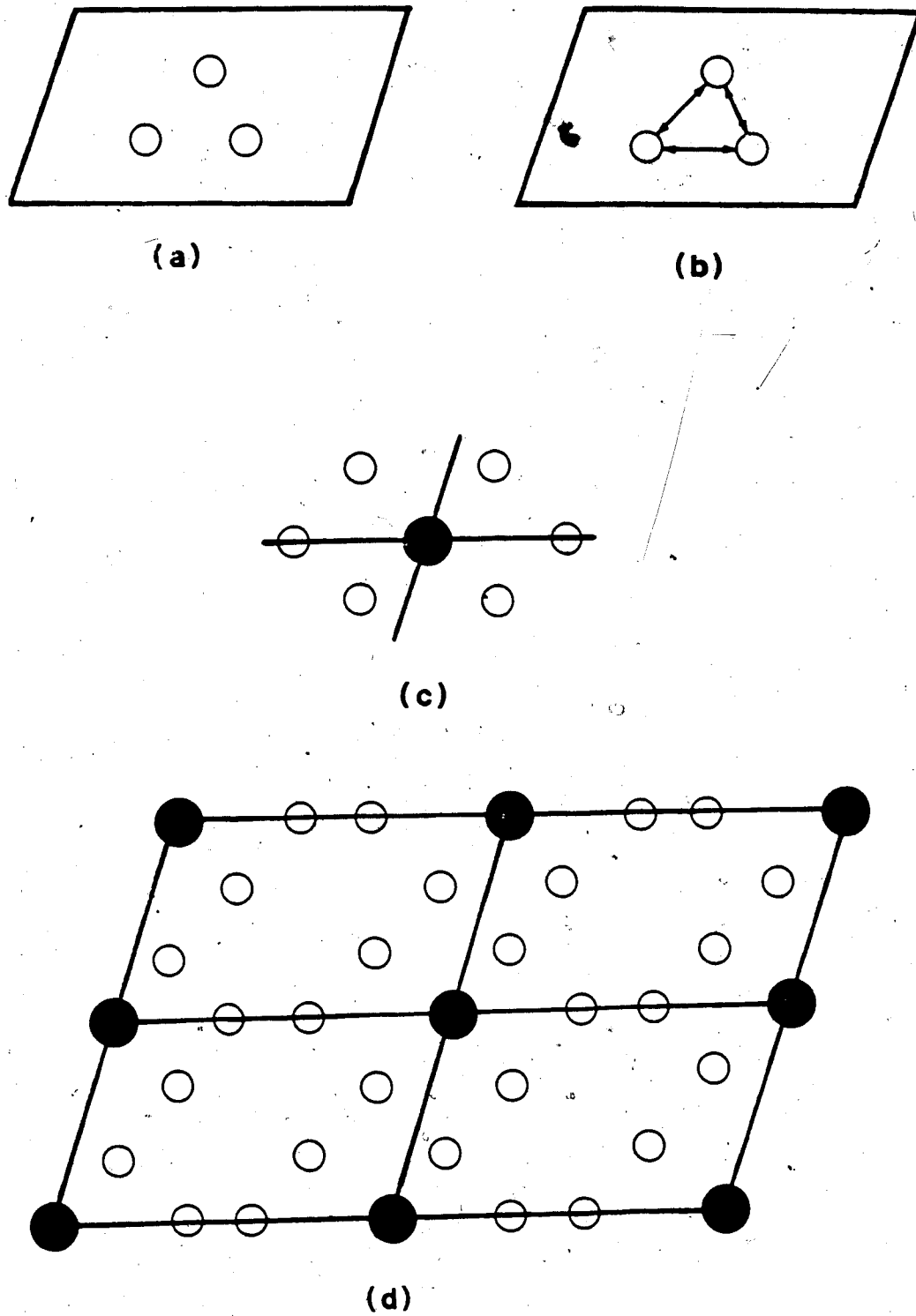


Figure 4.2 The Distribution of Patterson Peaks in a Two-dimensional Unit Cell

of atoms per unit cell (the density of Fourier peaks is, in general, independent of the number of atoms in the unit cell). This results in considerable crowding and overlapping of Patterson peaks and quite often they become indistinguishable.

4. The two-dimensional form of Patterson series can be directly written from equation 4.1 as:

$$p(u,v) = \frac{1}{S} \sum_h \sum_{k=-\infty}^{\infty} |F_{hk}|^2 \exp[-2\pi i(hu+kv)] \quad (4.14)$$

which can be further simplified as:

$$p(u,v) = \frac{1}{S} [F_{00}^2 + 2 \sum_{h=0} \sum_{k=-\infty}^{\infty} |F_{hk}|^2 \cos 2\pi(hu+kv)] \quad (4.15)$$

In practice this series is almost always calculated in relative units, that is, by disregarding the term F_{00}^2 but inclusion of this term facilitates the identification of various peaks in the manner described below:

A peak in the Patterson function exists at a distance from the origin which is equal to the interatomic vector between two atoms (say i and j) and is due to overlap of their atomic peaks. The height of a Patterson peak will accordingly be equal to $Z_i^{2/3} \cdot Z_j^{2/3}$, where Z is the atomic number (Vainshtein, 1964). The height of the origin peak, $H(0,0,0)$, (which, as seen above, is due to null vectors corresponding to the product of each atomic potential peak with itself) can be calculated using equation 4.1. By putting u, v and w equal to zero in equation 4.1 we get,

$$p(0,0,0) \propto \frac{1}{V} \sum_h \sum_k \sum_l |F_{hkl}|^2 \quad (4.16)$$

If there are N atoms in a unit cell then this equation is equal to a superposition of all the N products such as $\phi(x_i, y_i, z_i) \cdot \phi(x_i, y_i, z_i)$ at the origin and since $\phi(x_i, y_i, z_i)$ is proportional to $Z_i^{2/3}$,

$$H(0,0,0) \propto \sum_{i=1}^N Z_i^{2/3} \cdot Z_j^{2/3} = \sum_{i=1}^N (Z_i^{2/3})^2$$

$$\begin{aligned}
 \dots H_{ij} &\propto z_1^{2/3} \cdot z_j^{2/3} \\
 \dots H_{ij} &= H(0,0,0) \frac{1}{N} \frac{z_1^{2/3} z_j^{2/3}}{(\sum_{i=1}^N z_i^{2/3})^2} \quad (4.17)
 \end{aligned}$$

So, provided Patterson synthesis has been carried out by including the term F_{000}^2 , it is possible to compare the heights of various peaks by using equation 4.17 which will assist in the identification of peaks. Presence of a heavy element within the unit cell will result in a very large peak in the Patterson map as is evident, again, from equation 4.17. Such peaks between the heavy element and other elements of the unit cell will be relatively more prominent compared to the peaks due to vectors between elements of low atomic numbers.

4.4 Sharpening of Patterson Function

Consider a unit cell having N atoms and of volume V . The density of atomic peaks in such a unit cell will be N/V and the density of Patterson peaks will be N^2/V . As pointed out earlier in this chapter, the density of atomic peaks is independent of N but the density of Patterson peaks will increase linearly with N . This implies that although distinguishability of atomic peaks remains unaffected with increasing number of atoms in the unit cell, the distinguishability of Patterson peaks gets deteriorated. Moreover, Patterson peaks are broader compared to atomic or Fourier peaks (Figure 4.1) so the combined effect of the width of Patterson peaks and their increased density results in considerable overlapping of peaks. For even a moderate number of atoms ($\gg 20$) within a unit cell, this type of overlapping often results in a featureless distribution of Patterson peaks which makes their interpretation difficult.

The solution to this problem, that is enhancement of resolution, obviously cannot be carried out by decreasing the density of atomic peaks as density is the fundamental to the structure itself. But peak distinguishability can be increased by some artificial method with an overall objective of reducing the peak overlap due to broadening of peaks. This method was introduced by

Patterson himself (Patterson, 1935) and is called 'sharpening of Patterson peaks'; the following discussion describes the procedure involved.

The characteristic decline of atomic scattering factor, f_{e1} , of an atom with respect to $\sin\theta/\lambda$, is due to the distribution of electrons over a finite volume of an atom. The scattering of these electrons is in phase only in the forward direction (beam direction). For increasing departures from the forward direction, more and more destructive interference takes place between the scattering from different parts of the electron cloud. This results in rapid decline in the atomic scattering power with increasing scattering angle.

But, if all the scattering matter were concentrated at the nucleus of the atom (or at a point) then this collection of electrons would scatter in phase in all directions and f_{e1} would not decrease with increasing $\sin\theta/\lambda$. This approximation is known as point atom approximation. Since the integral of the atomic potential over its volume is proportional to $Z^{1/3}$ (Vainshtein, 1964), for such a point atom the atomic scattering factor will assume a constant value $Z^{1/3}$, for all the values of $\sin\theta/\lambda$ as is shown in figure 4.3.

Consider a crystal composed of N identical atoms per unit cell, each having Z electrons; the structure amplitude of a scattered wave will be:

$$F_{hkl} = f_{e1} \sum_{i=1}^N \exp[2\pi i(hx_i + ky_i + lz_i)] \quad (4.18)$$

Since each atom, in a real crystal, is not static at its location but is vibrating about its mean position, the amplitude of the scattered wave is affected by these vibrations. The scattering factor, f_{e1} , is then not the true scattering factor, and one must instead define a modified scattering factor as:

$$f_{e1}^T = f_{e1} \cdot f_T \quad (4.19)$$

where,

$$f_T = \exp[-B(\sin\theta/\lambda)^2] \quad (4.20)$$

In this equation B is the temperature factor, given by:

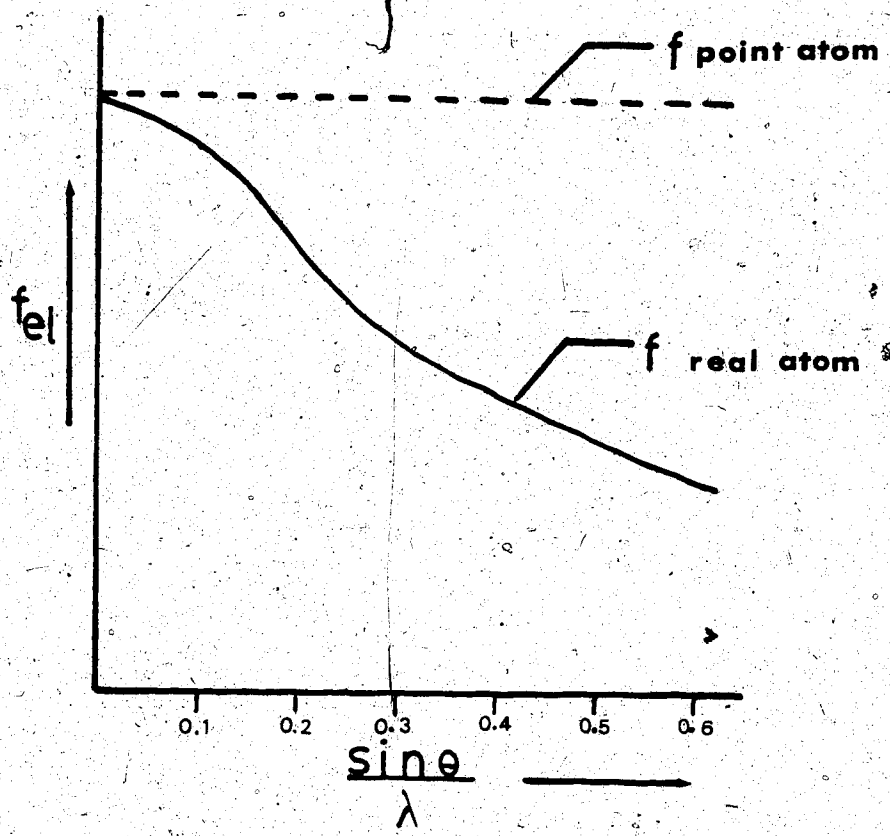


Figure 4.3 Point Atom Approximation

$$B = 8\pi^2 \overline{u^2} \quad (4.21)$$

Here, $\overline{u^2}$ is the mean square amplitude of atomic vibration of an atom in a direction normal to the reflecting plane. The net effect of such a vibration is to increase the effective volume of the atom, resulting in a greater decline of atomic scattering factor due to increasing interference between the waves scattered from the different parts of electron cloud. This becomes more noticeable with increasing B value. (See Figure 4.4).

Using f_{el}^T instead of f_{el} in equation 4.19 we get,

$$F_{hkl} = f_{el} \exp[-B(\sin\theta/\lambda)^2] \sum_{i=1}^N \exp[2\pi i(hx_i + ky_i + lz_i)] \quad (4.22)$$

Since in the case of point-atom approximation f_{el} or f_{el}^T reduces to $Z^{1/3}$, if F_{hkl}^P is the corresponding structure amplitude for point-atom approximation, we can write equation 4.22 for F_{hkl}^P as:

$$F_{hkl}^P = Z^{1/3} \sum_{i=1}^N \exp[2\pi i(hx_i + ky_i + lz_i)] \quad (4.23)$$

From equations 4.22 and 4.23 we can write,

$$F_{hkl}^P = \frac{Z^{1/3} \sum_{i=1}^N \exp[2\pi i(hx_i + ky_i + lz_i)]}{f_{el} \exp[-B(\sin\theta/\lambda)^2] \sum_{i=1}^N \exp[2\pi i(hx_i + ky_i + lz_i)]} F_{hkl}$$

or,

$$|F_{hkl}^P|^2 = (Z^{1/3}/f_{el})^2 \exp[2B(\sin\theta/\lambda)^2] |F_{hkl}|^2 \quad (4.24)$$

Equation 4.24 gives the sharpened values of intensities for various diffraction spots. This equation is only applicable to the case of a crystal having only one type of atom. Most crystals contain more than one kind of atom, and although it is not possible to obtain exact sharpening in this case, the following equation can be used (Buerger, 1959 and Stout and Jensen, 1968)

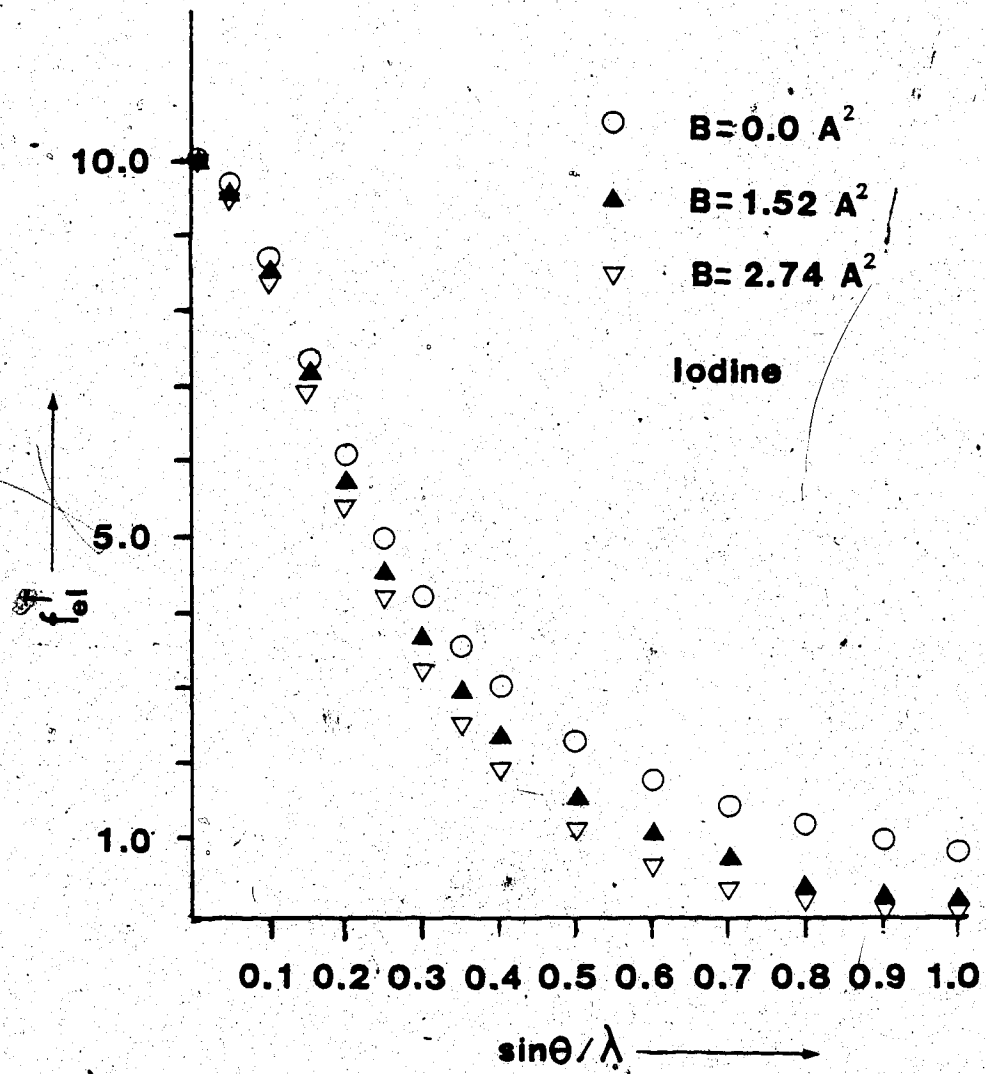


Figure 4.4 Dependence on B of Atomic Scattering Factor

$$F_{hkl}^P = \frac{\sum_{i=1}^N Z_i^{1/3}}{\exp[-B(\sin\theta/\lambda)^2] \sum_{i=1}^N f_{el_i}} F_{hkl}$$

or,

$$|F_{hkl}^P|^2 = \left[\frac{\sum_{i=1}^N Z_i^{1/3}}{\sum_{i=1}^N f_{el_i}} \right]^2 \exp[2B(\sin\theta/\lambda)^2] |F_{hkl}|^2 \quad (4.25)$$

where B is the overall isotropic temperature factor assumed to be same for all the atoms within a unit cell. Equation 4.25 gives the sharpened values of the intensities of various diffraction spots, which when used in equation 4.1 will give rise to a sharpened Patterson function. The only unknown quantity in this equation is B, which can be evaluated following the method of A.J.C. Wilson, in the following way.

4.4.1 Calculation of B By the Method of Wilson

An elegant statistical method for the scaling of observed intensity data and for the calculation of the B factor was proposed in 1942 by A.J.C. Wilson (Wilson, 1942) and is now routinely employed by X-ray crystallographers for preliminary analysis of their data.

Consider a unit cell having N randomly distributed atoms. The structure factor for a particular reflection spot, hkl, is given by

$$F_{hkl} = V \int_0^1 \int_0^1 \int_0^1 \phi(x,y,z) \exp[2\pi i(hx+ky+lz)] dx dy dz$$

We can rewrite equation 4.4 in the vector notation as.

$$F_{hkl} = \int_{vol} \Phi(\vec{r}) \exp[2\pi i(\vec{H} \cdot \vec{r})] d\vec{r} \quad (4.26)$$

where, $\vec{r} = x\vec{a} + y\vec{b} + z\vec{c}$ and $\vec{H} = h\vec{a}^* + k\vec{b}^* + l\vec{c}^*$. Here, a, b, c and a^* , b^* , c^* are three vectors defining real lattice and reciprocal lattice, respectively.

If we replace $\phi(\vec{r})$, the potential function, by the superposition of atomic potentials, given by:

$$\phi(\vec{r}) = \sum_{i=1}^N \phi_i(\vec{r} - \vec{r}_i) \quad (4.27)$$

we get

$$F_{hkl} = \int_V \sum_{i=1}^N \phi_i(\vec{r}-\vec{r}_i) \exp[2\pi i(\vec{H}\cdot\vec{r}_i)] d\vec{r} \quad (4.28)$$

$$= \sum_{i=1}^N \left\{ \int_V \phi_i(\vec{r}-\vec{r}_i) \exp[2\pi i(\vec{r}-\vec{r}_i)\cdot\vec{H}] d\vec{r} \right\} \exp[2\pi i(\vec{H}\cdot\vec{r}_i)]$$

$$= \sum_{i=1}^N f_{el_i} \exp[2\pi i(\vec{r}_i\cdot\vec{H})]$$

or

$$F_{hkl} = \sum_{i=1}^N f_{el_i} \exp[2\pi i(hx_i + ky_i + lz_i)] \quad (4.29)$$

The intensity of a reflection spot will be equal to $F_{hkl} F_{hkl}^*$, therefore:

$$I_{hkl} = F_{hkl} \cdot F_{hkl}^*$$

$$= \sum_{i,j=1}^N f_{el_i} f_{el_j} \exp[2\pi i\{h(x_i - x_j) + k(y_i - y_j) + l(z_i - z_j)\}]$$

$$= \sum_{i=1}^N f_{el_i}^2 + \sum_{\substack{i,j=1 \\ i \neq j}}^N f_{el_i} f_{el_j} \exp[2\pi i\{h(x_i - x_j) + k(y_i - y_j) + l(z_i - z_j)\}] \quad (4.30)$$

If we now average or sum this equation for all values of h, k, l , the second term on the right hand side will be practically equal to zero, as it will take both positive and negative values.

Therefore, equation 4.30 will reduce to,

$$\langle F_{hkl} \cdot F_{hkl}^* \rangle = \sum_{i=1}^N f_{el_i}^2 \quad (4.31)$$

where, $\langle F_{hkl} \cdot F_{hkl}^* \rangle$ denotes the average value of $F_{hkl} \cdot F_{hkl}^*$ over a small range of $\sin^2 \theta / \lambda^2$ such that f_{el_i} is not varying rapidly within any given range.

The observed value of intensity of a diffraction spot, $|F_{hkl}|^2$, is on an arbitrary scale; if k is the scale factor necessary for converting it to absolute scale, then:

$$\langle |F_{hkl}|^2 \rangle = k \langle |F_{hkl}^{\text{absolute}}|^2 \rangle \quad (4.32)$$

and

$$|F_{hkl}^2| = k |F_{hkl}^{\text{absolute}}|^2 \quad (4.33)$$

or, from equation 4.31:

$$\langle |F_{hkl}|^2 \rangle = k \sum_{i=1}^N f_{e1_i}^2 \quad (4.34)$$

Again, since the atoms are not static but are vibrating about their mean position so from equations 4.19 and 4.20 we can write:

$$f_{e1_i}^2 = f_{e1_i}^2 \exp[-2B(\sin\theta/\lambda)^2] \quad (4.35)$$

we assume B to be isotropic and the same for all the atoms within the unit cell, we can write equation 4.34 as:

$$\langle |F_{hkl}|^2 \rangle = k \exp[-2B(\sin\theta/\lambda)^2] \sum_{i=1}^N f_{e1_i}^2 \quad (4.36)$$

or

$$\frac{\langle |F_{hkl}|^2 \rangle}{\sum_{i=1}^N f_{e1_i}^2} = k \exp[-2B(\sin\theta/\lambda)^2]$$

or

$$\ln \frac{\langle |F_{hkl}|^2 \rangle}{\sum_{i=1}^N f_{e1_i}^2} = \ln k - 2B(\sin\theta/\lambda)^2 \quad (4.37)$$

If we put $\{g\} = \frac{\langle |F_{hkl}|^2 \rangle}{\sum_{i=1}^N f_{e1_i}^2}$ in equation 4.37, we get

$$\ln \{g\} = \ln k - 2B(\sin\theta/\lambda)^2 \quad (4.38)$$

This equation corresponds to the equation of a straight line and if we plot a graph of $\ln\{g\}$ against $(\sin\theta/\lambda)^2$, then the slope of the best line

drawn through different points will be equal to $-2B$ and the intercept on the ordinate will be equal to $\ln(k)$. The graph so obtained is called a Wilson plot. Figure 4.5 shows a typical example of the Wilson plot and it can be drawn in the following way:

1. The reciprocal lattice is divided into different zones of equal $\frac{\sin^2 \theta}{\lambda^2}$ or the zones are plotted such that their range or width decreases with increasing $\sin \theta / \lambda$ values.
2. The values of observed intensities are plotted on the 'zoned' reciprocal lattice.
3. The average of $|F_{hkl}|^2$, i.e. $\langle |F_{hkl}|^2 \rangle$ is calculated for each zone. While calculating the average, points of zero intensity and forbidden reflections are counted by assigning them zero intensity. The intensity of the central spot or $|F_{000}|^2$ is not included in the calculations. If symmetry elements permit the use of a fraction of reciprocal lattice then the points lying at the border are assigned half of their actual values of intensity.
4. $\sum_{i=1}^N f_{e_i}^2$ is calculated for each zone; f_{e_i} values for various elements can be taken from the published data (Vainshtein, 1964) corresponding to the mid-value of $\sin \theta / \lambda$ for that particular zone.
5. Knowing $\langle |F_{hkl}|^2 \rangle$ and $\sum_{i=1}^N f_{e_i}^2$ for each zone, it is trivial to calculate the value of $\ln\{g\}$ for each zone.
6. The Wilson plot can now be drawn between $\ln\{g\}$ and $\frac{\sin^2 \theta}{\lambda^2}$, the slope of which will give $2B$ and the intercept on the ordinate used to get the scale factor k .

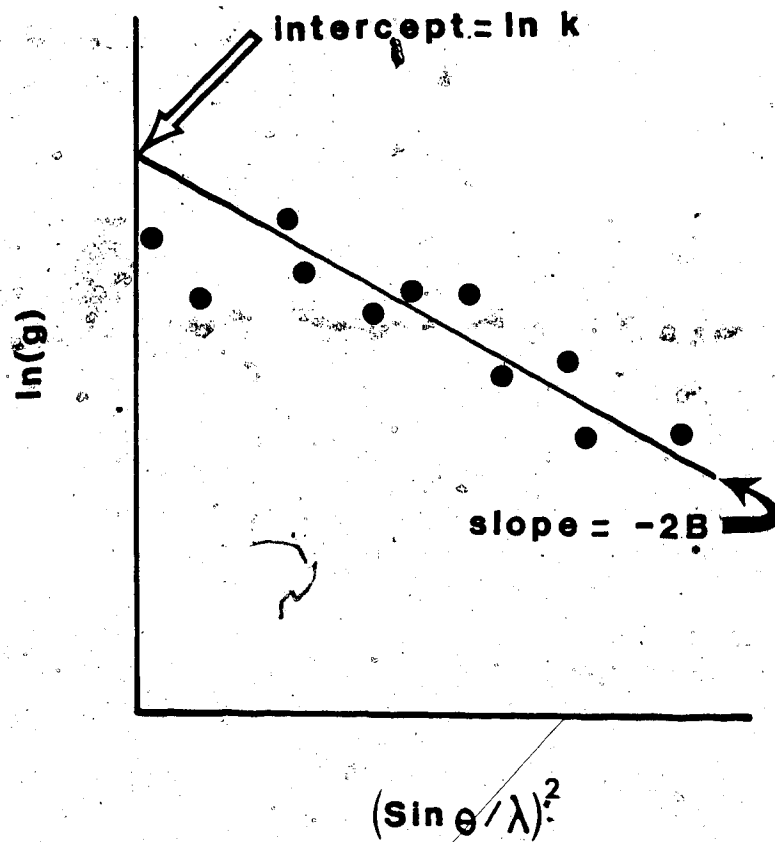


Figure 4.5 Wilson Plot

CHAPTER V

APPLICATION OF PATTERSON FUNCTION IN THE RADIATION DAMAGE

STUDIES OF 5-IODOURACIL

5.1 Introduction

An immediate sequel to the discussion pertaining to the Patterson function in the previous chapter is the application of this function to radiation damage studies. Prior to experiments leading to structure determination of biological molecules by electron microscopy, it is essential to assess the sensitivity of a particular compound to electron irradiation. Some information about the structural and chemical changes to the compound can indeed be extracted by observing changes in the electron diffraction pattern and EEL spectra, as discussed in Chapter 3. But to gain a deeper insight into the process of radiation damage it seems necessary to employ different methods of analysis. One such method would be to reconstruct an image of the damaged and undamaged structures at different doses of irradiation. The obvious unknowns involved in reconstructing images at different doses of irradiation are the phases of diffraction spots. However, Clark et al. in 1979 (Clark, 1979) conducted such a radiation damage study on α -copper phthalocyanine. Similarity in the structures between α -copper phthalocyanine and platinum phthalocyanine enabled them to take the phases from the X-ray data of the latter. The centrosymmetric structure of α -copper phthalocyanine molecules led them to conclude that the phases of the diffraction spots do not change upon irradiation. For centrosymmetric cases, phases can assume only two values: 0 and π ; whereas for non-centrosymmetric cases the phases can assume any value in between these two limits. So the basic assumption of using the same phases at different doses of irradiation may not be valid for non-centrosymmetric cases. In other words, it may not be possible to recover the structure of damaged crystals upon electron irradiation by that method, for non-centrosymmetric structures.

One of the aims of radiation damage studies is to determine a safe dose which can be used for structure determination of biological molecules.

Since, it is not possible to assume, *a priori*, the phases of various diffraction spots of unknown structures, the recovery of electrostatic crystal potential from the diffraction data is not feasible for radiation damage studies. An alternative method would be to construct a Patterson function for undamaged and damaged structures. Differences in successive Patterson maps should provide information about the changes in the crystal structure upon irradiation. Phase information is not needed for constructing Patterson maps, so this method of studying radiation damage should be equally applicable to both centrosymmetric and non-centrosymmetric structures. A disadvantage associated with this method stems from the fact that the exclusion of phases makes an analysis based on the changes in Patterson maps less informative compared to Fourier methods, since Patterson maps correspond to a distribution of interatomic vectors and not to the distribution of atoms as such within a unit cell. In case of large molecules (having greater than 20-30 atoms) the identification of peaks in a Patterson map becomes increasingly difficult; however, any change in the Patterson map should correspond to the maximum dose which can be used for structural investigations.

5.2 Experimental Details

The compound 5-iodouracil was obtained from Sigma Chemical Company and it was used without any further purification. The crystals of 5-iodouracil were prepared by slow evaporation of a small drop of aqueous solution on a carbon coated copper grid. The grids were subsequently examined in the JEM 100B electron microscope for the preliminary analysis of the crystals, primarily for estimating crystal thickness. Crystal thickness was determined by EELS as described in Chapter 2. By varying the concentration of the aqueous solution, the proper concentration was determined which gave rise to suitably thin crystals. Crystals of about 120 Å thickness were selected for electron diffraction studies.

A JEM 100 B electron microscope, fitted with a liquid nitrogen anti-contamination device and a goniometer stage, was used at 80keV

accelerating voltage, for conducting electron diffraction experiments on 5-iodouracil at room temperature.

Since the recorded optical density on a photographic plate is proportional to exposure for only a part of the whole range of possible values of exposure (Agar, Alderson and Chescoe, 1980), it is essential for any diffraction study to determine the optimum exposure necessary for recording a diffraction pattern. This was achieved by a preliminary recording of diffraction patterns, at a fixed beam current but at different exposure times. An optical density wedge supplied by Kodak, for calibration purposes, was used to determine the necessary exposure time by comparing the densitometer traces of the spots with that of the step wedge. The exposure time which corresponded to the linear region of the optical density versus exposure graph was chosen for the subsequent recordings of diffraction patterns.

A series of selected-area electron-diffraction patterns was recorded from the same area of the specimen, at a constant beam current but with increasing dose to the specimen. The goniometer stage was used to align the electron beam parallel to one of the crystallographic axes, in order to obtain a symmetrical diffraction pattern. For the purpose of indexing the diffraction pattern of 5-iodouracil, a diffraction pattern of gold was recorded under the identical electron-optical conditions.

A total of twenty series of electron diffraction patterns were recorded, the most symmetric sets of diffraction patterns being selected for further analysis. The dose sustained by the irradiated area of the specimen was determined by measuring the transmitted beam current at screen level, using a Faraday cup. Diffraction patterns were recorded with a defocused Condenser 2 lens, resulting in a large spot at the specimen. Spot size at the specimen was kept large in order to have a uniform current density as well as to reduce current density, which is desirable for radiation damage measurements. The beam diameter was measured from the image of the beam spot recorded at a calibrated magnification of 10,000.

The diffraction patterns were recorded on Kodak Electron Image plates. All the plates corresponding to a particular series of diffraction patterns were developed simultaneously in Kodak D-19 developer, diluted to half of its original concentration, for four minutes with continuous agitation. The temperature of the developer was kept at 20°C. All the developed plates were subsequently rinsed in distilled water and then transferred to Kodak rapid fixer for a fixing time of four minutes.

Densitometer traces of all the diffraction patterns were obtained on a Joyce-Loebl automatic recording microdensitometer MK III CS. Background subtraction was carried out by drawing a background curve as shown in Figure 5.1. The area under a peak on the densitometer trace and above the background was calculated using the integrating unit of MOP-3, which (corresponding to the intensity of each spot in the pattern) yielded a quantity proportional to the square of the corresponding Fourier component of the potential.

5.2.1 Calculation of Electron Dose

For the calculation of electron dose the beam current was measured using the Faraday cup, which was found to be equal to 3.6×10^{-11} A. Spot size at the screen level was found to be 75mm at a magnification of 10,000. Equation 3.12 was used to calculate the dose rate and the cumulative dose sustained by the specimen was determined by multiplying the dose rate obtained from equation 3.12 with the total time spent between the recording of each diffraction pattern. Since the exposure time necessary for the recording of a diffraction pattern (4 s) is small compared to the total irradiation time, it can safely be excluded in calculating cumulative doses.

5.2.2 Indexing of Diffraction Patterns

The following standard formula is used for the indexing of diffraction spots (see Chapter 3 also) (Beeston et al., 1972).

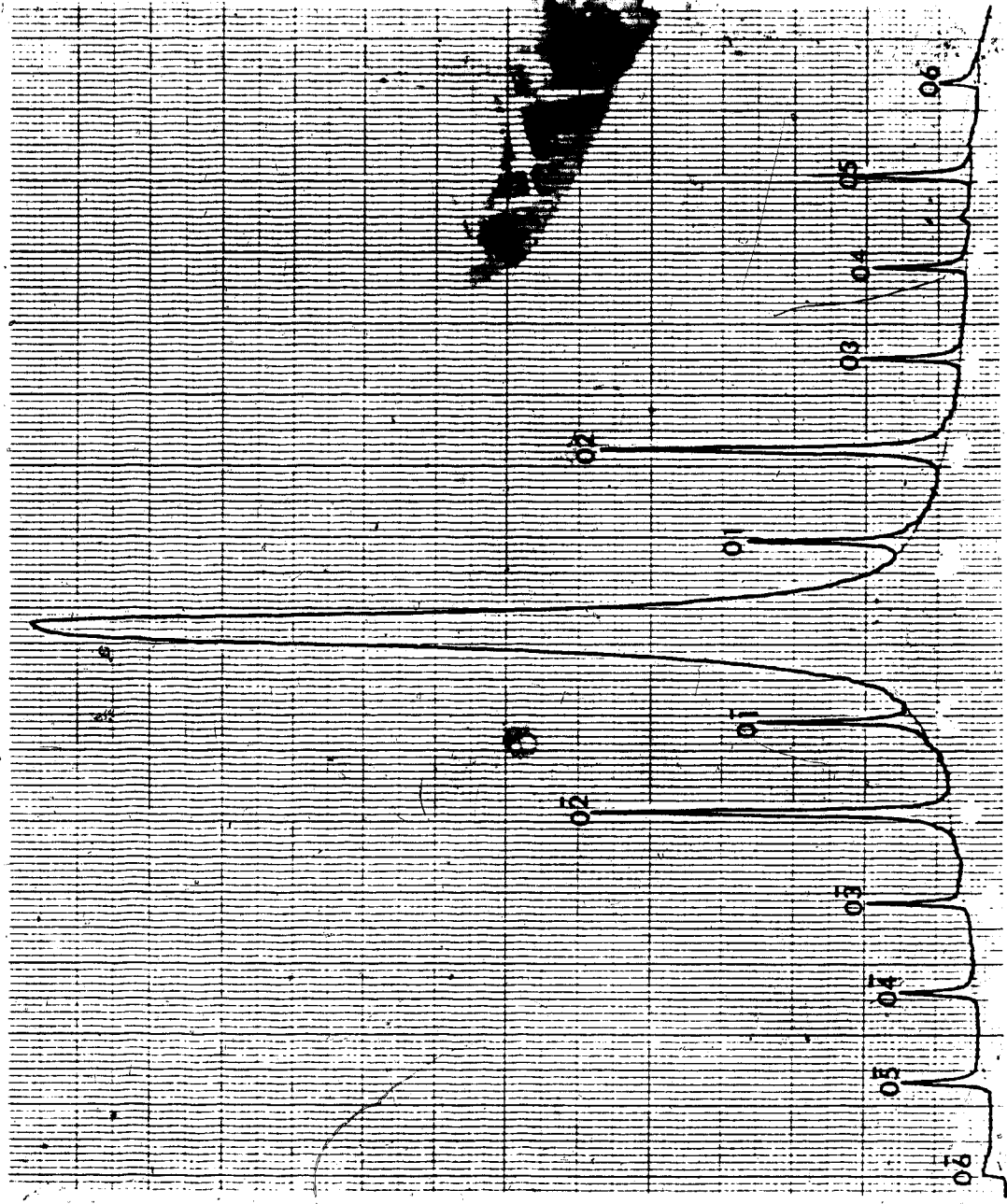


Figure 5.1 Densitometer Trace of a Single Layer-line and Background Fit

from the Diffraction Pattern of 5-Iodouracil

$$R d = L \lambda \quad (5.1)$$

where R is the distance of a particular spot from the central spot of the diffraction pattern, L is the camera length, λ is the wavelength of electrons at a particular accelerating voltage and d is the lattice spacing of the planes corresponding to that particular diffraction spot. So, knowing the values of R , L and λ one can calculate d for any diffraction spot belonging to the diffraction pattern. The diffraction patterns were recorded at an accelerating voltage of 80 keV, so the wavelength of electrons will (from standard tables) be 0.0418 Å. The only unknown in equation 5.1 is L , the camera length, which can be calculated from the diffraction pattern of any standard specimen of known lattice spacings. Gold was used as a standard in the present study. It crystallizes in cubic crystals and since $a = 4.07$ Å for gold, the lattice spacing of any ring in the diffraction pattern of gold can be obtained using equation 5.2:

$$d_{hkl} = \frac{a}{\sqrt{h^2 + k^2 + l^2}} \quad (5.2)$$

Therefore,

$$d_{111} = \frac{4.07}{\sqrt{1^2 + 1^2 + 1^2}} = 2.3498 \text{ Å}$$

The diameter ($2R$) of 111 ring in the diffraction pattern of gold was found to be equal to 10.9 mm, so we can calculate camera length from equation 5.1:

$$L = \frac{2Rd}{2\lambda} = \frac{10.9 \times 2.3498}{2 \times 0.0418} = 308.0 \text{ mm}$$

The diffraction pattern of 5-iodouracil is shown in Plate 5.1; it can now be indexed since the camera length is known. The diffraction pattern of 5-iodouracil forms a rectangular grid of regularly arranged diffraction spots and extends to the sixth order of reflection in one direction and to fifth order in the direction perpendicular to the previous one. The indexing of the whole diffraction pattern can be achieved by indexing the two innermost spots (which lie at 90° to one another) as other spots can be indexed once the indices of these innermost spots are known. Figure 5.2 shows the positions of two such

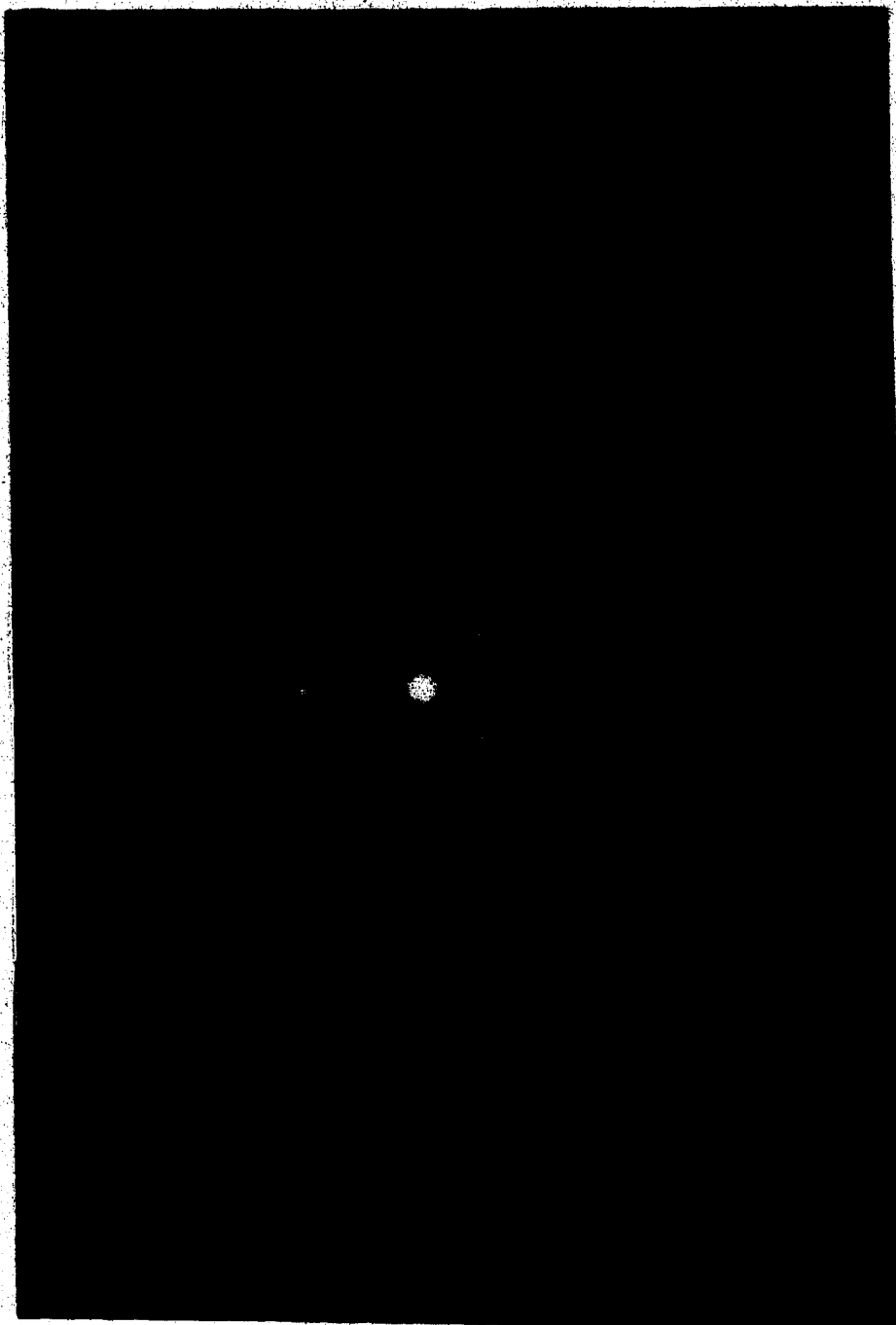


Plate 5.1 Diffraction Pattern of 5-Iodouracil

spots, A and A', on either side of the central spot.

The distance between spots A and A' (2R) was measured from the recorded diffraction pattern and was found to be equal to 5.79mm, therefore, from equation 5.1 we can write:

$$d_A = \frac{2L\lambda}{2R} = \frac{2 \times 308.0 \times 0.0418}{5.79} = 4.44 \text{ \AA}$$

Similarly, since $BB' = 5.28 \text{ mm}$,

$$d_B = \frac{2L\lambda}{2R} = \frac{2 \times 308.0 \times 0.0418}{5.28} = 4.88 \text{ \AA}$$

Therefore, the two innermost pairs of spots correspond to two sets of lattice planes located at 90° to one another at a lattice spacings of 4.44 Å and 4.88 Å. These lattice spacings correspond to either 100 or 010 or 001 planes of the unit cell whose projection is the diffraction pattern. 5-iodouracil forms monoclinic crystals (see below, the crystal structure of 5-iodouracil) in the space group $P2_1$. The b side of this crystal is the unique axis since it forms angles of 90° (α and γ) with c and a sides, whereas the angle between a and c sides is greater than 90°. In reciprocal space, the corresponding angles are α^* , β^* and γ^* between b^* and c^* , a^* and c^* and a^* and b^* respectively. These angles in the reciprocal space are related to the angles in the real space in the following manner:

$$\begin{aligned} \alpha^* &= \alpha = 90^\circ \\ \beta^* &= 180^\circ - \beta \\ \gamma^* &= \gamma = 90^\circ \end{aligned}$$

Since the angle between two of the axes in the diffraction pattern of 5-iodouracil is 90°, this implies that one of the two axes must be b^* and the other one could be either a^* or c^* . We further see, in the diffraction pattern, that along one of the two axes the intensity of alternate diffraction spots is extremely weak or negligible, which corresponds to systematic absences in the diffraction pattern. Such absences, for a monoclinic crystal, occur only in the

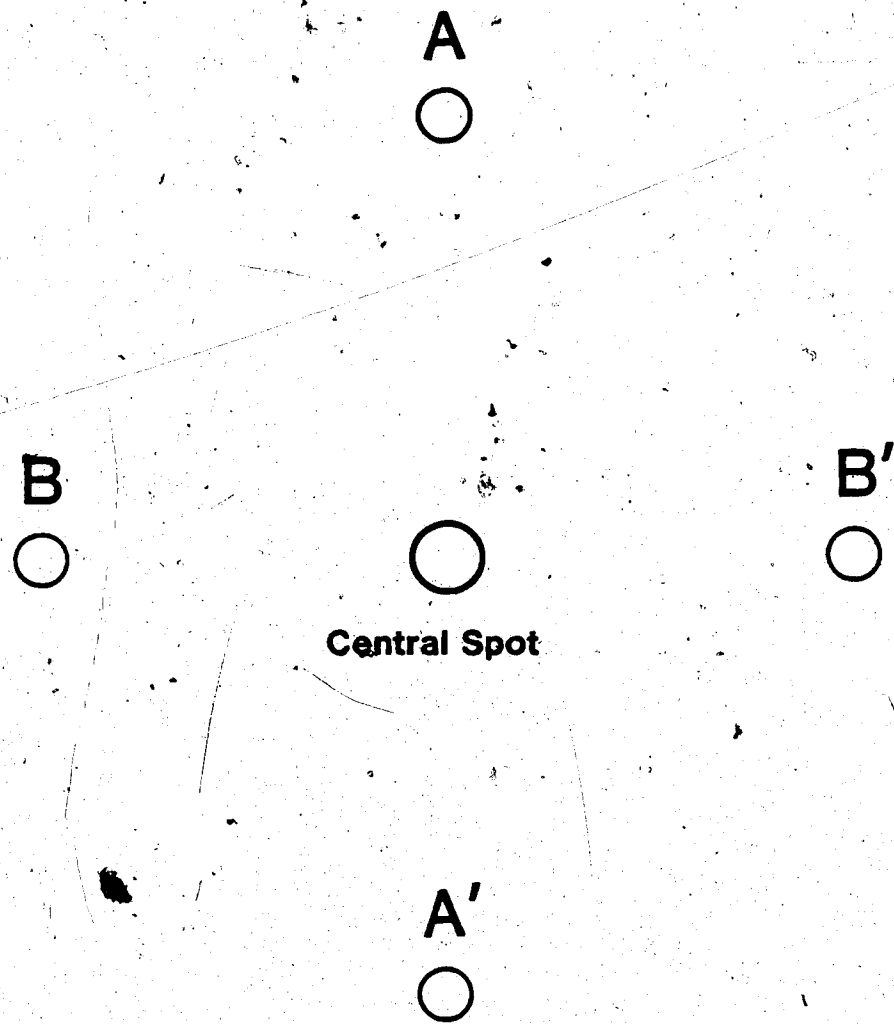


Figure 5.2 Location of the Innermost Spots around the Central Spot

b^* direction for all those $0k0$ spots for which $k=2n+1$, $n=1,2,3...$ (International Tables vol 2, 1967). In other words, if 1st, 3rd, 5th, etc orders of diffraction spots are very weak or absent along a particular direction for a $P2_1$ space group, then, that direction must correspond to the b^* axis. In Figure 5.2 OA direction should correspond to the b^* axis and OB direction could correspond to the either a^* or c^* axis. Since it was not possible to obtain three-dimensional data in the electron microscope as the tilt angle of the goniometer stage is limited to 30° , this ambiguity cannot be resolved from the two-dimensional diffraction pattern of 5-iodouracil. However, it is possible to conclusively index the OB direction from the three-dimensional X-ray diffraction pattern, which is described below:

The crystal structure of 5-iodouracil was determined by Sternglanz et al. in 1975 (Sternglanz et al., 1975). The following parameters describe the unit cell of 5-iodouracil,

Crystal Type : Monoclinic

Space Group : $P2_1$

$a = 14.210 \text{ \AA}$

$b = 4.458 \text{ \AA}$

$c = 4.899 \text{ \AA}$

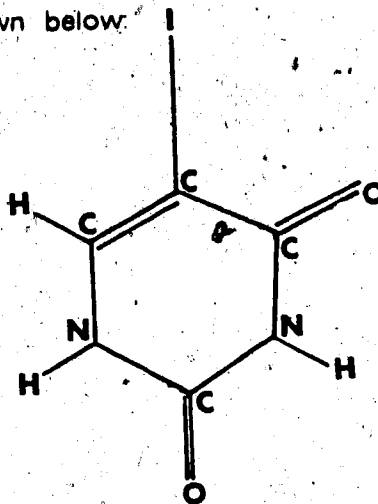
$\beta = 92.31^\circ$

number of formula units per unit cell = 2

Comparison of lattice constants of the unit cell of 5-iodouracil, as determined by X-ray diffraction, with the values calculated above, shows that the values of d_A and d_B are in close agreement (within 1%) with the b and c values calculated from X-ray diffraction data. This shows that OB corresponds to c^* axis. Thus, the indices of the first spot in the OA direction will be 010 and that of the first spot in the OB direction will be 001 . Or, the diffraction pattern corresponds to a set of $0kt$ reflections.

Crystal Structure of 5-iodouracil:

The crystal structure of 5-iodouracil was determined by Sternglanz et al., as mentioned above, in 1975. There are two molecules of 5-iodouracil per unit cell. The molecules form sets of hydrogen bonded ribbons which run in the the 011 and 0 $\bar{1}$ 1 directions. The molecular formula of 5-iodouracil is $C_4N_2O_2H_3I$ and its molecular structure is shown below:



The sets of ribbons run almost perpendicular to one another and the molecules in these two sets are connected together by intra-ribbon and inter-ribbon hydrogen bondings. Adjacent molecules which form ribbons are joined by the N(1)-H.....O(4) hydrogen bond, and different ribbons of molecules, perpendicular to one another, are joined by N(3)-H.....O(2) hydrogen bonds. Consequently, each molecule is connected to three other molecules by hydrogen bonds. The molecular ribbons are stacked at an inter-ribbon spacing of 3.15 Å.

Since the space group of 5-iodouracil is $P2_1$, the following relationship holds between the structure amplitudes of diffraction spots (International Tables, vol 1):

$$|F_{hkl}| = |F_{\bar{h}\bar{k}\bar{l}}| = |F_{h\bar{k}l}| \neq |F_{\bar{h}kl}| \text{ and } |F_{\bar{h}kl}| = |F_{h\bar{k}\bar{l}}|$$

Further, as the indexed diffraction pattern corresponds to the projection the along (100) direction, which is a set of $0kl$ reflections, for a two-dimensional diffraction pattern the above relationship reduces to:

$$|F_{0kl}| = |F_{0\bar{k}\bar{l}}| \text{ and } |F_{0kl}| = |F_{0k\bar{l}}|$$

or,

$$|F_{0kl}| = |F_{0k\bar{l}}| = |F_{0k\bar{l}}| \quad (5.3)$$

An intensity-weighted lattice of such a diffraction pattern of 5-iodouracil is shown in Figure 5.3. It consists of a set of $0kl$ and $0k\bar{l}$ spots of the diffraction pattern of 5-iodouracil, recorded at a cumulative dose of 6.4 C/m^2 .

The radii of various diffraction spots in this figure are equal to the square root of corresponding intensity values. The figure was drawn using a computer program CIRCLE.

5.3 Calculation of the Patterson Function

The three-dimensional Patterson function is calculated using equation 4.1, which is:

$$p(u, v, w) = \frac{1}{V} \sum_{h, k, l=-\infty}^{\infty} |F_{hkl}|^2 \exp[-2\pi i(hu + kv + lw)]$$

The diffraction pattern of 5-iodouracil corresponds to a set of $0kl$ reflections, so if S is the area of the bc plane of the unit cell of 5-iodouracil, equation 4.1 can be reduced to two-dimensional form as:

$$p(v, w) = \frac{1}{S} \sum_k \sum_l |F_{0kl}|^2 \exp[-2\pi i(kv + lw)] \quad (5.4)$$

Since 5-iodouracil crystallizes in the monoclinic system, in which the b side is the unique axis i.e. perpendicular to a and c sides, equation 5.4 can be written as (International Tables, vol 1, p 526):

$$p(v, w) = \frac{4}{S} \sum_k \sum_l |F_{0kl}|^2 \cos 2\pi kv \cos 2\pi lw \quad (5.5)$$

where the summation over k and l extends from 0 to ∞ . $|F_{0kl}|^2$ corresponds to the average intensity value of symmetry-related reflections i.e. of $0kl$ and $0k\bar{l}$.

A computer program, MODPAT, was written in Fortran to calculate the Patterson function using equation 5.5. In equation 5.5, v and w represent fractional coordinates of a point within a Patterson cell and vary between 0 and 1. Since the values of $|F_{0kl}|^2$ are known, the Patterson function $p(v, w)$

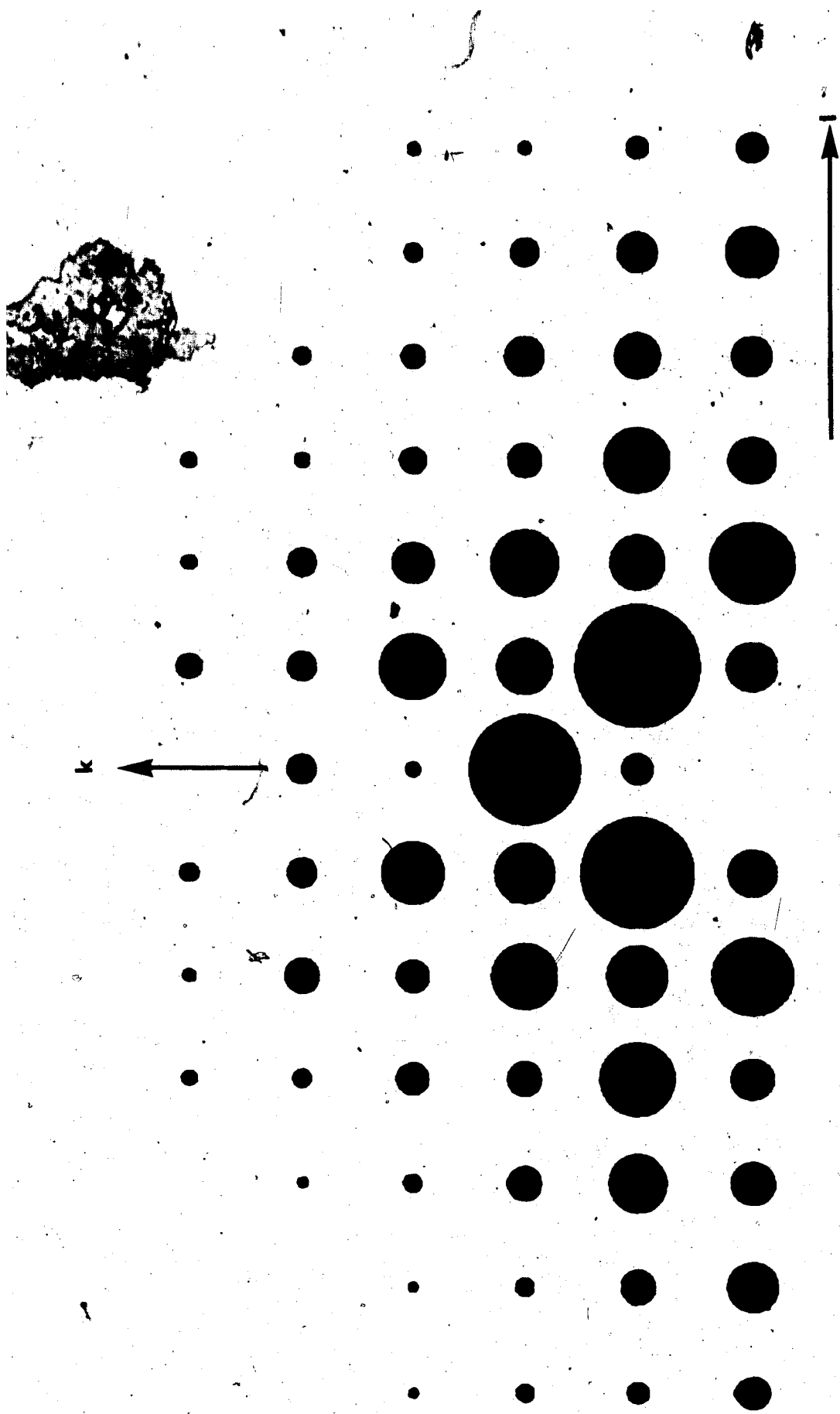


Figure 5.3 Intensity Weighted Diffraction Pattern of 5-Iodouracil

can be calculated for any point within the unit cell. The computation was performed for the values of v and w , increasing in steps of $1/60$; in other words, the unit cell was divided into a grid of 61×61 points and $p(v,w)$ was calculated at each node of the grid points. The $|F_{000}|^2$ term was excluded from the summations. As a result of this calculation, a total of 3721 numerical values of Patterson function were obtained. In order to interpret these numbers they are represented in a graphical form.

5.3.1 Contour Plots of the Patterson Function

The Patterson function numerical data calculated at certain distances within a unit cell, can be represented in the form of contour plots.

We know that p is a function of v and w , i.e.

$$p = f(v,w), \quad (5.6)$$

Since we have the values of p at the nodes of a grid at equal intervals in the v and w directions, contouring involves finding, for a constant value of p (contour value), points (v, w) which are then joined by a contour line. An interactive computer program CONTOUR was written using the University of Alberta subroutine CONTUR for the plotting of contours. This program permits the user to select the number of equi-spaced points needed to form the grid in two perpendicular directions and the dimensions of the sides of the unit cell; it also allows the user to decide the contour interval by first examining the Patterson function to determine the maximum and minimum values.

The computer programs for finding the Patterson function and drawing the contour plots were first tested using known test data. The crystal structure of the compound diglycine hydrobromide was determined by Buerger et al. (Buerger et al., 1956). The space group of diglycine hydrobromide is $P2_1 2_1 2_1$ and its two-dimensional Patterson function, $p(u,v)$, can be calculated using the following equation which is similar to equation 5.5:

$$p(u,v) = \frac{4}{S} \sum_h \sum_k |F_{hk0}|^2 \cos 2\pi hu \cos 2\pi kv$$

The Patterson function was calculated using the intensities of $hk0$ diffraction spots. The results of the contour map plotted using the CONTOUR program are shown in Figure 5.4(b). Figure 5.4(a) shows the Patterson function, $p(u,v)$, calculated by Buerger for the structure determination of diglycine hydrobromide. The close correspondence between the Patterson map calculated by Buerger and the one calculated using the computer programs MODPAT and CONTOUR establishes the correctness of these programs.

5.4 Calculation of B Value

The necessity of calculating the B value was discussed in Chapter 4. For the sharpening of the Patterson function a rough estimate of B value can be obtained using Wilson's method, as discussed in the preceding chapter. Calculation of B value requires information about the intensities of diffraction spots and the atomic scattering factors for electrons for all of the atoms present in a unit cell (at different values of $\sin\theta/\lambda$, where θ is the Bragg angle).

There are two molecules of 5-iodouracil per unit cell; a total of eight carbon atoms, four nitrogen atoms, four oxygen atoms, six hydrogen atoms and two iodine atoms per unit cell. The values of atomic scattering factor for electrons, f_{el} , at different $\sin\theta/\lambda$ values were obtained from Vainshtein's book (Vainshtein, 1964, Appendix IV). The plots of the atomic scattering factors with respect to $\sin\theta/\lambda$ for C, N and O are shown in the Figure 5.5(a) while Figure 5.5(b) shows similar plots for I and hydrogen.

Consider Figure 5.6 for the calculation of $\sin\theta/\lambda$. This Figure shows the diffraction of a beam of electrons by a set of planes, having an inter-planar spacing of d_{hkl} . L is the camera length, θ is the angle which the incident beam makes with the planes which is same as the Bragg angle. From the geometry of this figure, it is obvious that:

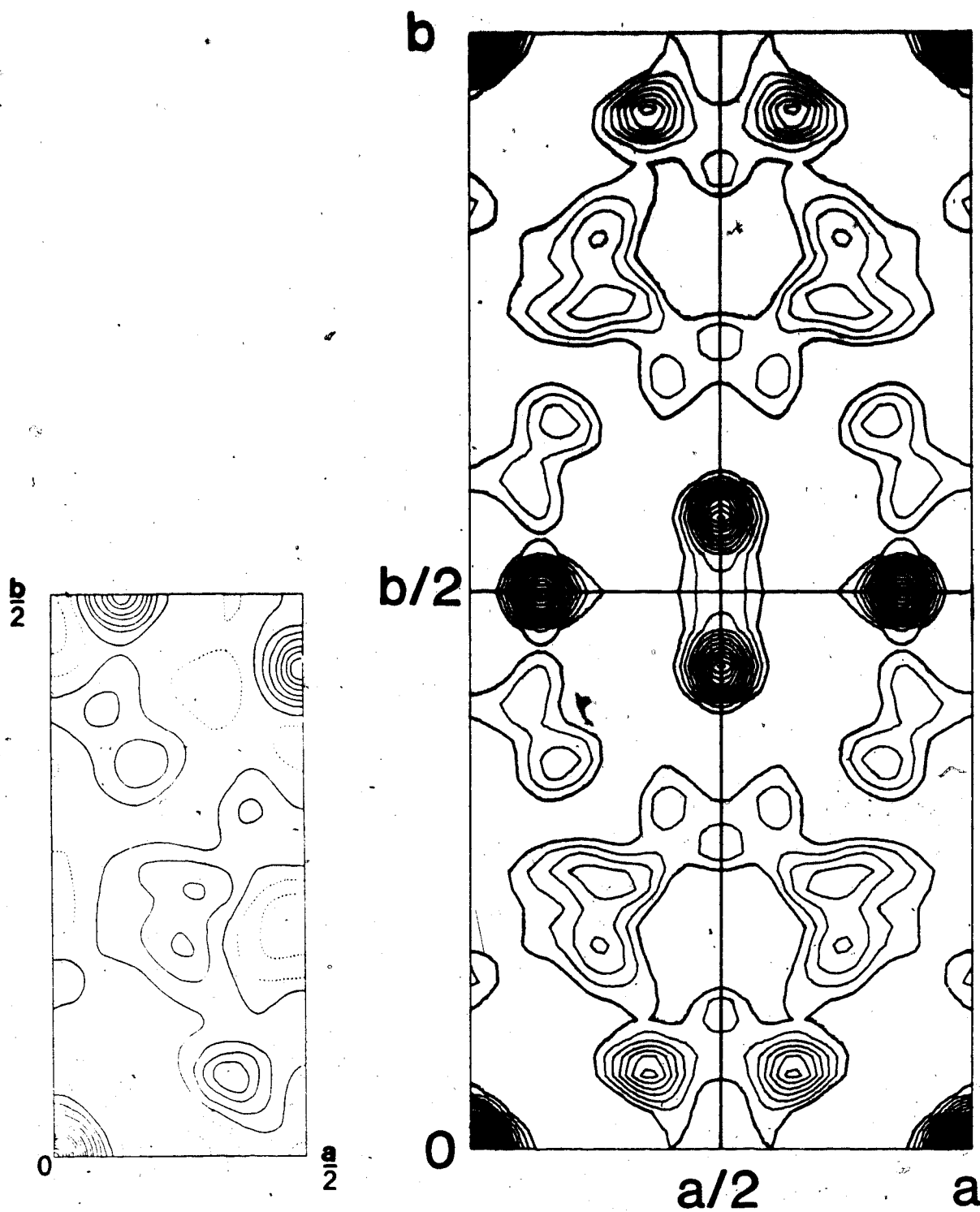


Figure (a)

Figure (b)

Figure 5.4 $p(u,v)$ Patterson Function as Calculated by Buerger (Figure a) and Calculated Using MODPAT and CONTOUR (Figure b)

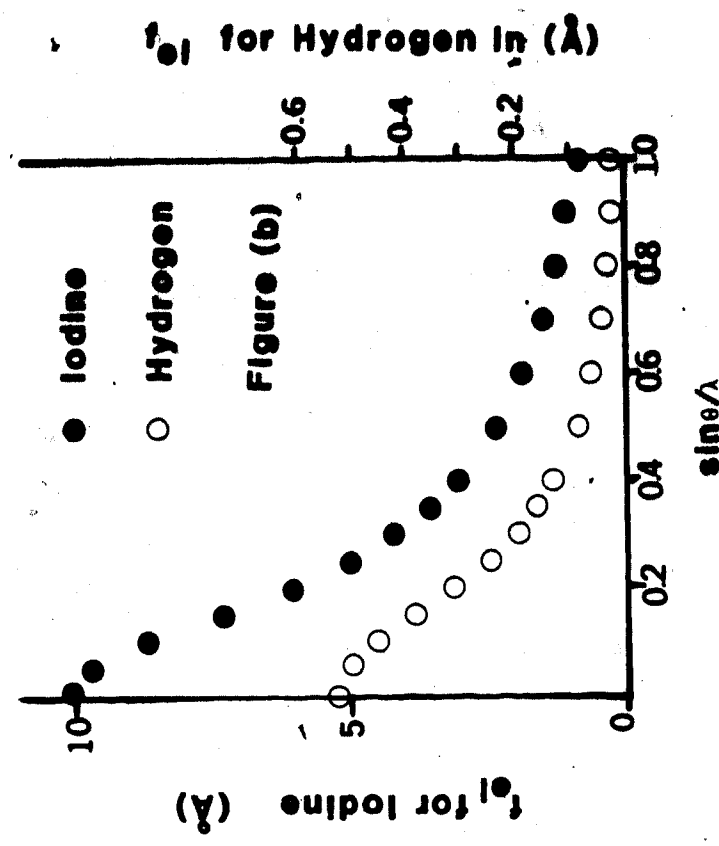
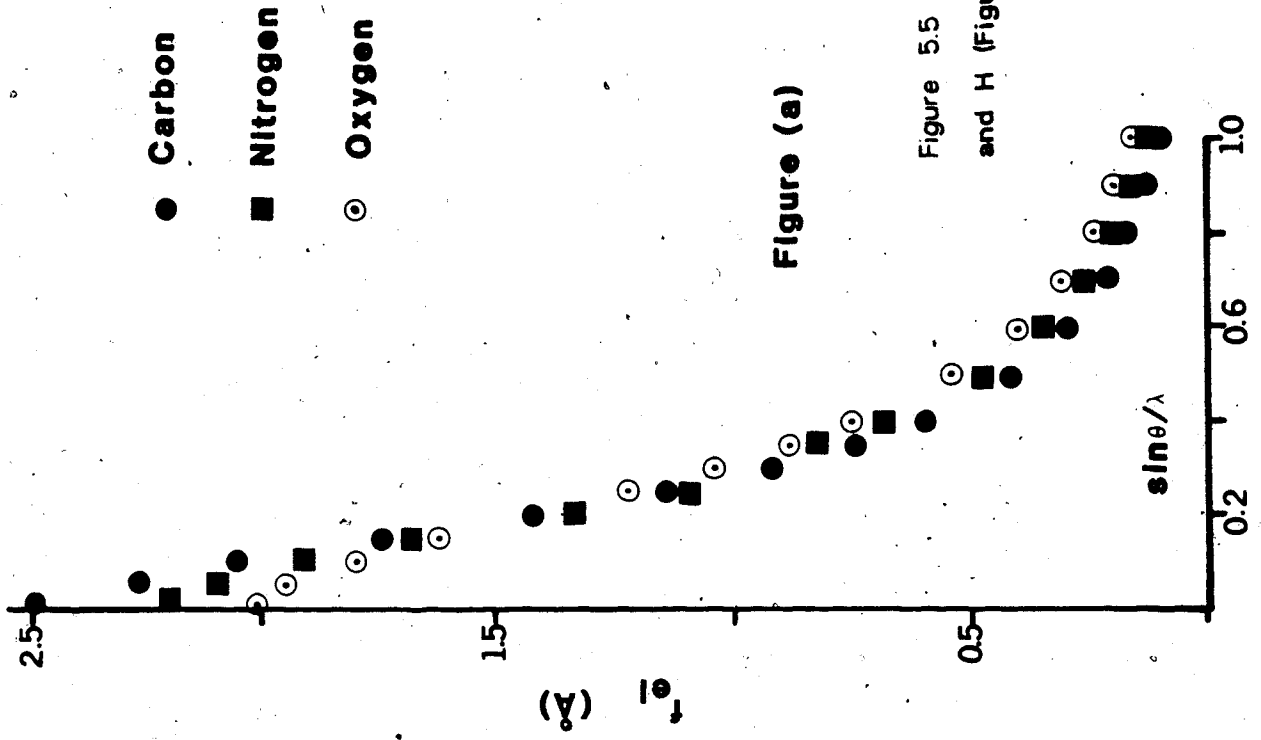


Figure (a)

Figure (b)

Figure 5.5 Atomic Scattering Factors for C, N and O (Figure a) and for I and H (Figure b) plotted with respect to $\sin\theta/\lambda$

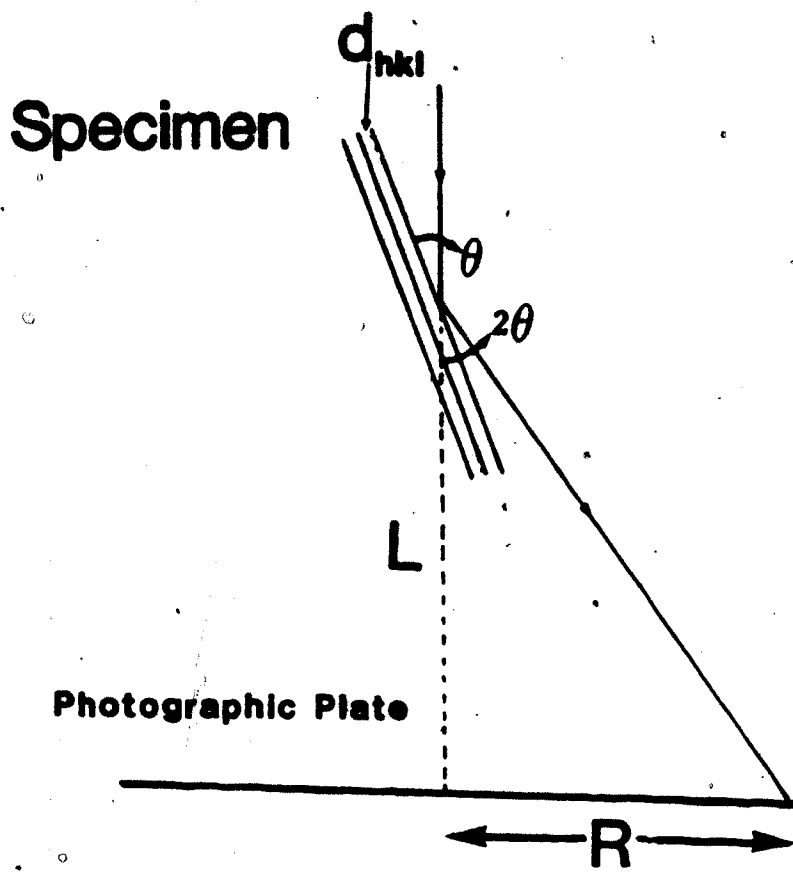


Figure 5'6 A Simple Schematic Diagram for the Calculation of $\sin\theta/\lambda$

$$\frac{R}{L} = \tan 2\theta \quad (5.7)$$

Further, according to Bragg's law, one has

$$\lambda = 2d_{hkl} \sin \theta \quad (5.8)$$

We can assume that $\tan 2\theta = 2\sin \theta$ provided θ is small, which usually is the case, then we can write from equation 5.7

$$\frac{\sin \theta}{\lambda} = \frac{R}{2L\lambda}$$

or,

$$\frac{\sin \theta}{\lambda} = \frac{2R}{4L\lambda} \quad (5.9)$$

where $2R$ is the distance between two symmetry related reflection spots.

Further, since $L = 308.0$ mm and $\lambda = 0.0418$ Å

$$\frac{\sin \theta}{\lambda} = \frac{2R}{51.5} \text{ Å}^{-1}$$

So, knowing the value of $2R$ in mm, we can calculate $\sin \theta / \lambda$ for each spot.

The intensities of a $0kl$ and $Ok1$ diffraction spots were plotted on a rectangular grid of lattice points at distances proportional to the corresponding distances in the original diffraction pattern, as shown in Figure 5.7. These plotted intensity values were divided into nine zones, at decreasing $\sin \theta / \lambda$ values which is equivalent to dividing into different zones of equal $(\sin \theta / \lambda)^2$ values, as is shown in the columns one to three of Table 5.1. Atomic scattering factors for C, N, O, H and I corresponding to mid-point values of $\sin \theta / \lambda$ are given in columns five to nine. Column 10 contains the values of $\sum_{i=1}^N e_i^2$ as determined from the values of atomic scattering factors given in columns 5 to 9. Column eleven contains the number of spots in each zone of $\sin \theta / \lambda$ and column twelve contains the average value of intensity $\langle |F_{0kl}|^2 \rangle$ for each zone calculated according to the procedure discussed in Chapter 4. Column thirteen gives the N value of $\ln\{g\}$ for each zone, where $g = \langle |F_{0kl}|^2 \rangle / \sum_{i=1}^N e_i^2$. Finally, column fourteen contains the mid-values for each $(\sin \theta / \lambda)^2$ region, given in column two.

Zone Number	Range of $\sin^2 \theta / \lambda^2$	Range of Mid Pt. $\sin \theta / \lambda$	Atomic Scattering Factors	Number of Spots	$\langle F_{0kl} ^2 \rangle$	$\ln\{g\}$	Mid $\sin^2 \theta / \lambda^2$	column number					
1	2	3	4	5	6	7	8	9	10	11	12	13	14
1	0-0.05	0-0.223	0.11	2.0	1.9	1.79	.44	8.5	205	8	102.8	-0.69	0.025
2	0.05-0.1	0.223-0.316	0.27	1.08	1.02	1.17	.44	4.7	63	8	51.6	-0.19	0.075
3	0.1-0.15	0.316-0.387	0.35	0.74	0.81	0.88	.16	3.5	35	9	44.0	0.22	0.125
4	0.15-0.2	0.387-0.447	0.42	0.55	0.62	0.69	.15	2.9	23	7	24.0	0.04	0.175
5	0.2-0.25	0.447-0.500	0.47	0.45	0.52	0.59	.09	2.5	17	6	19.0	0.11	0.225
6	0.25-0.3	0.500-0.547	0.52	0.39	0.45	0.51	.08	2.2	13	8	14.0	0.07	0.275
7	0.3-0.35	0.547-0.591	0.57	0.33	0.39	0.44	.06	2.0	10	7	7.0	-0.35	0.325
8	0.35-0.4	0.591-0.632	0.61	0.29	0.34	0.39	.05	1.7	8	8	6.0	-0.28	0.375
9	0.4-0.45	0.632-0.670	0.65	0.26	0.30	0.36	.05	1.6	7	5	3.0	-0.84	0.425

Table 5.1 Data Calculation for Wilson Plot

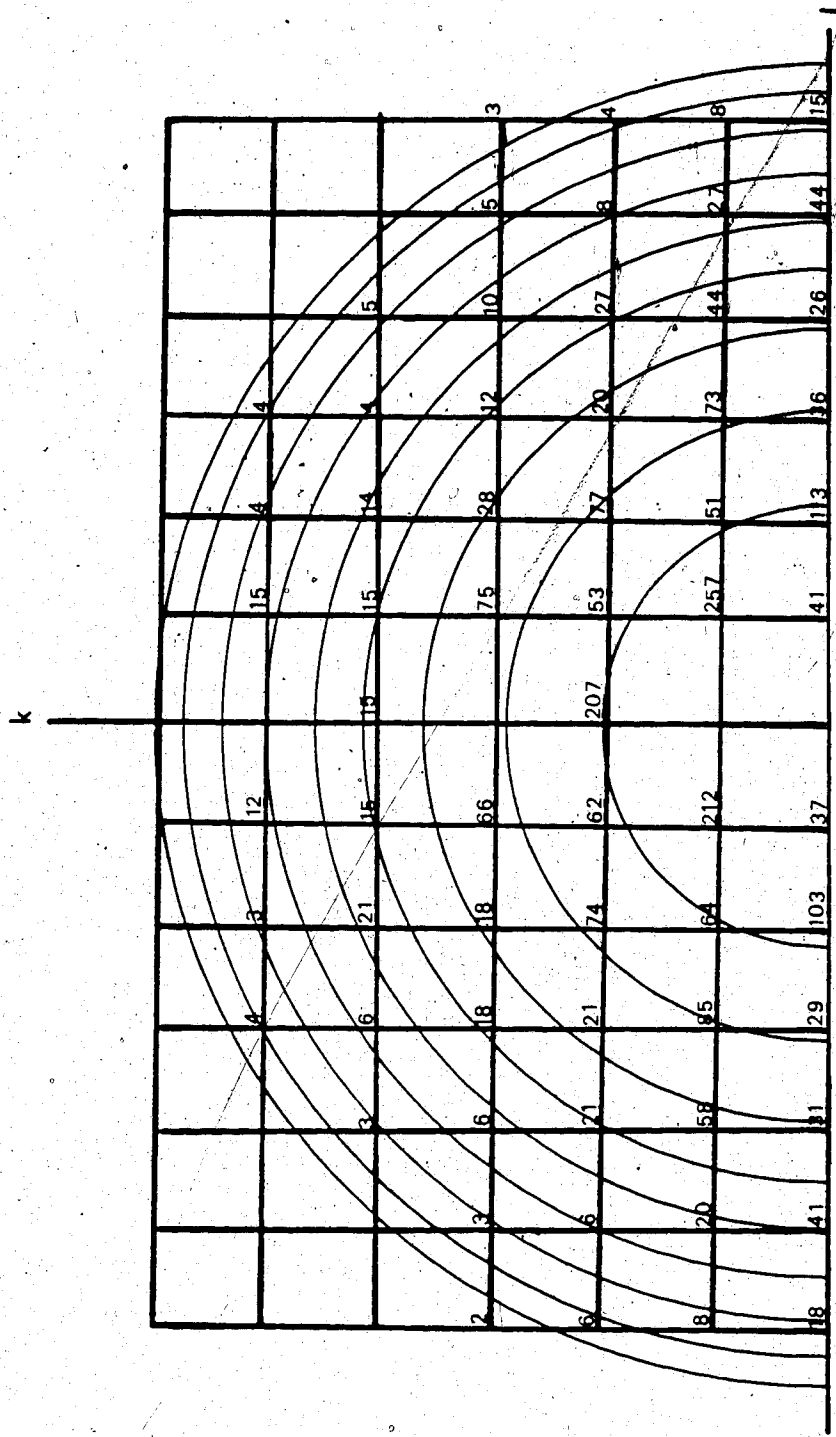


Figure 5.7 Zones of Decreasing $\sin\theta/\lambda$ for Wilson Plot

Figure 5.8 shows the graph of $\ln\{g\}$ against $(\sin\theta/\lambda)^2$, which was plotted using the data given in columns thirteen and fourteen of Table 5.1. A substantial scattering of data points is usually found in a Wilson plot (Blundell and Johnson, 1976), so the data was fed into a calculator to determine the slope and the y-intercept of the best fit line which was then drawn passing through the data points. The slope of this line was found to be -3.04 and since the slope of a Wilson plot is equal to $-2B$ so the value of B was found to be equal to 1.52 \AA^2 .

B was calculated in a similar manner for the diffraction patterns recorded at about 172 C/m^2 and 366 C/m^2 doses. The slopes of the corresponding Wilson plots gave a B value of 1.77 \AA^2 and 2.16 \AA^2 . B values for the diffraction patterns recorded at higher doses could not be calculated by Wilson's method as the decreasing number of diffraction spots (due to radiation damage) gave rise to poor statistical accuracy. The change in B value was found to be proportional to electron dose sustained by the specimen as is shown in Figure 5.9. The linear dependence of B on dose was utilised to evaluate the B value at higher doses by extrapolation of this straight line graph to higher doses.

5.5 Sharpening of the Patterson Function

The sharpening of Patterson function requires the calculation of intensities $|F_{hkl}|^2$ in the point-atom approximation. The method for the sharpening of Patterson function was discussed in the section 4.4 of the previous chapter. It involves the calculation of $|F_{hkl}^P|^2$ using the following equation:

$$|F_{hkl}^P|^2 = \left\{ \sum_{i=1}^N z_i^{1/3} / \sum_{i=1}^N f_i e^{i} \right\}^2 \exp[2B(\sin\theta/\lambda)^2] |F_{hkl}|^2$$

where N is the total number of atoms per unit cell. Since the diffraction patterns of 5-iodouracil corresponds to a set of $0kl$ reflections, equation 4.26 can be rewritten as:

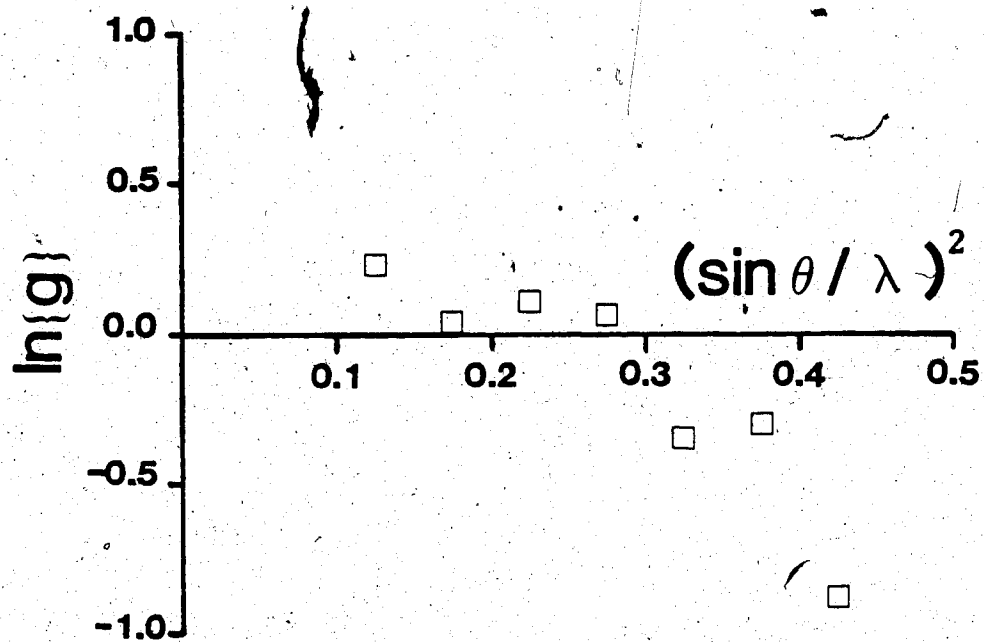


Figure 5.8 Wilson Plot at a Cumulative Dose of 6.4 C/m^2

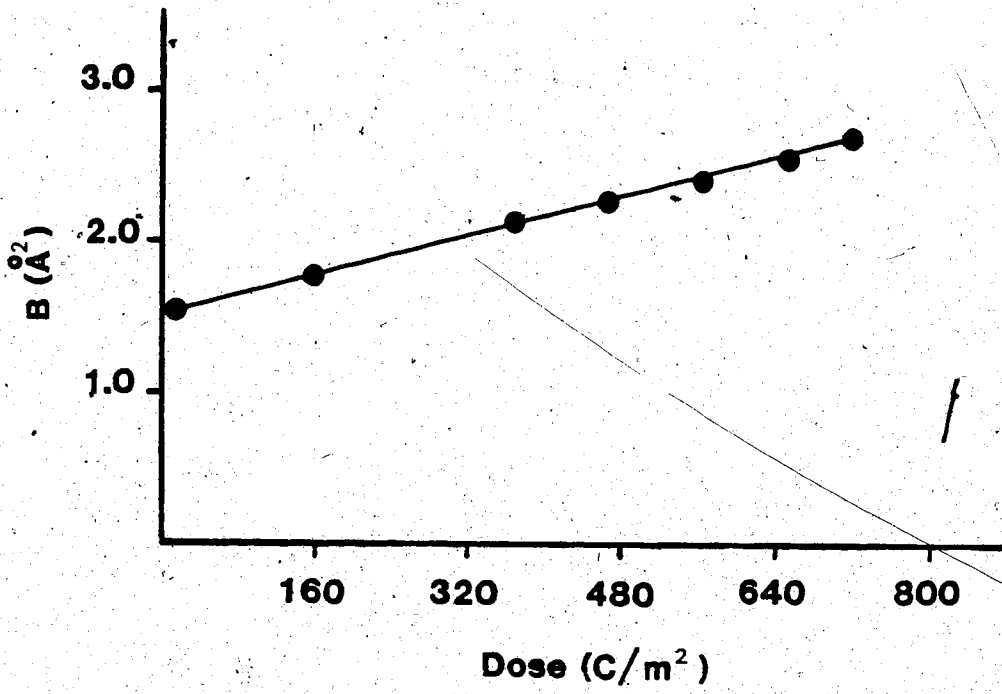


Figure 5.9 Dependence of B on Dose

$$|F_{0kl}^P|^2 = \left\{ \frac{\sum_{i=1}^N Z_i^{1/3}}{\sum_{i=1}^N f_{e1_i}} \right\}^2 \exp [2B(\sin\theta/\lambda)^2] |F_{0kl}|^2 \quad (5.10)$$

where $|F_{0kl}^P|^2$ are the intensities of $0kl$ reflection spots in point-atom approximation. Using the values of $|F_{0kl}^P|^2$ calculated using equation 5.10, instead of $|F_{0kl}|^2$ in equation 5.5, will give rise to a sharpened Patterson function.

Since the atomic numbers of I, C, N, O and H are 53, 6, 7, 8 and 1 respectively, the value of $(\sum_{i=1}^N Z_i^{1/3})^2$ for 8 carbon atoms, 4 nitrogen atoms, 4 oxygen atoms, 6 hydrogen atoms and 2 iodine atoms will be equal to 1904.44. The expression $(\sum_{i=1}^N f_{e1_i})^2$ in equation 5.10 can be calculated using the values of atomic scattering factors at different $\sin\theta/\lambda$ obtained from the f_{e1} curves drawn in Figure 5.6.

A computer program, SHARPIODO, was written based on equation 5.10 to compute the intensities of the diffraction spots in point-atom approximation, using the B values determined by Wilson's method at different doses of irradiation. The average value of the intensity of the symmetry-related reflection spots was used in the computation of equation 5.10. A set of $|F_{0kl}^P|^2$ values, obtained for all the diffraction patterns recorded at increasing dose was used for calculating sharpened Patterson functions, using equation 5.5. Computer programs MODPAT and CONTOUR were used again for computing the sharpened Patterson function and for plotting the data in the form of contour plots. A sharpened Patterson function was calculated at 3721 points within a unit cell by dividing the unit cell into a grid of 61 by 61 points.

To summarise: a series of electron-diffraction patterns of 5-iodouracil was recorded at increasing doses of irradiation at room temperature. The diffraction patterns so obtained were indexed and densitometer traces were obtained of all the diffraction spots using Joyce-Loebl microdensitometer. Cumulative electron irradiation received by the specimen was calculated by measuring the beam current using a Faraday cup located at the screen level of the JEM 100B electron-microscope. The peak area above the background of all

the peaks was calculated using the integrating unit of MOP-3. The peak areas so obtained yielded the relative intensities of diffraction spots. Computer programs MODPAT and CONTOUR were used to calculate and plot Patterson function, by substituting the relative intensities in equation 5.5. Next, Wilson's method was used to calculate B values for the first three diffraction patterns belonging to the damage series at increasing doses. B values for the subsequent diffraction patterns were obtained by the extrapolation of a straight line graph between B against electron doses. The intensities of $0k1$ spots in the point-atom approximation were calculated using these B values in the computer program SHARPIODO. This resulted in a set of $|F_{0k1}^p|^2$ values for all the diffraction patterns recorded at increasing doses, which were then substituted in equation 5.5. The sharpened Patterson function was calculated and plotted using the computer programs MODPAT and CONTOUR.

5.6 Results and Discussion

There are two molecules of 5-iodouracil per unit cell and since the molecular formula of 5-iodouracil is $C_4N_2O_2H_3I$, there are a total of eighteen non-hydrogen atoms in the unit cell (The peaks involving hydrogen atoms would be too weak to appear in the Patterson map) Theoretically, these 18 atoms must give rise to a total of $18(18-1)$ i.e. 306 non-origin peaks. On the other hand, from an experimental point of view the distinguishability of Patterson peaks is governed by the following two factors:

1. Area of the plane of the unit cell whose projection gives rise to a diffraction pattern, and
2. The atomic numbers of two elements which contribute to a Patterson peak.

The significance of the first point mentioned above can be appreciated in the following way. When the electron beam is parallel to one of the zone axes one gets a diffraction pattern which is a projection of the crystal structure on a plane perpendicular to the direction of the beam. If there are N atoms in a unit cell, then a Fourier Series calculated using Fourier amplitudes from the intensities of diffraction spots and respective phases should give rise to a total

of N peaks, provided none of the atoms occur on top of one another in the unit cell. A Patterson function calculated using the intensities of the diffraction spots would have to accommodate a total of $N^2 > N$ peaks in the same area of the unit cell. This greatly increased number of Patterson peaks, compared to the Fourier peaks calculated using phases and Fourier amplitudes, would result in a considerable overlap of Patterson peaks and their distinguishability would be poorer. However, one can hope to achieve an increased distinguishability of Patterson peaks by recording a diffraction pattern which corresponds to the projection of the crystal structure onto the plane of largest area of the unit cell. In other words, the interpretation of the Patterson function is easiest for the projection of a cell having the largest area (Buerger, 1959). In the compound 5-iodouracil, the a - c face of the unit cell is of largest area, so a Patterson function calculated using the intensities of $h0l$ spots of the diffraction pattern should consist of peaks of maximum distinguishability. However, such a projection could not be obtained, due to inherent limitations imposed by the construction of the goniometer stage itself. Since the crystals of 5-iodouracil grew on the b - c face of the unit cell so obtaining a diffraction pattern corresponding to a - c face would require tilting the specimen in the microscope column by 90° . Such a tilt angle is not possible in principle. Consequently the distinguishability of Patterson peaks in the b - c projection of the unit cell is not expected to be very good.

As discussed in the previous chapter, the strength of a Patterson peak is related to the atomic numbers of the corresponding atoms. 5-iodouracil has two iodine atoms per unit cell. One would expect that the peaks between an iodine atom and other atoms of the unit cell will be considerably more prominent compared to the peaks between, for example, carbon-carbon, carbon-nitrogen or nitrogen-oxygen atoms. Since there are eighteen non-hydrogen atoms in a unit cell of 5-iodouracil, each iodine atom will form a total of seventeen peaks with other non-hydrogen atoms. The presence of two iodine atoms per unit cell would result in a total of thirty-four Patterson peaks within a unit cell. Due to centro-symmetric nature of Patterson function,

if there is a peak due to iodine-carbon vector then there will exist another peak on the other side of the origin due to carbon-iodine vector. Consequently, due to the centre of symmetry, there will be a total of sixty-eight peaks within a unit cell. However, only those peaks which lie in one quarter of the unit cell will form an independent and unique set of peaks, as the peaks in the other quadrants will all be symmetry related.

The distribution of Patterson peaks between iodine and other atoms of the unit cell is shown in Figure 5.11. This Figure has been drawn in the following manner (Buerger, 1959). The coordinates of all the atoms in a unit cell of 5-iodouracil were calculated by Sternglanz et al. (1975). Knowing these atomic coordinates, the $p(b\ c)$ projection (in the following discussion, the axes of the Patterson map will be denoted by a , b and c instead of u , v and w , for a greater conceptual clarity.) of the Patterson function can be constructed by first drawing the positions of the molecules in a unit cell (called unit cell sheet). Figure 5.10 shows four adjacent unit cells of 5-iodouracil, surrounding a common center point (the scale in this figure is reduced to one half of the original scale in order to accommodate the figure). The inner rectangle corresponds to a single unit cell of 5-iodouracil which has this point at its center. A tracing paper was used to determine the locations of Patterson peaks. To begin with, a unit cell was drawn on the tracing paper with the origin at its center. The four unit cells drawn earlier, on the unit cell sheet, were kept fixed on a drawing table while the tracing paper was placed over the unit cell sheet with its cell outlines parallel to the cell outlines in the unit cell sheet. Next, the tracing paper was moved over the unit cell sheet, without changing its orientation, such that the origin of the Patterson sheet fell over one of the iodine atoms. At this particular position of tracing paper the locations of all the atoms lying within the outlines of Patterson cell were marked on the tracing paper. Then the tracing paper was moved to the other iodine atom in the parallel orientation and again the locations of all the atoms of 5-iodouracil, falling within the domain of the Patterson cell were marked on it. Each such placement of the tracing paper on two iodine atoms resulted in seventeen

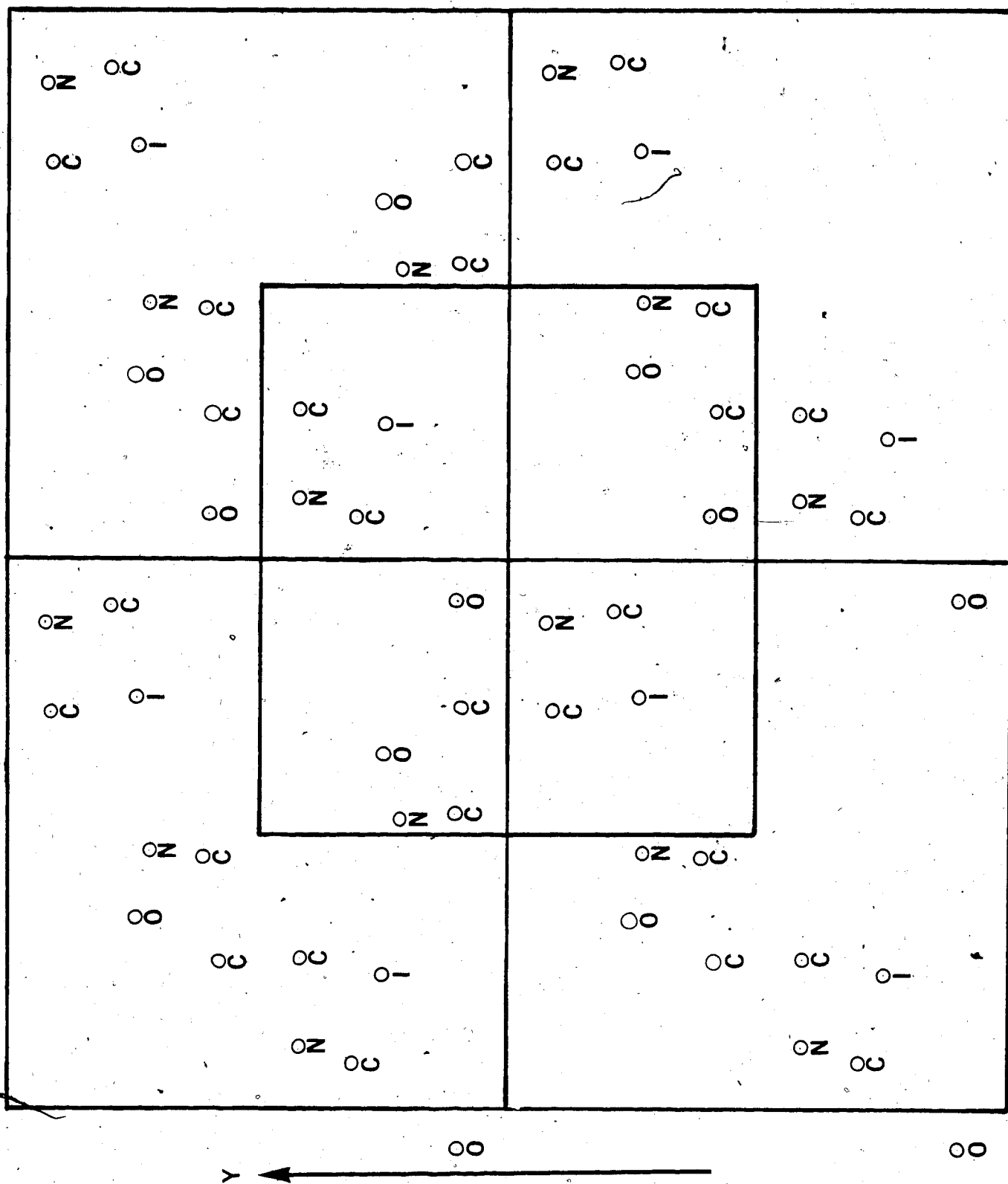


Figure 5.10 Four Adjacent Cells of 5-iodouracil Around a Common Centre Point (the inner cell encloses two molecules of 5-iodouracil)

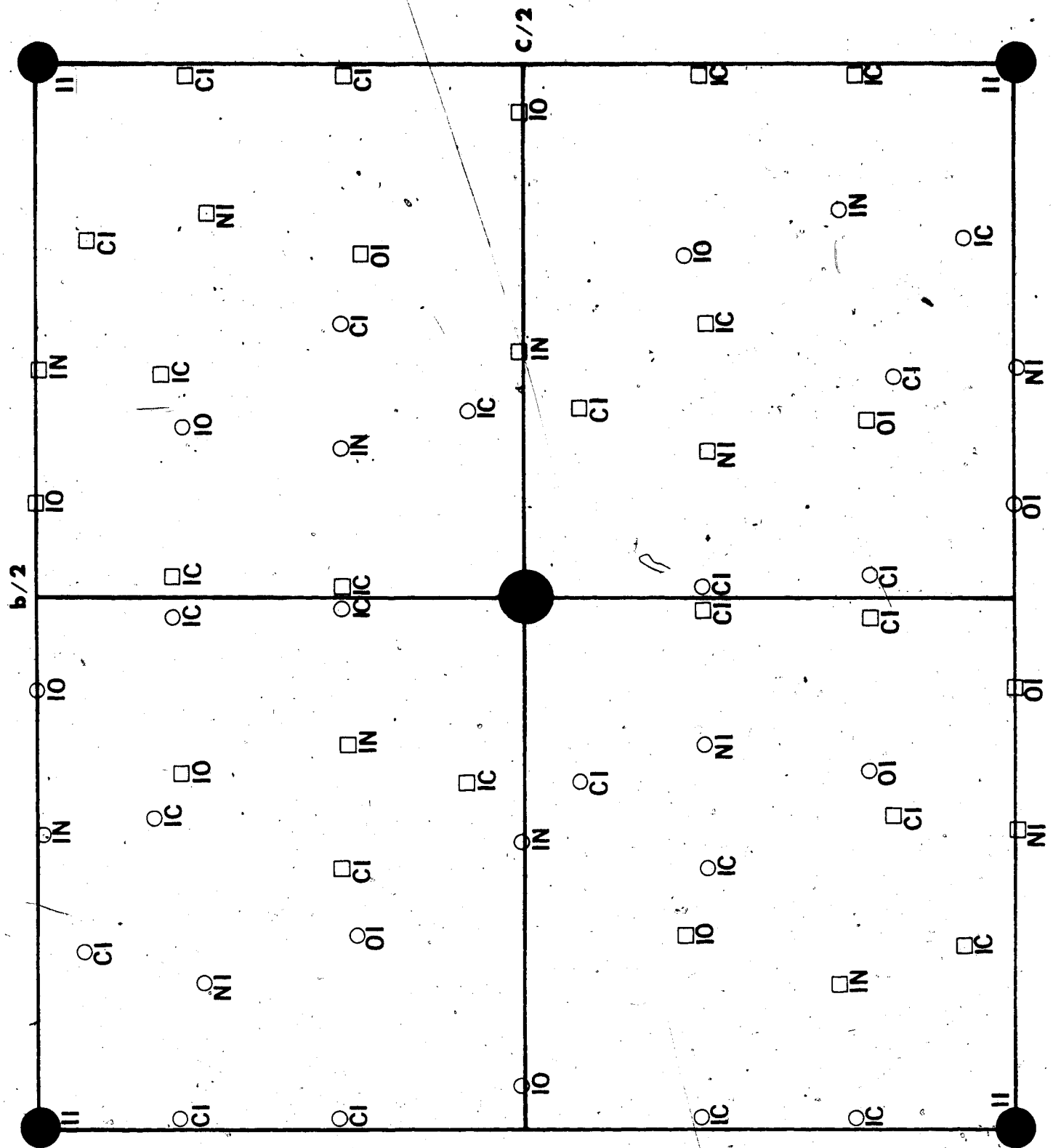


Figure 5.11 Patterson peaks due to Iodine and Other Atoms of Figure 5.10

peaks on the tracing paper. Due to centro-symmetric nature of Patterson peaks an equivalent number of Patterson peaks would appear on the opposite side of the origin. For example, if a peak were obtained due to iodine-carbon vector by putting the tracing paper origin on iodine atom, a peak would also be obtained for the same pair of atoms by placing the origin of the tracing paper sheet on the carbon atom. In Figure 5.11 the open circles correspond to the peaks obtained by placing the tracing paper origin on one iodine atom and the open squares correspond to the peaks obtained by placing the tracing paper origin on the other iodine atom of the unit cell. Under each peak are written the symbols of elements responsible for that particular peak. The first symbol corresponds to the location of the origin of the Patterson cell.

The Patterson map shown in Figure 5.12(a) corresponds to the diffraction pattern of 5-iodouracil recorded at 6.4 C/m^2 . Besides a peak at the origin which is due to the autocorrelation of the self vectors, a second prominent peak occurs at $(b/2, c/2)$. Comparison of this Patterson map with the one shown in Figure 5.11 shows that the peak at $(b/2, c/2)$ is due to the iodine-iodine vector. Although the peaks along $b=c=0$ and $b=c=0.5$ axes appear quite distinctly, in the region within these axes peaks seem to overlap and hence are not so distinct. The effect of sharpening this Patterson map can be seen in Figure 5.12(b), in which the distinguishability of peaks has improved and the peaks within the quadrant are more distinct compared to the peaks in Figure 5.12(a). A comparison of Figure 5.12(b) with the one calculated on the basis of the known atomic coordinates (Figure 5.11) shows that the peaks along $c=0$ and $c=0.5$ axes are due to the vectors between iodine and carbon atoms whereas the peaks lying along $b=0$ and $b=0.5$ axes are due to iodine-oxygen and iodine-nitrogen vectors. The peaks numbered 6 and 9 are due to the overlapping of iodine-carbon and iodine-oxygen vectors. A total of nine peaks appears in each quadrant besides the origin peak, which is less than what one would expect from consideration of the number of atoms per unit cell. However, this is understandable since the diffraction pattern corresponded to the projection of the crystal structure onto the plane of the smallest area.

Patterson maps calculated for each diffraction pattern recorded at increasing dose are shown in Figures 5.12(b) to 5.13(d). As a result of irradiation the changes in the specimen structure can be seen from these Patterson maps. The peaks in the Patterson maps either shift, overlap and merge with each other, or completely disappear. Further, the damage seems to affect either one peak at a time or all the peaks, at different stages of irradiation. Table 5.2 summarises the effect of irradiation on different peaks.

Significant changes occur during the initial stages of irradiation as is obvious from Figures 5.12(b) and 5.12(c). Some peaks are seen to shift along $b=0$, $c=0$ or $c=0.5$ axes. Peak 1 seems to rearrange along the $c=0.5$ axis that is parallel to b axis, whereas peak 2 disappears and peaks 6 and 9 merge with the adjacent peaks. This initial rearrangement of the molecule is followed by a relatively unchanged Patterson map of Figure 5.12(d), in which except of the disappearance of peak 3 no other peak registers any further shift. However, in the Patterson map shown in Figure 5.13(a), a broad band occurs running parallel to the b axis, seemingly due to the overlap of peaks along $c=0.5$ axis. This broad band remains present in the subsequent two Patterson maps of Figures 5.13(b) and 5.13(c). In Figure 5.13(b), however, another peak besides the one at $(b/2, c/2)$ seems to exist, corresponding to the position of peak 5 in Figure 5.13(b). In the last Patterson map, shown in Figure 5.13(d) only one distinct peak exists at $(b/2, c/2)$, in addition to the origin peak.

Although only those peaks which are due to iodine and other atoms of the unit cell are being discussed here, it is worth pointing out that one cannot disregard the existence of the peaks due to lighter elements. From the space group considerations of 5-iodouracil, there would be peaks occurring along the c axis at $b=0.5$, due to symmetry-related equivalent atoms. For example, the large peak at $(b/2, c/2)$ due to iodine-iodine vector would contain contribution from symmetry related carbon and oxygen atoms also.

A reorientation of the molecules would indeed affect all the peaks appearing in the Patterson map, though maybe to different degrees. Since the molecules of 5-iodouracil are joined together by relatively weak hydrogen

PEAK NUMBER	DOSE (Cm^{-2})							
	171.5	366	963.3	558	655.3	719.3		
1	SHIFTS PARALLEL TO b AXIS	NO CHANGE	OCCURS AT (b/2, c/2)	NO CHANGE	NO CHANGE	A LARGE PEAK APPEARS AT (b/2, c/2). COVERING THE REGION OF PEAKS		
2	DISAPPEARS	-	-	-	-	-		
3	SHIFTS PARALLEL TO c AXIS	DISAPPEARS	-	-	-	-		
4	SHIFTS PARALLEL TO c AXIS	NO CHANGE	MERGES	NO CHANGE	NO CHANGE	DISAPPEARS		
5	SHIFTS PARALLEL TO b AXIS	NO CHANGE	MERGES	NO CHANGE	NO CHANGE	ONLY ONE PEAK EXISTS AT (b/2, c/2), COVERING THE REGION OF PEAK 5		
6	MERGES	NO CHANGE	DISAPPEARS	-	-	-		
7	SHIFTS PARALLEL TO b AXIS	NO CHANGE	MERGES	NO CHANGE	NO CHANGE	DISAPPEARS		
8	SHIFTS PARALLEL TO b AXIS	NO CHANGE	MERGES	NO CHANGE	NO CHANGE	DISAPPEARS		
9	MERGES	NO CHANGE	DISAPPEARS	-	-	-		

PATTERSON MAP FOR UNDAMAGED CRYSTAL

Table 5.2 Effect of Irradiation on Patterson Peaks

bonds, during the initial stages of irradiation, the deposition of energy could break these bonds allowing molecules to undergo orientational changes in the crystal structure. The splitting of the peak at $(b/2, c/2)$, which is seen in Figures 5.12(c) and 5.12(d) may not involve iodine atoms only, as the peaks due to symmetry related carbon and oxygen atoms also fall around the same region. That this is indeed the case is evident from Figure 5.13(a) and the subsequent ones which show a large peak occurring at $(b/2, c/2)$, the location which exactly corresponds to iodine-iodine vector. Due to lack of three-dimensional information, it is not possible to say in which directions the molecular reorientation takes place; however, due to molecular reorientation the distinguishability of Patterson peaks (for example peaks 6 and 9) seems to be getting poorer (see later).

The initial deposition of energy may leave the pyrimidine ring structure intact because of the sharing of deposited energy amongst all the bonds, due to resonance. However, as irradiation increases, one notices from Figure 5.12(d) that peak 3 disappears from the Patterson map, whereas other peaks are not significantly affected. The disappearance of peak 3, which is due to iodine-nitrogen vector, is indicative of damage to the ring structure. Resonance stabilization of the ring seems to weaken very rapidly once initial damage has occurred to the ring, as is evident from the subsequent Patterson map shown in Figure 5.13(a), in which most of the prominent structural features, present in Figures 5.12(b) to 5.12(d), are lost. Damage to the nitrogen atom, belonging to the ring structure, must cause rearrangement within the molecule which leads to considerable structural disorder.

An assessment of disorder is also provided by the B factor, which is also termed the Debye-Waller factor, temperature factor or displacement factor. In the case of perfect crystalline order the B factor is simply related to the mean square displacement (or vibration) of atoms from their lattice sites. When the specimen is irradiated in an electron beam, the disorder increases within a unit cell and a factor due to lattice disorder contributes to the apparent mean square displacement. The disorder in the lattice may involve both translational

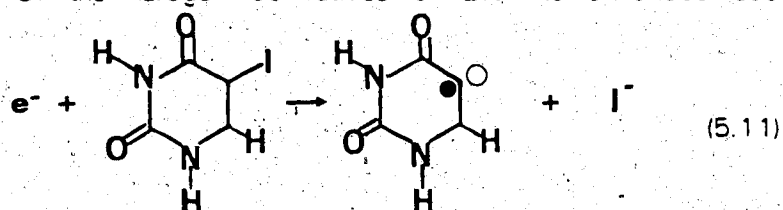
and/or rotational components. At small irradiation dose, as in Figure 5.12(b), the B factor possesses a certain value which can be related to the contributions due to the vibrating atoms primarily (the value which one would obtain, for example, from X-ray diffraction data), but at higher dose B factor was found to increase (increment being proportional to the dose). Indicating that the atomic vibration is not the only factor contributing to B value, at higher doses, but ensuing rotation of the molecule and/or displacement are also contributing to an increase in the B value. Since its value was found to depend upon the 'disorderliness' of the crystal structure, be it vibrational, rotational or displacement disorder, it would be appropriate to call B a disorder factor.

For a perfect crystal, the value of atomic scattering factor declines rapidly (with respect to the scattering angle) depending upon the B value. A higher B factor gives rise to a faster decline of the atomic scattering factor of a particular atom, which results in the gradual decrease in the intensity of the diffraction spots with increasing scattering angle. Since the shapes of the f -curves (a plot of atomic scattering factor as a function of scattering angle) are similar for all the atoms, except of the scale factor which depends on the atomic number of an element, one can visualize an average shape of the f -curve for all the atoms in a molecule (Harker et al., 1948). Moreover, the disorder factor B, as determined by Wilson's method, provides an estimate of the B factor for all the atoms in a unit cell and is not a measurement of the individual B value of each atom. Considering radiation damage in terms of scattering power of ordered arrays of molecules in certain specific directions, one can associate an increase in B value with a faster decline in the slope of the average shape of the scattering factor. Since an increase in B value does not necessarily mean a greater amplitude of atomic vibrations but could be due to rotational and/or translational disorder of molecules, a faster decline of the average shape of the scattering factor would amount to the broadening of Patterson peaks and the peaks would tend to overlap. It is quite likely, hence, that with increasing irradiation the distinguishability of Patterson peaks worsens due their broadening and eventual overlapping, as is observed for example in

Figure 5.13(a), in which as a result of disorder to the ring structure most of the peaks are lost and peaks due to carbon and iodine atoms have spread to form a broad band running parallel to the *b* axis.

Elimination of iodine does not seem to take place, as is evident from Figure 5.13(d) in which one sees a large peak still existing at (*b*/2, *c*/2). The peak due to iodine-iodine vector is seen to expand, covering the region which includes peak 5 due to iodine-carbon vector. Therefore, although most of the structural features are destroyed at this high dose of about 719 C/m^2 , some long range order involving iodine and carbon atoms still seems to exist.

The liberation of iodine ions has been detected from aqueous solution studies using pulse conductimetry and pulse radiolysis techniques on DNA in which a fraction of thymine bases was replaced by 5-iodouracil. It was found that the radiation sensitivity of the halogen derivatives of DNA is enhanced due to the following reaction:



which results in the formation of an iodine ion and a highly reactive σ radical (Zimbrick et al., 1969; Bansal et al., 1972). Elimination of iodine, however, was not detected from the single crystals of 5-iodouracil and their nucleoside derivatives (Huttermann, 1982). Riederer et al. found that under solid-state conditions and in a neutral environment, iodine elimination is at most a minor event if it occurs at all (Riederer, 1981).

5.7 Factors Contributing to Artifacts in the Intensity Data

There are certain factors which might affect the intensity of diffraction spots and any application of the intensity data for the computation of Patterson function would be incomplete without discussing the nature of these artifacts and their effect upon the analyses. So long as the simple kinematic approximation for the diffraction of electrons by the crystal potential is valid, there exists a straightforward relationship between the crystal potential and the intensities of the diffraction spots. In the kinematic approximation of electron

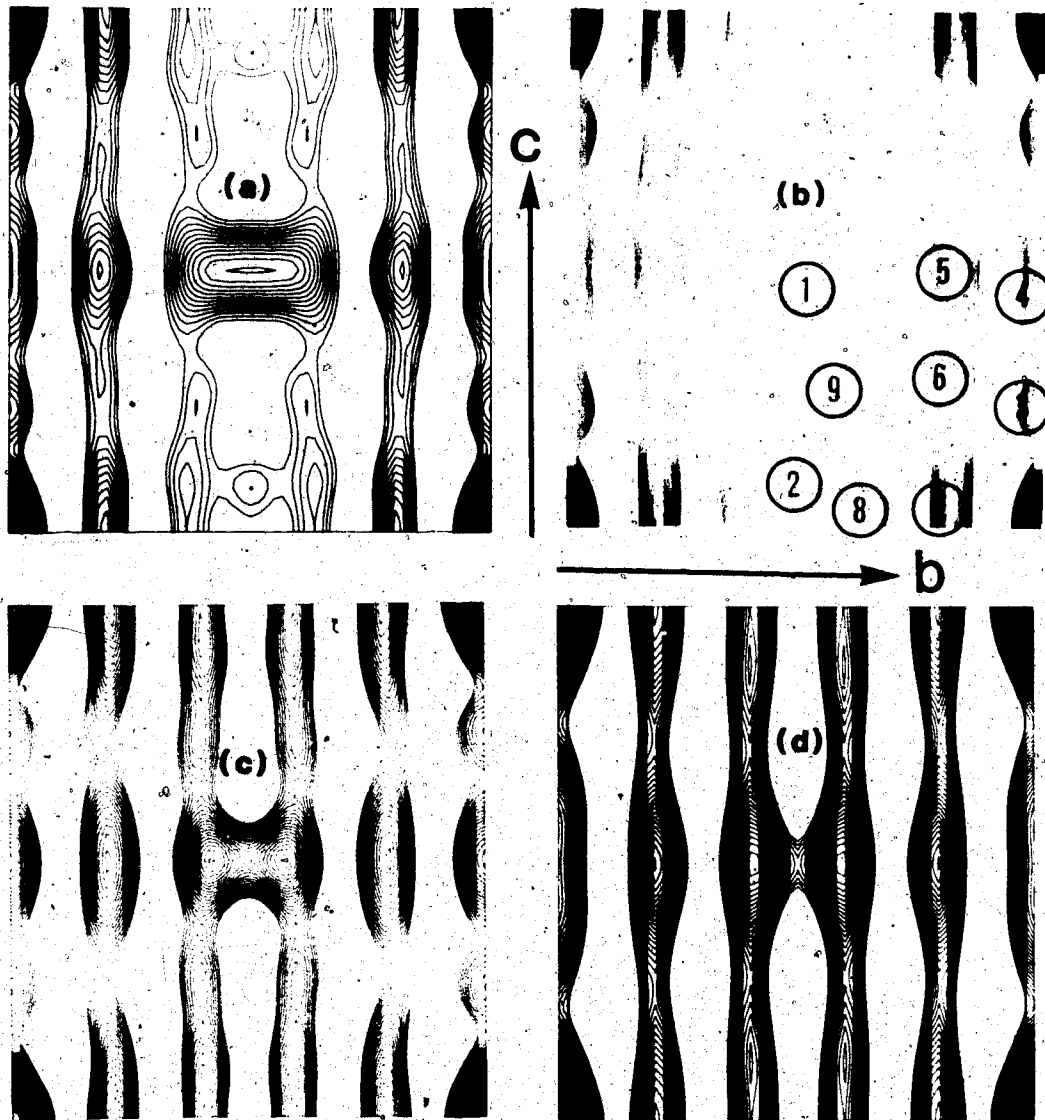


Figure 5.12 (a) and (b) Unsharpened and Sharpened Patterson Functions for a Dose of 6.4 C/m² (c) and (d) Sharpened Patterson Functions for Doses of 171.5 and 366 C/m² respectively

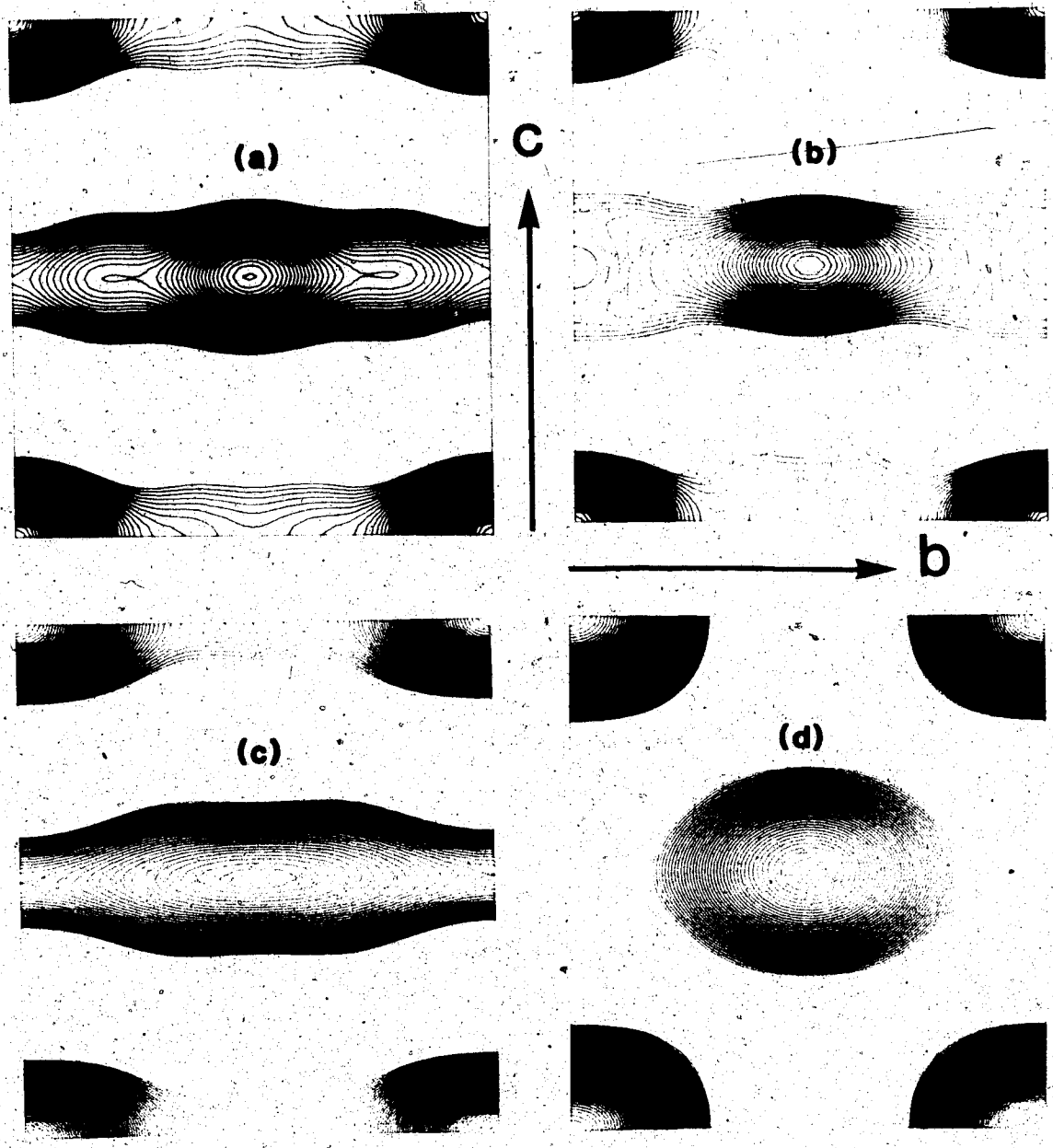


Figure 5.13 (a) to (d) Sharpened Patterson Functions Corresponding to Doses of 463.3, 558, 655.3 and 719.3 C/m² respectively

specimen interaction the projected crystal potential can be determined by computing a Fourier series involving the intensities of diffraction spots as Fourier coefficients along with their phases. However, when the amplitude of the diffracted wave becomes very large, the diffracted wave may itself get scattered by the atoms (Hirsch et al., 1977). The breakdown of the kinematic approximation becomes more and more probable with increasing specimen thickness. In such cases, for the diffraction spots belonging to small spatial frequencies the diffracted intensity can exceed the incident intensity and kinematic approximation will then not be a valid description of the scattering process.

An assessment of the validity of kinematic approximation can be made by comparing the intensity of the strongest diffraction spots with that of the incident beam. According to Vainshtein (1964, also Dorset et al., 1975) the ratio of the scattered intensity in a diffraction spot to the intensity received by the crystal is proportional to the square of the structure amplitude and to the square of the crystal thickness.

Or,

$$\frac{I_{hkl}}{J_0 S} = \lambda^2 \frac{F_{hkl}^2}{V^2} t^2 \quad (5.12)$$

where I_{hkl} is the integrated intensity of a spot having indices h , k and l , F_{hkl} is the structure factor, J_0 is the intensity of the primary beam on the specimen, S is the area of the specimen irradiated by the beam, V is the volume of the unit cell, λ is the wavelength of the electrons and t is the thickness of the crystal. For kinematic approximation to be valid, the ratio of the intensity of each spot to $J_0 S$ must be less than one.

Equation 5.12 was tested for three spots in order of decreasing intensities (011, 020 and 002) 011 being most intense. $J_0 S$ in equation 5.12 was estimated by finding the area under the central densitometer trace through the incident beam spot (Dorset, 1975). The ratio of the intensity of the most

intense spot to that of the incident beam intensity was found to be about 0.18 and hence small compared to 1. Since equation 5.12 is valid only for kinematic diffraction conditions, a small value of $I_{hkl} / J_0 S$ for the most intense diffraction spot suggests that the effect of dynamical scattering on the intensities of diffraction spots should be small. For a symmetrical diffraction pattern (when the electron beam is parallel to one of the crystallographic axes) when the crystal thickness is such that the dynamical scattering is just beginning to occur, its effect is mainly confined to diffraction spots of small spatial frequencies. However, with increasing crystal thickness, the intensity of high spatial frequency spots also gets affected by dynamical scattering. In other words, for thin crystals the intensity data for small spatial frequency spots may be affected by dynamical scattering but this would not affect the information obtained by a Patterson synthesis, since the effect would be confined to low resolution information.

From kinematic theory and space group considerations, the $0k0$ spots ($k=2n+1$, $n=0, 1, 2$ etc.) are forbidden in the diffraction pattern of 5-iodouracil. The appearance of 010 spot in the diffraction pattern indicates a slight departure from a perfect kinematic case, even for a crystal having a small thickness of about 120 \AA . The intensity of 010 spot, however, was found to be very small, about 1% of the incident beam intensity.

A quantitative measure of the symmetry preserved in diffraction pattern is provided by the value of the reliability index R_{sym} (also called R-factor) (Blundell and Johnson, 1976) which reflects the agreement between the symmetry related reflections. For the preservation of Friedel symmetry in a diffraction pattern we may denote R_{sym} by R_f . If the intensity of a diffraction spot h,k is given by I_{hk} , the R_f for the preservation of Friedel symmetry is given by

$$R_f = \frac{\sum_{h,k} |I_{hk} - I_{\bar{h}\bar{k}}|}{\sum_{h,k} |I_{hk} + I_{\bar{h}\bar{k}}|} \quad (5.13)$$

Using equation 5.13 the R-factor for Friedel symmetry from the diffraction pattern of 5-iodouracil was found to be equal to 0.09. A small value of R-factor implies a good degree of agreement in the intensities of spots related by Friedel symmetry, which, in turn, also provides information about the precision of crystal setting. The R-factor of 0.09 for 5-iodouracil can be compared with the R-factors obtained by Dumont et al. (1981) from the diffraction pattern of purple membrane which was found to range between 0.16 and 0.25 and also with the R value of 0.198 determined by Wallace and Henderson (1982). Dumont et al. used their intensity data for locating the heavy atom binding sites in the structure and for determining the phases for high resolution diffraction orders. Whereas, Wallace and Henderson used the intensity data for the calculation of Fourier projection maps. Tivol et al. (1982) also determined R factor from the diffraction pattern recorded from the hydrated microcrystals of rat hemoglobin and found it to range between 0.05 and 0.09. Low values of R-factor led them to prove the authenticity and reproducibility of diffraction patterns. This data provides an indication of the expected range of R-factor values and suggests that a value of 0.09 determined from the diffraction pattern of 5-iodouracil is indicative of good preservation of Friedel symmetry in the diffraction pattern.

Small intensity of the strongest diffraction spot compared to that of the central spot together with good preservation of Friedel symmetry as determined by a small value of R-factor suggests that the scattering was mainly kinematical. However, the appearance of very faint but discernible forbidden reflection provides evidence of some dynamic interaction between scattered beams. Hence it seems that the scattering in these samples was mainly kinematical but with a slight degree of dynamic scattering in the low spatial frequency diffraction spots.

A correction of intensities of diffraction spots in the presence of forbidden reflections was made by Cowley et al. (1951) and a comparison of Fourier projections was made from the diffraction pattern of dicycyl ($C_{32}H_{66}$) using observed and corrected values. Both sets of intensity data were found to

reveal the general arrangement of the molecules, for example the location of carbon atoms; but the detection of hydrogen atoms required the use of intensity data corrected for forbidden reflections. Since the detection of the peaks involving hydrogen atoms has not been attempted from the Patterson map of 5-iodouracil and only peaks which involve iodine atoms have been identified, the correction of the intensities of diffraction spots for the appearance of forbidden reflection is not expected to provide additional information.

The effect of dynamical scattering on Patterson function has been made by Cowley and Moodie (1959). The effect is primarily confined to changes in height and diameter of Patterson peaks; however, the position of the peaks remains unchanged in the case of slight dynamical scattering. Since identification of the peaks obtained from the diffraction pattern of 5-iodouracil was not made on the basis of their height and diameter but involved a comparison of the computed Patterson map with the one made by the method of graphical autocorrelation of molecules, the effect of slight deviation from kinematic scattering should be of little consequence in the analysis of Patterson function.

Contamination in the microscope column may also alter the intensity of diffraction spots. However, contamination should have little effect on the diffraction pattern of 5-iodouracil because very low doses and liquid nitrogen anti-contamination device were used. Further evidence for the absence of contamination is the fact that the carbon K-loss (measured by EELS) did not increase during the recording of electron diffraction patterns.

CHAPTER VI

CONCLUSIONS

In this thesis an attempt has been made to assess the mechanisms of electron irradiation damage to certain crystalline biomolecules. An analysis of the damage process has been made in terms of structural damage to the crystal lattice and chemical damage to molecules. This kind of division in the mechanism of radiation damage is more due to the type of method being used for damage assessment than due to any fundamental and distinct delineation between the loss of crystalline order and molecular damage. Since a crystal is a three-dimensional array of individual molecules, any damage to the crystal structure (as assessed by the fading of the diffraction spots) may also involve damage to the molecules. It has been a general belief that structural damage to the crystalline lattice is followed by chemical damage (elemental loss) to the molecules. However, it has emerged from this study of radiation damage that it is not always correct to assume that structural damage precedes chemical damage. The mechanism of radiation damage seems to be highly dependent upon various inter- and intra- molecular bondings which are responsible for holding the crystal together.

In the case of biological compounds, the presence of hydrogen bonds is nearly ubiquitous. It is possible that the weak nature of hydrogen bond renders them very susceptible to damage by electron irradiation and hydrogen bonds are readily damaged under the electron beam. Such a disturbance to the crystal may affect the regularity of molecular packing in the crystal.

The damage mechanism in amino acids could be due to two factors. Bond scission seems to be an important cause of radiation damage at relatively large irradiation doses, doses which are comparable to the characteristic doses for low spatial frequency diffraction spots. However, the characteristic doses calculated from the G-values suggest that some other mechanism of radiation damage (possibly rotation of side chains) should be responsible for the initial loss in intensity of high spatial frequency diffraction spots.

Subsequent stages of radiation damage seem to be very much dependent upon the molecular structure of different compounds. For example conjugated molecules were found to be more resistant to radiation damage compared to the unconjugated ones.

However, the peripheral atoms (surrounding the ring of conjugated structures) in nucleic acid bases were found to be quite susceptible to radiation damage. The characteristic doses for elemental losses involving peripheral atoms were comparable to the characteristic doses measured for the fading of high spatial frequency diffraction spots. Although resonance stabilization does provide greater stability to conjugated molecules, the initial disorder in crystal structure may not only involve rupture of hydrogen bonds but also be due to elemental losses of peripheral atoms.

On the other hand in compounds like cysteine and methionine, the deterioration of the crystal structure seems to take place very rapidly, as seen by fast-decaying diffraction spots, but elemental loss involving sulphur atoms seems to be a more gradual process. On the basis of these results and as a reasonable hypothesis one can say that the location of an atom in the structure and the various types of bondings with which it is connected to other atoms, seem to govern its sensitivity to electron irradiation.

For the first time, an effort was made to use a crystallographic technique involving the Patterson function for the assessment of radiation damage. Application of the Patterson function technique to the assessment of damage in 5-iodouracil resulted in the description of damage process in terms of a damage parameter which was found to be proportional to electron irradiation. Patterson maps revealed the effect of irradiation at different stages of exposure of the specimen to the electron beam. Damage to the pyrimidine ring structure (as determined by the disappearance of the I-N peak) was followed by the disappearance of most of the peaks from the Patterson map, signifying a deterioration in crystalline order. Patterson maps also revealed that at a relatively high dose of about 719 C m^{-2} most of the high-resolution structural features are destroyed but the long range order is preserved by iodine atoms bonded to carbon atoms.

The presence of a heavy atom, such as iodine in 5-iodouracil, facilitates the identification of peaks in a Patterson map but poses a disadvantage due to an increased amount of dynamic scattering. The presence of dynamic scattering would prevent a simple interpretation of Patterson peaks. Especially if the Patterson function is applied to study radiation damage in a compound of unknown structure, the identification of the Patterson peaks could be extremely difficult in the presence of severe dynamical scattering. It is then necessary to have a very thin crystal in order to minimize dynamic

scattering.

In order to learn more about the mechanism of radiation damage, further experiments could be conducted on other compounds of known crystal structure. It would be desirable to obtain the diffraction patterns corresponding to the projection of the structure on the largest area of the unit cell as this would result in an enhanced distinguishability of Patterson peaks.

The use of a Patterson function for radiation damage studies would be particularly interesting for those compounds whose structure is not completely known. For example, certain long chain polymers and oligopeptides (such as polylysine) form α -helical structures arranged in a hexagonal lattice; the crystals of such compounds could be useful for studying the effect of irradiation. A Patterson function computed from the diffraction patterns of such structures would indicate the location of peaks due to inter-atomic vectors belonging to the helices, and also the peaks due to helices and side chains. An analysis of different Patterson functions corresponding to diffraction patterns recorded at increasing doses could provide information about the damage to helical structures.

It is generally believed that no appreciable damage to a biological compound occurs below a dose of about 16 C m^{-2} (Stenn and Bahr, 1970). By recording diffraction patterns at small dose intervals and below the dose of 16 C m^{-2} it would be informative to calculate the Patterson function to determine if any detectable damage takes place at such small values of doses. Especially if the intensity of the high spatial frequency spots drops due to irradiation, the effect may be noticeable in the Patterson maps.

In this thesis, an emphasis was directed toward better understanding of the mechanism of radiation damage, which is desired for devising methods for eventually reducing the damage itself. However, cooling the specimen by liquid nitrogen and liquid helium has for long been considered a possible solution to the problem of radiation damage. In the case of electron diffraction, several measurements have been carried out at low temperatures on various specimens. Glaeser et al. (1971) found that no significant improvement occurred in the stability of diffraction patterns at low temperatures, whereas Siegel (1972) found an improvement of about 5 times in the stability of electron diffraction pattern at liquid helium temperatures. In the case of uranyl acetate-stained catalase crystals, Glaeser et al. (1975) found that the damage actually increased at low

temperatures compared to that at room temperature.

Analysing the low-loss region of the electron energy-loss spectra of nucleic acid bases Isaacson et al. (1973) found no improvement in the stability of these compounds at 90 K. However, according to Egerton (1980c) the loss of carbon and oxygen decreased by a factor of 10-100 upon cooling the specimen down to a temperature of 100 K from the room temperature.

This data indicates that the effect of cooling the specimens, as assessed by diffraction and electron energy-loss measurements, can be very different; ranging from no improvement in the stability of diffraction patterns to a large improvement as determined by EELS. The mechanism of cryoprotection is also unclear. It is hoped, however, that by conducting simultaneously electron energy-loss and diffraction measurements on a crystalline specimen, both at room temperature and at low temperature, it would be possible to correlate the information obtained by these two methods for a better understanding of cryoprotection. Further, by analyzing differences in the Patterson maps, computed from the the diffraction patterns recorded at room temperature and at liquid nitrogen and/or liquid helium temperatures, it might be possible to study the mechanism of cryoprotection. Also, information gained in this manner could be used in conjunction with the information obtained about the chemical damage (as assessed by EELS) for a better understanding of the mechanism of cryoprotection.

BIBLIOGRAPHY

- Agar, A.W., R.H. Alderson and D. Chescoe, 1980, Practical Methods in Electron Microscopy, Vol 2 (Principles and Practice of Electron Microscope Operation), Chapter 7, (ed. Audrey M. Glauert), Elsevier/North-Holland Biomedical Press, Amsterdam, Netherlands.
- Bacq, Z.M. and Peter Alexander, 1966, Fundamentals of Radiobiology, Pergamon Press, London.
- Bansal, K.M., L.K. Patterson, R. Schuler, 1972, J. Phys. Chem. 76, 2386.
- Baumeister, W. and W. Vogell (eds.), 1980, Electron Microscopy at Molecular Dimensions, Springer-Verlag, Berlin.
- Beeston, B.E.P., R.W. Horne and R. Markham, 1972, Practical Methods in Electron Microscopy, Vol 1 (Electron Diffraction and Optical Diffraction Techniques), (ed. Audrey M. Glauert), American Elsevier Publishing Co., Inc., New York.
- Bethe, H., 1928, Annal. Phys. 5, 325.
- Blundell, T.L. and L. N. Johnson, 1976, Protein Crystallography, Academic Press, New York.
- Bracewell, R. N., 1978, The Fourier Transform and its Applications, McGraw-Hill Book Co., New York.
- Bragg, W.H. and W.L. Bragg, 1913, Proc. Cambridge Phil. Soc. XVII, 43.

Buerger, M.J., E. Barney and T. Hahn, 1956, Z. Krist. **108**, 130.

Buerger, M.J., 1959, Vector Space and its application in crystal-structure investigation, John Wiley and Sons, Inc., New York.

Clark, W.R.K., J.N. Chapman, R.P. Ferrier, 1979, Nature, **277**, 368.

Clark, W.R.K., J.N. Chapman, A.M. Macleod and R.P. Ferrier, 1980, Ultramicroscopy, **5**, 195.

Cooley, J.W. and J.W. Tukey, 1965, Math. Comput. **19**, April 1965, 297.

Corbett, J.W., 1966, Electron Radiation Damage in Semiconductors and Metals in Solid State Physics, Supplement 7, (eds. F. Seitz and D. Turnbull), Academic Press, New York.

Cosslett, V.E., 1975, J. of Microscopy, **105**, Pt. 3, 269.

Cosslett, V.E., 1978, J. of Microscopy, vol **113**, Pt. 2, 113.

Cowley, J.M., A.L.G. rees and J.A. Spink, 1951, Proc. Phys. Soc. A **64**, 604.

Cowley, J.M. and A.F. Moodie, 1959, Acta Cryst. **12**, 360.

Cowley, J.M., 1981, Diffraction Physics, 2nd edition, North-Holland Publishing Co., Amsterdam.

Davisson, C.J. and Germer, L.H., 1927, Nature, **119**, 558.

Dorset, D.L. and D.F. Parsons, 1975, Acta Cryst. A **31**, 210.

Dumont, M.E., J.W. Wiggins and S.B. Hayward, 1981, Proc. Natl. Acad. Sci. Vol. 78, No 5, 2947.

Egerton, R.F. and M.J. Whelan, 1974, Phil. Mag. 30, 739.

Egerton, R.F., 1975, Phil. Mag., 31, 199.

Egerton, R.F., C.J. Rossouw and M.J. Whelan, 1976, Development in Electron Microscopy and Analysis, (ed. J. Venables), Academic Press, London.

Egerton, R.F., 1978, Ultramicroscopy, 3, 43.

Egerton, R.F., 1979, Ultramicroscopy, 3, 39.

Egerton, R.F., 1979b, Ultramicroscopy, 4, 169.

Egerton, R.F. and D. Kenway, 1979, Ultramicroscopy, 4, 221.

Egerton, R.F., 1980a, SEM II, Scanning Electron Microscopy Inc., (ed. M.A. Hayat), AMF O'Hare, Chicago.

Egerton, R.F., 1980b, Instt. Phys. Conf., Ser No. 52, Chapter 7, p 323.

Egerton, R.F., 1980c, Ultramicroscopy, 5, 521.

Egerton, R.F., 1981, Ultramicroscopy, 6, No. 6, 297.

Egerton, R.F., 1982, Ultramicroscopy, 10, 297.

Ferrel, R.A., 1957, Phys. Rev., 107, 450.

Gejvall, T. and G. Lofroth, 1975, Rad. Effects, 25, 187.

Glaeser, R.M. and G. Thomas, 1969, Biophys. Jour., 9, 1073.

Glaeser, R.M., 1971, J. Ultra. Res., 36, 466.

Glaeser, R.M., V.E. Cosslett and U. Valdre, 1971, J. Microscopie (Paris), 12, 133.

Glaeser, R.M., 1975; in Physical Aspects of Electron Microscopy and Microbeam Analysis, (eds. B.M. Siegel and D.R. Beaman), 205, John Wiley and Sons, New York.

Glaeser, R.M. and L.W. Hobbs, 1975, Jour. of Microscopy, 103, 209.

Gottschall, W.C. Jr. and B.M. Tolbert, 1968, J. Phys. Chem., V 72 No. 3, 922.

Hall, C.R., 1965, Phil. Mag., 12, 815.

Handbook of Chemistry and Physics, 1981, E 170, Chemical Rubber Company, Cleveland, Ohio.

Harding, M.M. and H.A. Long, 1968, Acta Cryst. B24, 1096.

Henderson, R. and P.N.T. Unwin, 1975, Nature, 257, 28.

Harker, D. and J. S. Kasper, 1948, Acta Cryst., 1, 70.

Hillier and Baker, R.F., 1944, J. Appl. Phys., 15, 663.

Hirsch, P., A. Howie, R.B. Nicholson, D.W. Pashley and M.J. Whelan, 1977, Electron Microscopy of Thin Crystals, Robert E. Krieger Publishing Company, Huntington, New York.

International Tables for X-ray Crystallography, 1965, Volume 1, (eds. Norman F. M. Henry and K. Lonsdale), Birmingham England: The Kynoch Press.

International Tables for X-ray Crystallography, 1967, Volume 2, (eds. J. S. Kasper and K. Lonsdale), Birmingham England: The Kynoch Press.

Isaacson, M., 1972, J. Chem. Phys., Vol. 56, No.5, 1803.

Isaacson, M., 1972, J. Chem. Phys., Vol 56, No.5, 1813.

Isaacson, M., D. Johnson and A.V. Crewe, 1973, Rad. Res. 55, 205.

Isaacson, M., 1974, Electron Microscopy, Vol. 2, p 680, Australian Academy of Sciences, Canberra.

Isaacson, M., 1977, in Principles and Techniques of Electron Microscopy Biological Applications, (ed. M.A. Hayat), Chapter 1, Van Nostrand Reinhold Co., New York.

Joy, D.C., R.F. Egerton, D.M. Maher, 1979, SEM 1979, (ed. O. Johari), 81, SEM Inc., Chicago.

Kobayashi, K., 1965, Quant. Elec. Micr., (eds. G.E. Bahr and E.H. Zeitler), 1097, Williams and Wilkins Co., Baltimore.

Kobayashi, T. and L. Reimer, 1974, Electron Microscopy, Canberra, Australia.

Ladd M.F.C. and Palmer, R.A., 1977, Structure Determination by X-ray Crystallography, Plenum Press, New York and London.

Laue, M. von, W. Friedrich and P. Knipping, 1912, Sitzungsberichte der

- mathematisch-physicalischen Klasse der K.B. Akademie der Wissenschaften Zu
Munchen, 303.
- Leapman, R.D., P. Rez, D. F. Mayers, 1978, Proc. 9th Intl. Cong. on E.M., (ed. J.M. Sturgess), p 526, Microscopical Society of Canada, Toronto.
- Leapman, R.D., P. Rez, D. F. Mayers, 1980, J. Chem. Phys., 72, 1232.
- Lenz, Z., 1954, Z. Naturf., 23 A, 185.
- Manson, S.T., 1972, Phys. Rev., A 6, 1013.
- Marton, L., 1968, In the Preface of Early History of the Electron Microscope, San Francisco Press, San Francisco, California.
- Marsh, R.E., 1958, Acta Cryst., 11, 654.
- Meshitsuka, G., K. Shindo, A. Minegishi, H. Suguro and Y. Shinozaki, 1964, Bull. Chem. Soc. Japan, V 37 No 7, 928.
- Oughton, B.M. and Harrison, P.M., 1957, Acta Cryst., 10, 479.
- Patterson, A.L., 1934, Phys. Rev., 46, 372.
- Patterson, A.L., 1935, Z. Krist., 90, 517.
- Pauling, L., 1969, The Nature of Chemical Bond Cornell University Press, Ithaca.
- Peterson, D.B., J. Holian and W.M. Garrison, 1969, J. Phys. Chem., V 73 No 5, 1568.
- Pines, D., 1963, Elementary Excitations in Solids, W.A. Benjamin Inc., New York and

Amsterdam.

Pullman, A. and B. Pullman, 1963, Quantum Biochemistry, InterScience, New York.

Raether, H., 1965, Springer Tracts in Modern Physics, 38, (ed: G. Hohler), 84,
Springer-Verlag, Berlin.

Riederer, H., 1981, Ph.D. Thesis, Universitat Regensburg, West Germany.

Schwinger, J., 1949, Phys. Rev., 75, 898.

Scott, W.T., 1965, Rev. Mod. Phys., 35, 231.

Siegel, G., 1972, Z. Naturforsch., 279, 325.

Stenn, K and G.F. Bahr, 1970, J. Ultra. Res., 31, 526.

Sternglanz, H., G.R. Freeman, C.E. Bugg, 1975, Acta Cryst. B 31, 1393.

Stout, G.H. and L.H. Jensen, X-ray Structure Determination A PRACTICAL GUIDE, Chapter
11, The Macmillan Company, New York.

Tivol, W.F., Bun-Woo B. Chang and D.F. Parsons, 1982, Ultramicroscopy, 9, 117.

Torii, K., and Y. Iitaka, 1970, Acta Cryst. B26, 1317.

Torii, K., and Y. Iitaka, 1973, Acta Cryst. B29, 2799.

Unwin, P.N.T. and Henderson, R., 1975, J. Mol. Biol., 94, 425.

Unwin, P.N.T., 1975, J. Mol. Biol., 98, 425.

Vainshtein, B.K. and Pinsker, Z.G., 1949, Zh. Fiz. Khim. 23, 1058.

Vainshtein, B.K., 1964, Structure Analysis by Electron Diffraction, Macmillan Company, New York.

Wallace, B.A. and R. Henderson, 1982, Biophys. J. Vol 39, 233.

Watanabe, H., 1964, Japan J. of Appl. Phys. 3, 804

Wentzel, G., 1927, Z.Phys. 40, 590.

Willis, B.T.M. and Pryor A.W., 1975, Thermal Vibrations in Crystallography, Cambridge University Press, London.

Wilson, A.J.C., 1942, Nature 150, 152.

Wittry, D.B., R.P. Ferrier, V.E. Cosslett, 1969, B.J. Appl. Phys (J. Phys D) 2, 1767.

Woolfson, M.M., 1970, An Introduction to X-ray Crystallography, Cambridge University Press, London.

Wooster, W.A., 1964, Acta Cryst. 17, 878.

Zeitler, E., 1982, Ultramicroscopy 10, 1.

Zimbrick, J.D., J.F. Ward, L.S. Myers, 1969, Intl. J. Rad. Biol. 16, 505.

APPENDIX 1: Removal of Mixed Scattering by Deconvolution.

A highly energetic electron beam, while traversing a specimen, may undergo multiple scattering with the atomic electrons. The probability that an electron would get scattered more than once depends upon the mean free path, λ_{in} for inelastic scattering. Since the value of λ_{in} is about 50 nm for 100 keV electrons, the probability of multiple scattering is considerably enhanced in the case of moderately thick electron microscope specimens.

Since the cross-section for valence electron scattering is larger compared to the cross-section for other various modes of inelastic scattering, a K-shell or L-shell excitation may be preceded or followed by valence electron excitation. Excitation of the valence electrons may correspond to single electron interband transitions or collective plasmon oscillations. In the absence of multiple scattering, the energy-loss spectrum beyond the excitation edge is called single scattering profile (SSP). The effect of multiple scattering of incident electron appears as a 'hump' in the SSP which makes quantitative assessments of elemental concentrations less accurate. Hence, it may be necessary to remove multiple scattering from the observed spectrum to yield SSP. One method of performing this is to employ the technique of deconvolution (Egerton and Whelan, 1974).

If the instrumental resolution function is given by $I_0(E)$ and if $I_L^0(E)$ is the observed intensity beyond the L-edge of an element, then one can write the following convolution integral to represent the observed intensity profile in the spectrum:

$$I_L^0(E) = \int_{-\infty}^{\infty} I_L^i(E) I_0(E-E') dE' = I_L^i(E) * I_0(E) \quad (1.1)$$

where $I_L^i(E)$ denotes the intensity at different energy losses which would be recorded by an ideal instrument. The probability of multiple scattering may be represented as a convolution of the SSP beyond the excitation edge, $I_L^s(E)$ with the ideal spectrum of the valence electron excitations i.e. $I_L^i(E)$, provided the two processes are independent (Egerton and Whelan, 1974). Since valence

electron scattering also forms a monotonically decreasing background at the excitation edge, the ideal scattering profile (in the absence of instrumental broadening) would be the sum of $I_1^i(E)$ and the convolution between $I_L^s(E)$ and $I_1^i(E)$.

Or,

$$I_L^i(E) = I_L^s(E) * I_1^i(E) + I_1^i(E) \quad (1.2)$$

Ideal spectrum due to valence electron excitation is, again, related to the observed spectrum by the instrumental resolution function as:

$$I_1^0(E) = I_1^i * I_0(E) \quad (1.3)$$

By combining equations 1.1 and 1.2 we get the observed spectrum beyond the L-edge:

$$\begin{aligned} I_L^0(E) &= [I_L^s(E) * I_1^i(E) + I_1^i(E)] * I_0(E) \\ &= I_L^s(E) * I_1^i(E) * I_0(E) + I_1^i(E) * I_0(E) \\ &= I_L^s(E) * I_1^0(E) + I_1^0(E) \end{aligned}$$

so,

$$I_L^s(E) * I_1^0(E) = I_L^0(E) - I_1^0(E) \quad (1.4)$$

If we denote the right hand side of this equation by $I_L^{0s}(E)$, which is equal to the remaining observed spectrum beyond the L-edge after the subtraction of the background, then we can write equation 1.4 as:

$$I_L^s(E) * I_1^0(E) = I_L^{0s}(E) \quad (1.5)$$

Equation 1.5 can be solved to yield the SSP by invoking convolution theorem which states that (Bracewell, 1978):

If the Fourier transforms of two functions $f(x)$ and $g(x)$ are represented by $F(s)$ and $G(s)$ respectively then the Fourier transform of $f(x) * g(x)$ will be $F(s)G(s)$. Or, the Fourier transform of a convolution of two functions is equal to the product of the Fourier transforms of individual functions.

Therefore, if the Fourier transforms of $I_L^s(E)$, $I_1^0(E)$ and $I_L^{0s}(E)$ are denoted by $I_L^s(\omega)$, $I_1^0(\omega)$ and $I_L^{0s}(\omega)$, then equation 1.5 can be written as:

$$I_L^s(\omega) \cdot I_1^0(\omega) = I_L^{0s}(\omega)$$

so,

$$I_L^s(\omega) = \frac{I_L^{0s}(\omega)}{I_1^0(\omega)} \quad (1.6)$$

Now, the SSP can be immediately obtained from equation 1.6 by taking inverse Fourier transform of both sides to yield:

$$I_L^s(E) = \mathbf{F}^{-1}[I_L^s(\omega)] = \mathbf{F}^{-1}\left[\frac{I_L^{0s}(\omega)}{I_1^0(\omega)}\right] \quad (1.7)$$

where \mathbf{F}^{-1} denotes the inverse Fourier transform. Breaking a convolution integral into a product in Fourier domain and a division of Fourier transforms to subsequently yield a function in the real domain is called deconvolution and obtaining the SSP from a multiple scattering profile by this technique is called deconvoluting the spectrum.

Reliable absolute quantitative estimates of elemental concentration from a thick specimen can only be performed by first subtracting the background from the observed spectrum and then by deconvoluting the spectrum with respect to the valence electron excitation. Quantitative estimates require information about the cross-section for inner shell ionization which can either be measured experimentally using a thin specimen or may be calculated on the basis of an atomic model (Manson, 1972 and Leapman et al., 1978). Accuracy of these theoretical calculations of cross-sections and the effect of deconvoluting the spectrum can be seen by comparing the theoretically calculated values of cross-section for the L-shells of Aluminum and Silicon with their experimentally determined values.

Experiments were performed at 80 keV on vacuum evaporated films of aluminum and silicon oxide, mounted on copper grids, in a JEM 100B electron microscope equipped with an energy-loss spectrometer (Egerton, 1978). The energy-loss spectrum was recorded in a TI 990 microcomputer programmed to act as a multichannel analyser (Egerton and Kenway, 1979). An objective aperture

was used to determine the maximum angle of scattering, α , allowed into the spectrometer, α was 4.2 mrad in this case.

Figure 1.1(a) shows the energy-loss spectrum of aluminum in the region of L-shell excitation, which corresponds to $I_L^0(E)$ while figure 1.1(b) shows the same spectrum after the subtraction of the background due to valence electron excitation ($I_L^0(E)$) computationally and the resulting spectrum corresponds to $I_L^{0s}(E)$ of equation 1.5.

Fourier transforms were calculated using a Fast Fourier transform program based on Cooley-Tukey algorithm (Cooley and Tukey, 1965), for energy losses lying in the low region of the spectrum i.e. for losses between 0 and 50 eV, and for $I_L^{0s}(E)$ which corresponded to losses beyond the L-edge, up to 100 eV. Fourier transforms were divided using a computer program and an inverse Fourier transform was calculated to yield the SSP of the energy-loss spectrum, $I_L^{0s}(E)$. In Figure 1.2 are shown the original (with background removed) and deconvoluted spectra beyond the L-edge of silicon. The resulting intensity per channel is proportional to the energy-differential cross-section, $d\sigma_L/dE$, for ionization of L-shell by electron scattered through an angle $< \alpha$.

Absolute values of cross-section for silicon were obtained by matching the deconvoluted data at 100 eV beyond the L-edge, with the experimental values of partial cross-section obtained by Joy (Joy et al., 1979) after adjusting the latter to an incident energy of 80 keV and $\alpha = 4.2$ mrad. These absolute values of partial cross-section, $\sigma_L(\alpha, \Delta)$, are plotted in figure 1.3 as a function of energy window Δ .

For aluminum absolute values of partial cross-section were not calculated due to lack of experimental absolute values of partial cross-section, $\sigma_L(\alpha, \Delta)$. However, the energy dependence of partial cross section can be written in a normalised form using equation 2.6 as :

$$x(\Delta) = \frac{\sigma_L(\alpha, \Delta)}{\sigma_L(\alpha, \Delta_1)} = \frac{I_L^s(\alpha, \Delta)}{I_L^s(\alpha, \Delta_1)} \quad (1.8)$$

where, $I_L^s(\alpha, \Delta)$ denotes the area under the deconvoluted spectrum, beyond the ionization edge upto the energy window Δ for the electrons scattered through

an angle less than α . Δ_1 was taken to be equal to 100 eV. The experimental $x(\Delta)$ curve for aluminum L-shell excitation is shown in Figure 1.4.

From equation 2.5 one can obtain the following equation for $x(\Delta)$:

$$x(\Delta) = \frac{\sigma_L(\alpha, \Delta)}{\sigma_L(\alpha, \Delta_1)} = \frac{I_L(\alpha, \Delta)}{I_L(\alpha, \Delta_1)} \cdot \frac{I_1(\alpha, \Delta_1)}{I_1(\alpha, \Delta_1)} \quad (1.9)$$

Here, $I_L(\alpha, \Delta)$ denotes the area under the original spectrum (with background removed) beyond the L-edge and upto an energy window Δ for the electrons scattered through an angle less than α . While $I_1(\alpha, \Delta)$ represents the area under the low-loss region upto the same energy window. Δ_1 was again taken to be equal to 100 eV. Experimental values of $x(\Delta)$ calculated using equation 1.9 are shown in Figure 1.4 as a dashed curve. For comparison, also included in this figure are the $x(\Delta)$ values obtained from the original data, by taking the ratio of $I_L(\alpha, \Delta)$ and $I_L(\alpha, \Delta_1)$ which are shown as a dotted curve.

The experimental values of $x(\Delta)$ plotted in figures 1.3 and 1.4 were compared with the theoretical values obtained using energy-differential cross-section calculated by Manson (Manson, 1972) for L-edge of aluminum and silicon. Partial cross-sections were obtained by integrating differential cross-sections. Absolute values of partial cross-section are plotted in Figure 1.3, for silicon (as discrete points) while $x(\Delta)$ values for partial cross-section for aluminum are plotted in Figure 1.4 as discrete points.

The trend of $x(\Delta)$ values obtained from the SSP of the energy-loss spectrum seems to be in excellent agreement with the theoretically calculated values of Manson, while the curve corresponding to the $x(\Delta)$ values obtained from the original data shows a significant departure from the theoretical values. Moreover, the curve corresponding to equation 2.7 also significantly differs from the theoretical values and represents poorer accuracy, especially for low Δ values, than that obtained by using a similar procedure applied to K-shell ionization spectra (Egerton, 1978). It is understandable from the fact that equation 1.9 is exact only if the intensity is sharply peaked at the ionization energy as for K-shells, whereas the profile for the L-edge rises rather gradually. The slight degree of disagreement occurs between the theoretically

computed values of $\sigma_{L,\alpha,\Delta}$ and $x(\Delta)$ for silicon and aluminum in Figures 1.3 and 1.4. The spectral intensity due to the excitation of an L-shell electron would depend upon the density of states between the 2p level and the conduction band. Since such considerations are not included in the theoretical calculations, which are based on an atomic model, a small difference might be expected to occur between the theoretically computed and experimentally measured values of partial cross-sections.

Hence, in the case of thick specimens it is desirable to deconvolute the spectrum to obtain the single scattering profile otherwise incorrect values of elemental concentration might result. Especially, in case of radiation damage measurements of biological specimens, when the mass loss occurs, this could lead to inaccurate values of elemental concentration. However, for thin biological specimens, when the thickness is around 15-20 nm, it is not necessary to deconvolute the spectrum due to very small probability of multiple scattering.

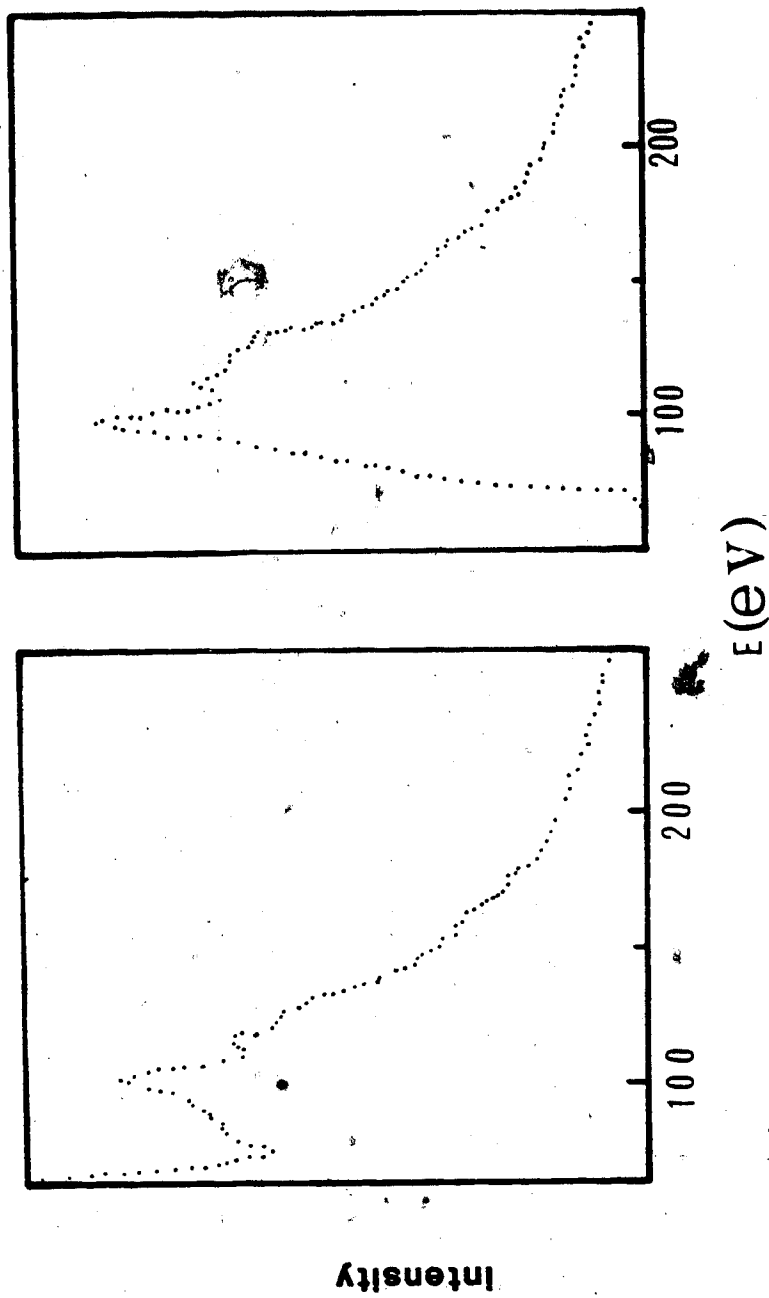


Figure 1.1 (a) Electron energy-loss spectrum of Aluminum (region of L-shell excitation) (b) same spectrum after the subtraction of background.

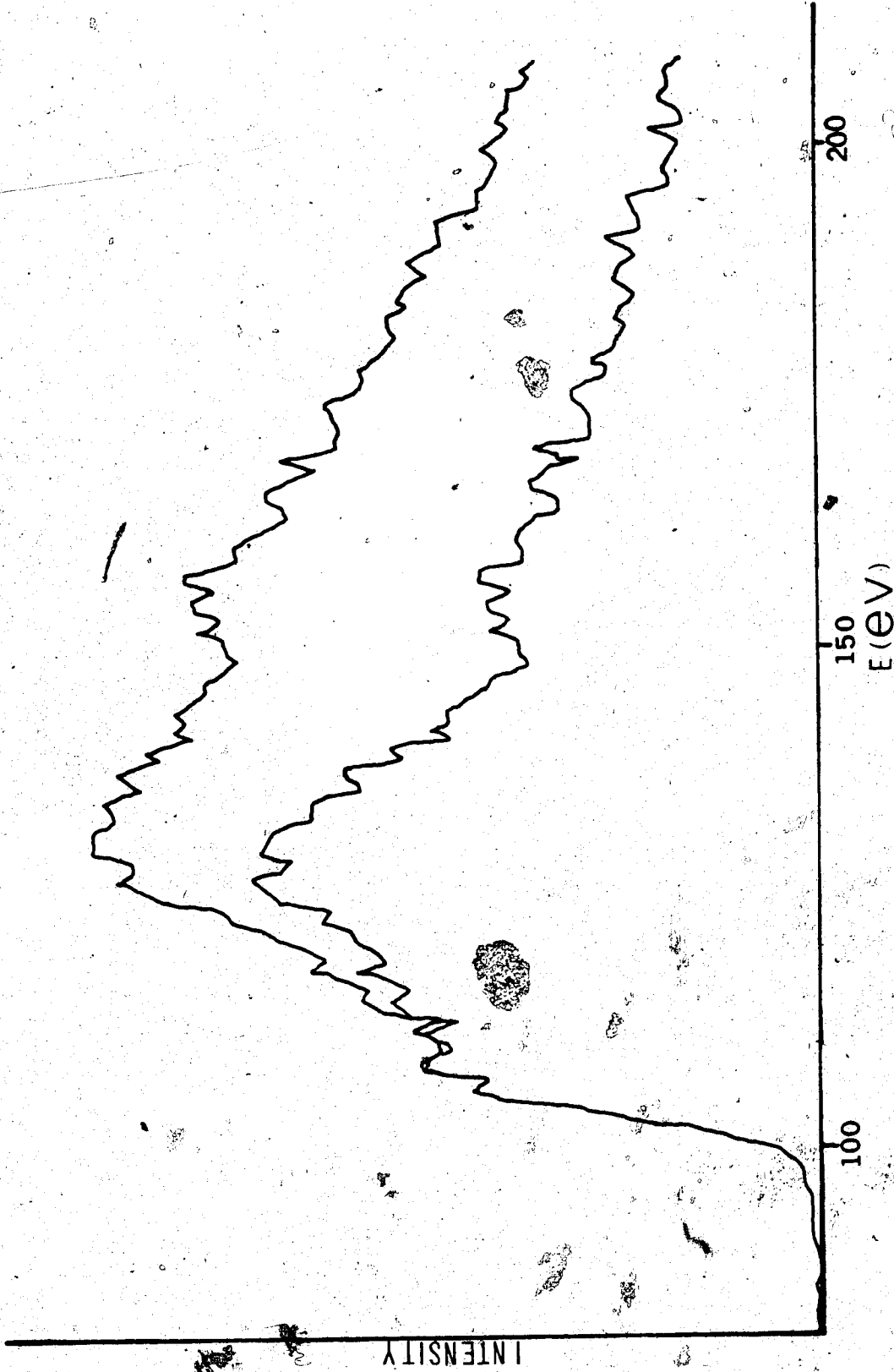


Figure 1.2 Original spectrum (with background removed) after the L-edge of Silicon (upper curve) and deconvoluted spectrum (lower curve)

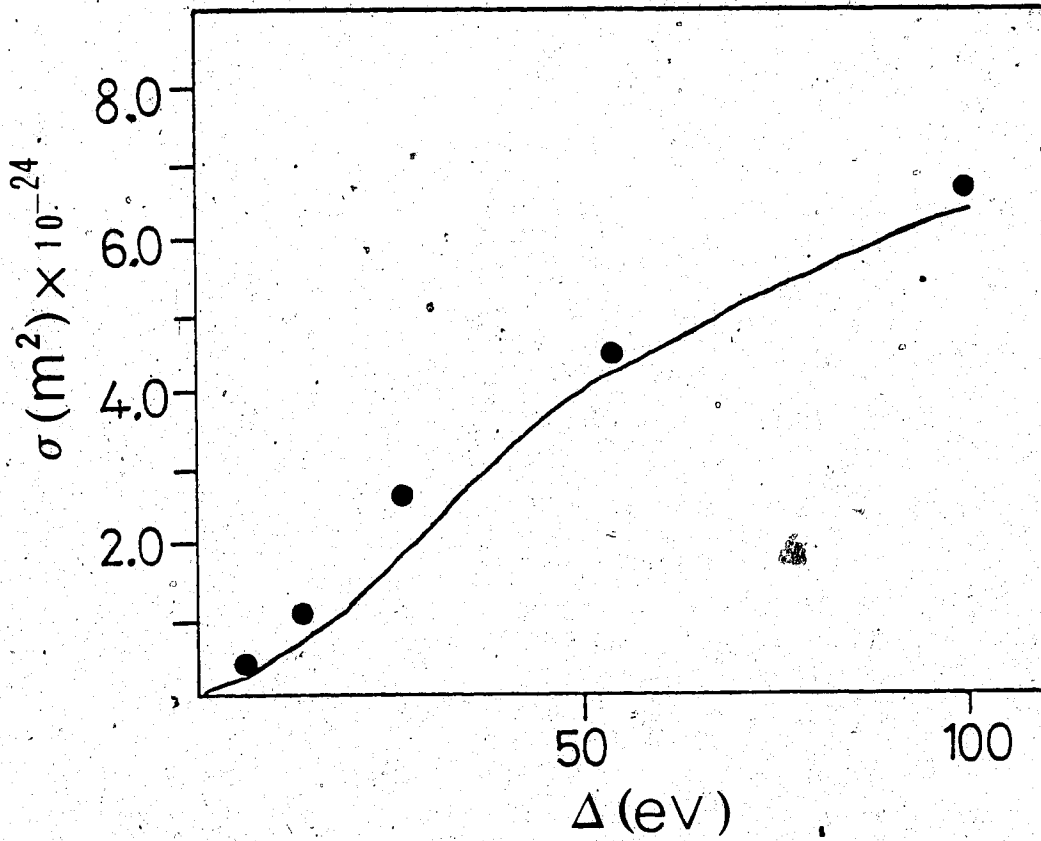


Figure 1.3 Absolute partial cross-section for L-shell excitation in Silicon plotted as a function of energy window.

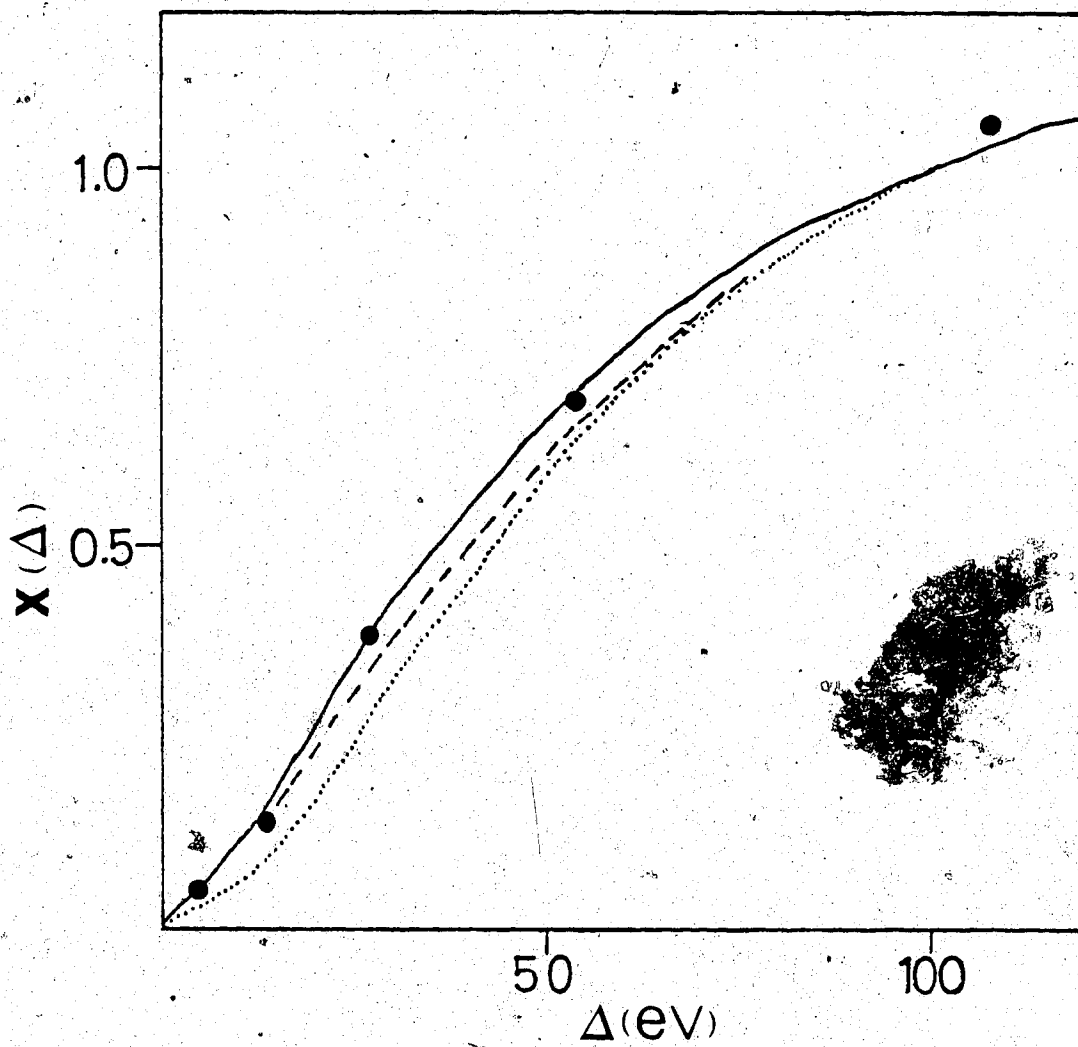


Figure 14 Normalised partial cross-section $X(\Delta)$ for L-shell excitation in Aluminum plotted as a function of energy window.